Fakultät für Mathematik, Informatik und Naturwissenschaften | RWTH AACHEN UNIVERSITY

The Role of Nanostructure on Carrier Transport in Thermoelectric Materials Addressed by Focused Ion Beam Assisted Device Fabrication

Von der Fakultät für Mathematik, Informatik und Naturwissenschaften der RWTH Aachen University zur Erlangung des akademischen Grades einer Doktorin der Naturwissenschaften genehmigte Dissertation

vorgelegt von

Riga Wu, M.Sc.

aus

Hohhot, China

Berichter*:* Prof. Dr. Matthias Wuttig
Prof. Dr. Rainer Waser

Tag der mündlichen Prüfung*:* *12th Marc 2025*

Dedicated to my father, Damulin.

For that childhood afternoon when we used a glass bottle as a lens, and the light spot we observed together sparked my curiosity for science.

ABSTRACT

Nanostructures, including grain boundaries (GBs), ion segregation, and precipitates, have a profound impact on carrier transport and material properties. The study of these nanostructures and their influence is an important and burgeoning topic. Nevertheless, the majority of studies on GB-related properties primarily emphasize the average grain size, neglecting the significant role played by the complex structure and composition of GBs in determining transport properties. In addition, doping is a crucial method use to tailor material properties, resulting in ion segregation at boundaries and precipitates.

These kinds of nanostructures significantly impact carrier concentration, mobility, and conductivity, ultimately determining the thermoelectric (TE) performance. However, the mechanisms underlying ion segregation and precipitates remain unclear due to the limitations in the current macroscopic experiments. Consequently, characterizing the structure and composition of individual nanostructures becomes a prerequisite for comprehending and engineering these materials.

To achieve this goal, this thesis focuses on studying the effect of individual nanostructures on the electrical properties of TE materials using a novel technique based on focus ion beam(FIB)-assisted device fabrication. This novel technique is a flexible and comprehensive approach, combining FIB, electron backscatter diffraction (EBSD), energy-dispersive X-ray spectroscopy (EDX), atom probe tomography (APT), and a physical property measurement system (PPMS), in order to investigate the impact of nanostructures, including GBs, twin boundaries, and precipitates, on charge carrier scattering. This correlative study enables the determination of the local microstructure, composition, and transport properties of individual nanostructures.

In Chapter IV, the thesis focuses on studying the impact of GBs in Ag-doped PbTe. This investigation reveals the electronic characteristic and chemical composition of individual GBs, underscoring how compositional heterogeneity influences electrical conductivity. Notably, it is found out that Ag segregation at the GBs enhances electrical conductivity, while the second phase, formed by Ag replacing Pb atoms, acts as a scattering center.

Chapter V explores the influence of the misorientation angles of individual GBs on charge carrier scattering in slightly Ag-dope PbTe. The study demonstrates that charge carriers experience significantly stronger scattering at high-angle GBs (HAGBs) than at low-angle GBs (LAGBs). The APT measurements indicate a higher fraction of trapping states at HAGBs, along with a complete breakdown of the metavalent bond, which contributes to the increased scattering of charge carriers.

Chapter VI investigates the impact of twin boundaries on the electrical transport properties in $Bi_2Te_{2.7}Se_{0.3}$. The study discovers that the presence of two parallel twin boundaries enhances mobility and

conductivity. This enhancement is attributed to the coherent interface and uniform composition distribution at twin boundaries. This finding indicates that the twin boundaries do not scatter carriers in this material, providing insights for designing high-performance TE materials.

In the last chapter, this thesis examines telurrium(Te)-based materials doped with antimony (Sb), bismuth (Bi), and arsenic (As). The Energy-Dispersive X-ray Spectroscopy(EDX) and APT measurements provide clear evidence for the poor solubility of dopants in the host material, leading to the formation of telluride precipitates. The local transport measurements of pre-characterized precipitates show that the dramatically increased electrical conductivity is due to the incorporation of precipitates, providing guidance for enhancing the performance of single-element thermoelectrics. The APT characterization reveals the metavalent bonding nature of the precipitates, further aiding in material design.

The novel FIB-assisted device fabrication technique presented in this thesis provides a new approach to study specific nanostructures in bulk materials, breaking previous experimental limitations. The findings on charge transport across the GBs and precipitate have implications for various applications, including TEs, memory materials, and mid-infrared devices. The versatility of this technique allows for its adaptation to study other solid materials, and explores extraordinary physical properties in newly synthesized materials. Future directions involve using this technique for solar cell grain boundary research and various electrical measurements. This method enables detailed analysis of how individual defects affect charge carrier transport in semiconductors and expands nanostructure research in material science.

CONTENTS

1 INTRODUCTION

The semiconductor industry and information technology have witnessed a rapid growth in recent years, with smartphones and other portable devices fundamentally changing the way we live. Artificial intelligence (AI) technology has significantly accelerated the discovery of information and built a new data-driven economy and society. This has led to an increased demand for semiconductor devices, with AI technology firms using graphics processing units (GPUs) and tensor processing units (TPUs) to increase computational speed and to reduce power consumption. The information technology industry requires higher data storage capacities, and personal digital devices requiring steady performance at a competitive price. Moreover, as environmental concerns become more prominent, low energy costs and eco-friendly qualities are increasingly desirable, further driving the demand for functionally enhanced materials that can satisfy the diverse market demands.

In semiconductor engineering, doping is the most common way to tune the carrier concentration. Along with doping, segregated ions at grain boundaries (GBs), secondary phases, and precipitates are generated in the semiconductor, which scatter carriers and phonons simultaneously. This also has an essential impact on the properties of the semiconductor. Figure 1 shows that charge carriers scatter with point defects, GBs and other types of nanostructures containing precipitates and dislocations in thermoelectric(TE) materials. Firstly, the bulk sample contains increased microscale GBs that improve the scattering of high-energy carriers. Secondly, the nanostructures produced through dynamic recrystallization contribute to the scattering of phonons with middle wavelengths. Lastly, dislocations and lattice distortions, combined with intrinsic and extrinsic point defects, scatter low-energy charge carriers. As a result, this multiscale microstructure effectively decreases the electrical mobility and conductivity across various types of nanostructures. [1]

TE materials are also the target materials in this thesis. For this class of functional materials, both doping and nanostructure effects on carrier transport determine their performance. The efficiency of its electricity conversion is measured by the figure of merit ZT to quantify the device's performance. The aim of designing an excellent TE material is to achieve a high ZT value, which is the figure of metric to evaluate the heat-to-electricity conversion efficiency. However, factors determining this value are coupled and demand to balance their relation: carrier concentration and effective mass, Seebeck coefficient and electrical conductivity, electrical conductivity and thermal conductivity. The band structure engineering via doping and various synthesis methods, such as GB engineering, has seen a large increase in the ZT value. The logic behind the ZT improvement method induces dif-

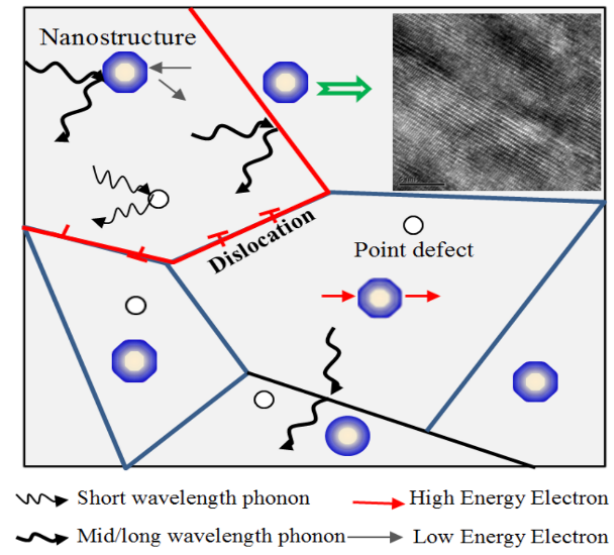

Figure 1: Charge carrier and phonon scattering in a bulk material with various types of nanostructures. [2]

ferent types of defects or nanostructures to decrease the charge carrier scattering and enhance the phonon scatting. Nonetheless, due to the limitation of current equipment, the underlying carrier scattering mechanism of different nanostructures has not been fully understood.

The novel technique proposed in this thesis can help to study the effect of nanostructures on carrier transport. The advantages and novelty of this correlative study are manifold. First, it is flexible enough to extract the impact of any target nanostructure. For example, a pre-characterized GB is selected from millions of randomly distributed GBs in bulk with the help of a Focus ion beam(FIB). Yet, the majority of studies of GB-related properties focus on the average grain size. [3, 4] Second, the pre-characterization of crystallography, composition, and specific microstructure can be done with the help of the FIB dual beam system. For precipitate studies, before conducting an electrical measurement on Sb-doped tellurium with single Sb_2Te_3 precipitate, energy-dispersive X-ray spectroscopy(EDX) can characterize it to help in selecting a target sample, which is impossible to accomplish by other experimental methods. Furthermore, the entire process, from choosing a target GB to characterization and, finally, sample fabrication, can be carried out inside the FIB system. It largely enhances the experimental efficiency and lowers the cost. Third, this novel method is applicable over a broad temperature range, which is important for various applications, including power generation (as TE), memory (as phase change material), mid-infrared lasers and detectors. The approach devised here can be adapted to many other solids, providing a new avenue for the design of functional materials via GB engineering. Unlike GB research in metals or other solids, transport measurements are not restricted to a narrow temperature range based on GB resistivity alone. [5, 6, 7] Fourth, the GB topology and compositions can be revealed by atomic probe tomography (APT), which has no 2D projection effect and much higher chemical

sensitivity than the electron-beam-based techniques such as transmission electron microscopy(TEM)[8, 9] and associated energy dispersive spectroscopy (EDS). Lastly, the unique attribute of APT in capturing the bond-breaking behaviour can provide information on the chemical bonding mechanism at and aside from the GB. [10] This will greatly enrich our understanding of the origin of GB charge carrier scattering by taking the structure, composition, and bonding into account.

In summary, the goal of this thesis is to understand the effect of nanostructures on materials' electrical properties using an FIB-assisted device fabrication technique to guide functional material design.

2

FUNDAMENTALS

2.1 FUNDAMENTALS OF THERMOELECTRIC MATERIAL

2.1.1 *The basics of thermoelectric material*

Due to the swift growth of the economy and industry, the utilization of fossil fuel as a primary energy source has faced both resource limitations and environmental pollution. To address these issues, the development of renewable energy sources and the improvement of energy efficiency have become the primary focus of energy research. TEs is a promising technology that can convert waste heat into electricity directly. A TE device can convert heat to electricity under a temperature gradient (Seebeck effect) or drive heat from one side to another with electric current (Peltier effect). The Seebeck coefficient, S or α, measures the voltage generated by a temperature difference, as shown in the formula $V = S\Delta T$. The Peltier coefficient, Π, quantifies the heat current driven by an electric current ($\Pi = S\dot{T}$). TE materials are often heavily doped semiconductors that either have free electrons or holes that carry both charge and heat. The efficiency of its electricity conversion is measured by the figure of merit ZT to quantify the device's performance. It is a dimensionless value when evaluating TE energy conversion efficiency. The formula defines the ZT value:

$$ZT = \frac{S^2\sigma}{k}T \tag{1}$$

where S is the Seebeck coefficient, σ is the electrical conductivity, k is the thermal conductivity, and T is the absolute temperature. An ideal TE material should have a high Seebeck coefficient, high electrical conductivity, and low thermal conductivity, described as "electron crystal - phonon glass". [11] This is because the combination of a high Seebeck coefficient and electrical conductivity is typically found in crystalline metals or semiconductors. In contrast, low thermal conductivity is often found in amorphous materials or glasses with low phonon or lattice thermal conductivity. The critical determinant for improving the performance of TE technology is the interrelated relationship between various TE parameters. Since these transport properties are contingent upon interdependent material characteristics, multiple parameters must be fine-tuned to achieve a maximum ZT. To illustrate this point, a high effective mass increases the Seebeck coefficient but decreases the electrical conductivity, while a high carrier concentration enhances the electrical conductivity but lowers the Seebeck coefficient. Therefore, careful consideration of the trade-offs between coupled parameters is necessary for optimizing TE performance.

The typical ZT values of thermoelectric materials are below 1.0, which limits the performance of these devices. [12] According to cur-

rent studies, bismuth telluride and its alloys are common for room-temperature applications with ZT values around $1.0 - 1.5$. [13] Lead telluride and its alloys, effective in medium temperatures, reach ZT values up to 2.0. [14] Skutterudites and Half-Heusler alloys are used in medium to high-temperature ranges, achieving ZT values of about $1.0 - 1.5$. [15, 16] Emerging materials like tin selenide (SnSe) have shown ZT values above 2.5 under specific conditions. [17] In this thesis, lead telluride, bismuth telluride and doped tellurium are the main focus.

Several methods have been proposed to optimize TE energy conversion. One approach is to optimize doping to maximize the ZT value. [18] Another strategy is to increase phonon scattering by introducing point defects and nanostructures.[19, 20, 21] Additionally, band engineering, such as multi-valley transport, has been employed to avoid the trade-off between Seebeck coefficient and electrical conductivity in order to enhance the power factors. [22, 23]

2.1.1.1 *Contradictory relation between Seebeck coefficient and electrical conductivity*

One of the most well-established and easily understood conflicts in TE materials is the coupled relation between the carrier concentration n and two key parameters in transport properties: electrical conductivity σ and the Seebeck coefficient S.

The relation between n, S, and σ can be observed in the Single Parabolic Band (SPB) model. [19, 24, 25] In the case of degenerate semiconductors with a simple and parabolic band ($m^*_{DOS} = m^*_{Drude}$), the Seebeck coefficient S is expressed as follows:

$$S = \frac{8\pi^2 k_B^2}{3eh^2} m^*_{DOS} \left(\frac{\pi}{3n}\right)^{\frac{2}{3}} \tag{2}$$

in which k_B is the Boltzmann constant, h is the Planck constant, e is the electron charge, and m^*_{DOS} is the density of states effective mass. The Drude model allows for the estimation of the electrical conductivity σ as:

$$\sigma = ne\mu = \frac{ne^2\tau}{m^*_{Drude}} \tag{3}$$

where μ is the carrier mobility, τ is the carrier relaxation time, e is the elementary charge, and m^*_{Drude} is the conductivity effective mass. [26] According to Equation 2, the Seebeck coefficient is inversely proportional to the carrier concentration, whereas the electrical conductivity is directly proportional to the carrier concentration, as shown in Equation 3. As illustrated in Figure 2, the conflict between S and σ requires finding an optimal value in charge carrier concentration in order to maximize the ZT value. This peak of ZT value occurs at optimal carrier concentrations between 10^{19} and $10^{21} cm^{-3}$. This explains why most good TE materials are extremely heavily doped semiconductors that must have a large concentration of defects from

extrinsic dopants. Nonetheless, this coupled relation allows for calculating any factor through its function of carrier concentration with reasonable accuracy. [27]

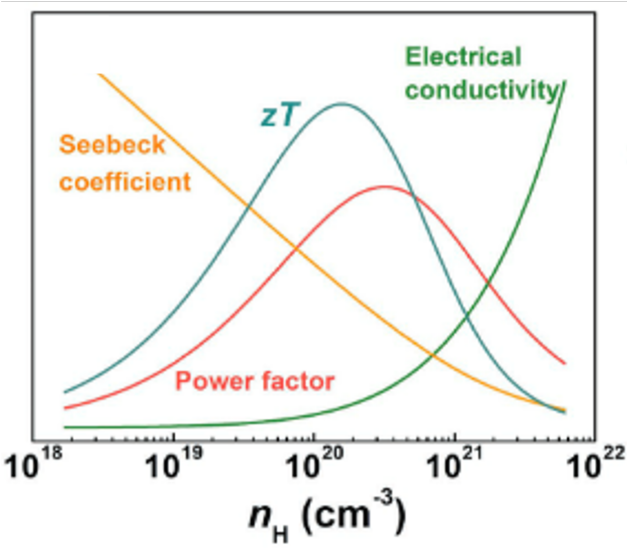

Figure 2: The optimal concentration of charge carriers for ZT and power factor. [28]

2.1.1.2 *Contradictory relation between electrical conductivity and thermal conductivity*

To design a high-performance TE material, another conflict between electrical conductivity σ and thermal conductivity k is required to be considered. This relation can be given from the Wiedemann-Franz law [26]:

$$\kappa = \kappa_e + \kappa_L \tag{4}$$

and

$$\kappa_e = L\sigma T \tag{5}$$

where κ is the total thermal conductivity, κ_e is the electronic thermal conductivity, κ_L is the lattice thermal conductivity, σ is the electrical conductivity, and L is the Lorenz number. Thus, the ZT formula of TE materials can be derived as:

$$ZT = \frac{S^2\sigma}{k}T = \frac{S^2\sigma}{\kappa_e + \kappa_L}T = \frac{S^2}{L + \frac{\kappa_L}{\sigma}T} \tag{6}$$

Equation 6 shows that if the carrier concentration is optimized, both the Seebeck coefficient and the Lorenz number remain relatively constant within a specific range. Thus, the only factor influencing this becomes the ratio $\frac{\kappa_L}{\sigma}$ in the denominator. To maximize ZT, one would expect the ratio $\frac{\kappa_L}{\sigma}$ to be as low as possible, implying that κ_L should be minimized, while σ should be maximized. A higher thermal conductivity often accompanies a higher electrical conductivity. Since

phonons and electrons share the same sublattice, the scattering occurs on both electrons and phonons. Therefore, from the perspective of the charge carrier and phonon scattering mechanism, optimizing ZT requires a compromise between electrical and thermal conductivity.

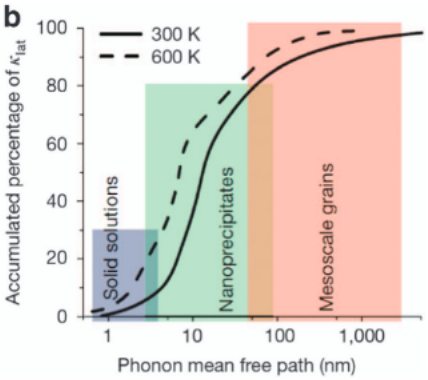

Figure 3: Variation of the accumulated percentage of K_L with the phonon mean free path. [29]

Owing to the difference in the mean free path between phonons and charge carriers, defect engineering, especially nanostructures, provides a solution to decouple the interrelated k and σ. For electrons, their mean free path is in the order of a few nanometers, e.g. 5 nm for degenerate semiconductors. [30] With regard to the effective length of phonons, the mean free path varies from a few nanometers to thousands of nanometers. As shown in Figure 3, the accumulated thermal conductivity increases with the phonon mean free path. Introducing different types of nanostructures at various scales selectively scatters phonons, reducing thermal conductivity. [29, 31] These scattering centers are expected to have strongly scattered phonons but weakly scattered electrons. This requires a deep understanding of the scattering mechanism of defects in TE materials on phonons and electrons. Considering the difference in the scattering mechanism for electrons and phonons, a suitable defect introduction can be used to further optimize the ZT value.

2.1.2 *Thermoelectric materials studies in this thesis*

PbTe, a TE material widely applied in industry, has an exceptional TE performance. [28, 34, 19] The crystal lattice of PbTe is NaCl type, where Pb atoms occupy cation sites, and Te atoms occupy anion sites (Figure 4 (A)). [35] In this thesis, Ag is chosen as the dopant due to its widespread use in TEs, and its ability to decorate GBs, which is beneficial for visualizing different GB features in the APT. In Chapter III, the Ag doping concentration is higher. The diverse electrical transport results show a close relationship with the corresponding microstructure at the GB. In Chapter IV, the Ag content is kept low (PbTe-0.005Ag) so as to avoid the formation of complex structural defects and second-phase precipitates at the GBs. [36] The electrical

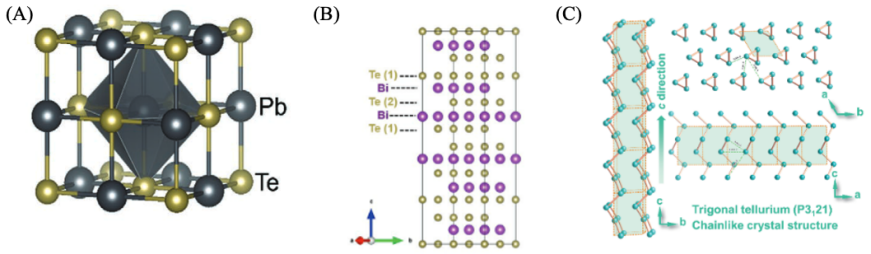

Figure 4: (A) Crystal structures of PbTe lattice structure (B) layer structure of Bi_2Te_3, including the quintuple layer of $Te(1) - Bi - Te(2) - Bi - Te(1)$ [32] (C) trigonal tellurium from the top and side view. [33]

conductivity type (n-type or p-type) of Ag-doped PbTe depends on the concentration of Ag. [37, 36, 38] The incorporation of Ag atoms within the PbTe matrix can lead to either n-type or p-type doping characteristics. When Ag atoms are located at interstitial sites, they act as donors by providing additional electrons, resulting in n-type conductivity. Conversely, if Ag atoms take the place of Pb atoms at substitutional sites, the Ag^{1+} ions replace the Pb^{2+} ions, creating a hole, thus leading to p-type conductivity. Previous studies have observed that Ag doping in PbTe can exhibit dynamic doping behaviour, which is attributed to the limited solubility of Ag in the PbTe matrix. [39]

Bi_2Te_3-based alloys have been shown to perform best for the near-room temperature range. The n-type Bi_2Te_3-based material exhibits a ZT value of around 1.2, which is lower than that of the p-type Bi_2Te_3 ($ZT = 1.4 \sim 1.8$). Various methods, including heterostructures [18], microstructures [40] and grain boundary engineering have been applied to improve the performance of the n-type Bi_2Te_3-based alloys. Recently, Bi_2Te_3 has been classified as a metavalently bonded compound due to its unique property portfolio, which enables its superior TE performance. [41, 42] Figure 4 (B) shows their quintuple layer (QLs) atomic structure, which contains five sublayers of Te(1)-Bi-Te(2)-Bi-Te(1) and belongs to the 3Rm space group. [32]

Elemental tellurium (Te), which is a narrow bandgap semiconductor with a complex Fermi surface, has been regarded as a promising TE material at medium temperatures. As shown in Figure 4 (C), its trigonal structure has strong intra-chain covalent bonding and weak inter-chain Van Der Waals bonding. Its lattice constants are $a = b = 4.456$Å and $c = 5.921$Å. Te's quasi-1D crystal lattice along the c-direction makes it anisotropic, and this could affect heat transport. [33]

2.1.3 *Carrier scattering mechanism in thermoelectric materials*

The properties of materials concerning their electronic behaviour are typically explained using the semi-classical transport theory. This theory takes into account important factors like the density of the charge

carriers (n), their mobility (μ), and their effective mass (m^*). This thesis employs the Boltzmann Transport method as a comprehensive approach to investigate the transport properties and scattering mechanisms in TE materials, especially highly doped semiconductors. The starting point of these theories is to take an external field as a perturbation for a many-particle system in equilibrium. We can think of the electron as a semi-particle. Assuming the system is inhomogeneous on a macroscopic scale, and the scattering is weak, we may describe the motion of electrons by a semi-classical distribution function $f(k, r, t)$ which depends not only on the wavevector k, but also on the position r and time t in phase space. If there is no scattering, this state will move through the phase space satisfying the transport equation $\frac{\partial f}{\partial t} = 0$. If a voltage bias or a temperature gradient is applied and causes a perturbation, the $f(\vec{k}, \vec{r}, t)$ is out of equilibrium state $f_0(\vec{k}, \vec{r}, t)$. Thus, the transport equation is $\frac{\partial f}{\partial t} = \frac{\partial f}{\partial t}\big|_{\text{coll}}$. The result is:

$$\frac{\partial f}{\partial t} + \nabla_k f \cdot \frac{d\mathbf{k}}{dt} + \nabla f \cdot \frac{d\mathbf{r}}{dt} = \left.\frac{\partial f}{\partial t}\right|_{\text{coll}} \tag{7}$$

Inserting the general force $\frac{d\vec{p}}{dt} = \frac{d(\hbar\vec{k})}{dt} = \vec{F}$ into the equation 7, it is transformed into:

$$\frac{\partial f}{\partial t} + \frac{1}{\hbar}\mathbf{F} \cdot \nabla_k f + \boldsymbol{v} \cdot \nabla f = \left.\frac{\partial f}{\partial t}\right|_{\text{coll}} \tag{8}$$

A relaxation time approximation is

$$\left.\frac{\partial f}{\partial t}\right|_{\text{coll}} = -\frac{f - f_0}{\tau} \tag{9}$$

used in the left collision term, the equation 8 becomes:

$$\frac{\partial f}{\partial t} + \frac{1}{\hbar}\mathbf{F} \cdot \nabla_k f + \boldsymbol{v} \cdot \nabla f = -\frac{f - f_0}{\tau} \tag{10}$$

In a uniform, static electric field given by $\mathbf{F} = -e\mathbf{E}$, the distribution function has not changed a lot. Thus, the distribution function is rewritten as $f = f_0 + f_1$, where f_1 is the deviation from the equilibrium distribution function f_0. The equation is changed into:

$$\frac{\partial f_1}{\partial t} + \frac{1}{\hbar}\mathbf{F} \cdot \nabla_k f_0 + \boldsymbol{v} \cdot \nabla f_0 = -\frac{f_1}{\tau} \tag{11}$$

Since $\partial f_1/\partial t = 0$, the left side of equation 11 can written as:

$$\frac{1}{\hbar}\nabla_k f_0 = \frac{1}{\hbar}\frac{\partial f_0}{\partial E}\nabla_k E = v\frac{\partial f_0}{\partial E} \tag{12}$$

$$\nabla f_0 = \frac{\partial f_0}{\partial E_0}\nabla E_F \tag{13}$$

Then the first-order term is:

$$f_1 = e\tau\frac{\partial f_0}{\partial E}\boldsymbol{v} \cdot \mathbf{E} \tag{14}$$

where $\mathbf{E}' = \mathbf{E} - (1/e)\nabla E_F$ is the electric field force. The current is derived as:

$$j = -\frac{2e}{(2\pi)^3}\int \boldsymbol{v} f_1 \, d\mathbf{k} = \sigma \mathbf{E}' \tag{15}$$

The electrical conductivity can be gotten as:

$$\sigma = -\frac{2e^2\tau}{(2\pi)^3}\int \boldsymbol{v}v\frac{\partial f_0}{\partial E}d\mathbf{k} \tag{16}$$

Assuming the electric field E lies in the z-direction, we replace v by v_z, and take the average of the mean squared velocity across the three directions to obtain $\langle v_z^2 \rangle = v^2/3$ and a parabolic band with $E = \hbar^2 k^2/2m^*$, and then $v\,(-\partial f_0/\partial E) = -(1/\hbar)\partial f_0/\partial k$, the formula can be simplified as:

$$\begin{aligned}
\sigma &= -\frac{2e^2\tau}{3(2\pi)^3}\int dk v^2 \frac{\partial f_0}{\partial E} \\
&= -\frac{2e^2\tau}{3(2\pi)^3 m^*}\int_0^\infty dk 4\pi k^3 \frac{\partial f_0}{\partial k} \\
&= -\frac{2e^2\tau}{3(2\pi)^3 m^*}\left(-4\pi k^3 f_0|_0^\infty + 3\int_0^\infty dk 4\pi k^2 f_0\right)
\end{aligned}$$

The initial term becomes zero at the lower limit when $k = 0$ and at the upper limit when $f_0 = 0$. The conductivity becomes:

$$\sigma = \frac{ne^2\tau}{m^*} \tag{17}$$

in which the number density of electrons $n = \left[\frac{2}{(2\pi)^3}\right]\int f_0 dk$, and τ is the relation time. In the Drude model, the electrical conductivity is described by the formula $1/\rho = \sigma = ne\mu$, and the mobility can derived as:

$$\mu = \frac{e\tau}{m^*} \tag{18}$$

Here, τ is the scattering time, and m_I^* is the inertial or conductivity effective mass that in complex materials, is different from but related to the density-of-states mass or Seebeck mass m_{DOS}^*. The mobility and charge carrier concentration are often estimated using Hall effect measurements. Since most TEs are heavily doped semiconductors, the dominant charge polarity can be determined by the slope of the Hall voltage when applying a magnetic field scan. If both electrons and holes are present in a material, their Hall effects compensate for each other and decrease the Hall coefficient. This Hall coefficient is defined as $R_H = \frac{t}{IB}\left(V_{H,h} + V_{H,e}\right)$, in which $V_{H,h}$ and $V_{H,e}$ represent the Hall voltage of hole and electron, t, I and B refer to the thickness, current and magnetic field respectively. Unlike the Hall mobility, the weighted mobility is measured by the Seebeck coefficient and resistivity, as illustrated in Figure 5. [43] In this thesis, the current applied is quite low, so it does not cause a temperature gradient in the measured sample. So here, we only use Hall mobility.

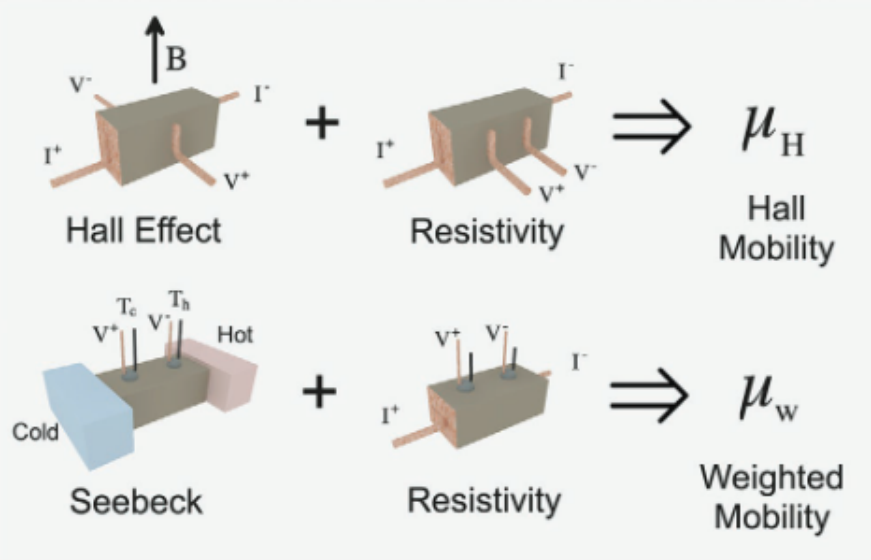

Figure 5: Hall mobility is determined through Hall effect and electrical resistivity measurements, while weighted mobility is derived from the Seebeck coefficient and electrical resistivity measurements, offering comparable insights into charge transport mechanisms. [43]

Figure 6 provides an overview of all the scattering mechanisms that occur in TE materials. When charge carriers enter a polycrystalline material, they scatter due to GBs and second phases. Doping, a key method for improving ZT, results in the creation of point defects (such as vacancies and extrinsic doped defects) and the segregation of impurities at the boundaries. These atomic-scale defects interact with charge carriers, causing scattering. At the nanometer scale, doping leads to the formation of precipitates and the generation of grain dislocations during synthesis, both of which also scatter charge carriers. In addition, the interaction between charge carriers and phonons is also considered a scattering mechanism. In a homogeneous material, multi-carrier scattering mechanisms, including acoustic phonon scattering, alloy scattering, ionized impurity scattering, and polar optical phonon scattering, contribute to carrier transport using the Matthiessen rule. As shown in equation 19, the total scattering rate (the reciprocal of relaxation time) is the sum of each scattering mechanism's scattering rate using the Matthiessen rule. However, this rule breakdown is in the case of GBs, second phases, and other inhomogeneous scattering mechanisms. [44]

$$\tau^{-1}(\mathbf{k}) = \tau_{\mathrm{IIS}}^{-1}(\mathbf{k}) + \tau_{\mathrm{APS}}^{-1}(\mathbf{k}) + \tau_{\mathrm{OPS}}^{-1}(\mathbf{k}) + \ldots \tag{19}$$

A semi-classical description of electrons and phonons is used to rationalize the general features of complex scattering equations, such as temperature dependence. The concept of a scattering cross-section is applied to relate the vibrational amplitude of atoms, and then to temperature via the equipartition theorem. From the scattering of charge carriers by atom motion and impurities, the scattering rate can be obtained by the average velocity, which has a temperature dependence for metal or degenerate semiconductors and both temperature and

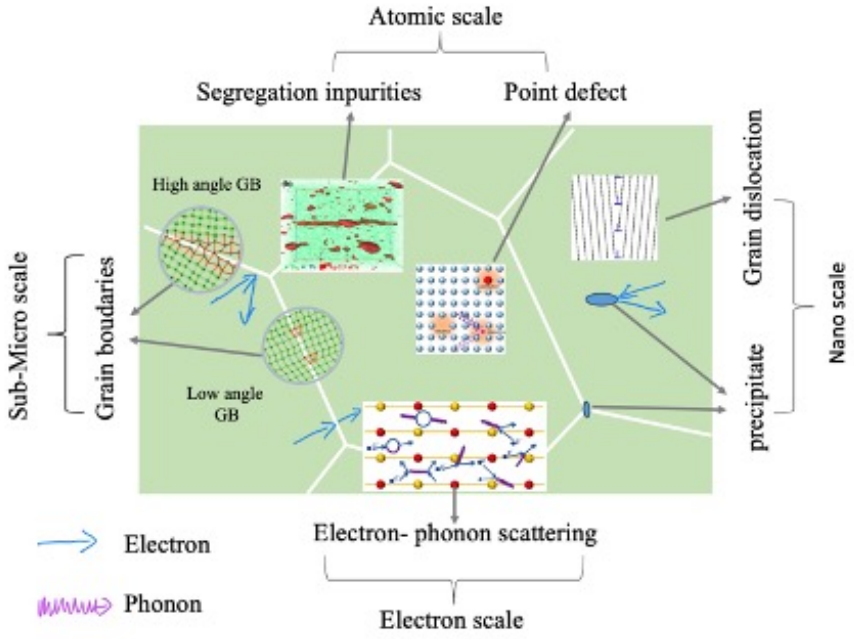

Figure 6: Different carrier scattering mechanisms occurring in the TE material.

energy dependence for semiconductors. According to equation 18, the temperature dependence of conductivity or carrier mobility becomes a crucial characteristic in identifying the dominant scattering mechanism in TE materials. Figure 7 summarizes the temperature-dependent mobility $\mu(T)$ under typical charge carrier scattering mechanisms. Here, we first briefly introduce these scattering mechanisms.

2.1.3.1 *Acoustic phonon scattering*

In the periodic lattice, each unit cell has both acoustic and optical phonons. Acoustic phonons have lower frequency and energy than optical phonon modes. They are induced by the vibrations of atomic cores in lattices. Generally, longitudinal acoustic phonon scattering dominates in most TE materials, especially lead chalcogenides. When an acoustic phonon wave propagates through a crystal lattice, it induces a local strain that affects the energy bands, and causes the scattering of charge carriers. The strength of the interaction between the charge carriers and phonons is quantified by the deformation potential, as illustrated in Figure 8. The mobility in deformation potential scattering can be obtained by:

$$\mu_0 = \frac{\pi\hbar^4}{\sqrt{2}} \frac{e}{m_I^*} \frac{C_l}{\left(m_b^* k_B T\right)^{3/2} \Xi^2} \tag{20}$$

in which the inertial effective mass m_I^*, the effective mass m_b^* from the band structure, the longitudinal elastic constant C_I, the deformation potential Ξ, calculated from the average interaction matrix element obeying Fermi's golden rule. Under a single parabolic band model, the carrier mobility in semiconductors for acoustic phonon scattering can be expressed as $\mu \propto T^{-1.5}$. This relation stems from the classical

Scattering mechanism	Relaxation time τ		Mobility $\mu(T)$	
	Non-degenerate semicoductor	Degenerate semicoductor	Non-degenerate semicoductor	Degenerate semicoductor
Acoustic phonon scattering	$T^{-3/2} \cdot E^{-1/2}$	T^{-1}	$T^{-3/2} \cdot E^{-1/2}$	T^{-1}
Optical Phonon scattering	$T^{-3/2} \cdot E^{1/2}$	T^{-1}	$T^{-3/2} \cdot E^{1/2}$	T^{-1}
Ionized impurity scattering	$T^{3/2} \cdot E^{3/2}$	T^{0}	$(m^*)^{-3/2} \cdot T^{3/2} \cdot E^{-1/2}$	T^{0}
Gran boudary scattering			$\mathrm{Le}\frac{1}{2\pi m^* k_B T}^{1/2} \exp(-\frac{E_b}{k_B T})$ L is the grain size, k_B is Boltzmann constant, E_b is potential barrier height caused by the grain boudary	

Figure 7: Scattering mechanisms and their respective temperature dependence of carrier mobility.

kinetic energy $\frac{1}{2}mv^2 \sim k_B T$ and an additional T^{-1} dependence in the scattering rate, where m^* represents the carrier mass, v is the average velocity of semi-classical charge carriers, k_B is the Boltzmann constant, and T denotes the temperature. The acoustic phonon mechanism usually dominates charge transport, especially in the high-temperature ranges. [45]

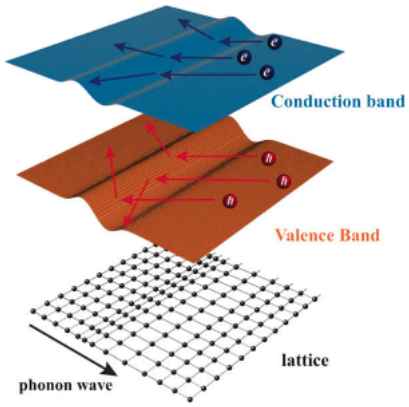

Figure 8: Deformation potential causes the energy alteration of the conduction and valence bands in a crystal due to a phonon wave, leading electron-phonon scattering. [46]

2.1.3.2 *Optical phonon scattering*

Differing from acoustic phonon scattering, optical phonon scattering possesses an invariant frequency and higher energy and frequency. Depending on different chemical bonding in unit cells, the optical phonon scattering can be divided into two types. One is non-polar optical scattering in a material with covalent bonding, such as silicon and germanium. It comes from long wavelength oscillations in the lattice, involving small displacements of tens to thousands of atoms. This small atomic displacement also induces a deformation potential

similar to acoustic phonons. However, the scattering efficiency of optical phonons is relatively low compared with polar optical phonon scattering. The other one is polar optical scattering in ionic semiconductors. In polar scattering, short wavelength oscillations of atoms on different sub-lattices vibrating out of phase produce an effective dipole moment. The oscillations of atoms with opposite charges not only cause an atomic displacement, but also induce a dipole moment, which is the origin of an extra potential. This polarizability also scatters charge carriers. This interaction between charge carriers and optical phonons is quantified by the Fröhlich interaction. The mobility in Fröhlich interaction scattering can be obtained as:

$$\mu_0 = \frac{e}{\sqrt{2}\pi\hbar^3} \frac{1}{\left(m_b^* k_B T\right)^{3/2}} \frac{1}{\Xi^2} \frac{1}{\sqrt{\varepsilon_0 \varepsilon_\infty}} \tag{21}$$

in which the effective mass m_b^* from the band structure, the longitudinal elastic constant C_l, the deformation potential Ξ, calculated from the matrix element, the static dielectric constant ε_0, and the high-frequency optical constant ε_∞. [47, 48] Materials with a small effective mass, small static dielectric constant, and high optical phonon Debye temperature (close to Debye temperature) tend to have weak polar optical phonon scattering and, hence, high carrier mobility. The polar optical phonon scattering mechanism adopts the polarization theory to analyze lattices with large ionicity, and the perturbation theory to analyze lattices with small ionicity. When the temperature is higher than the Debye temperature, the carrier mobility is $\mu \propto m^{*-1/2} E^{0.5} T^{-1}$, adopting the relaxation time approximation. Furthermore, charge carriers might screen the influence of the polarization and reduce the scattering strength of polar optical phonons.

2.1.3.3 *Ionized impurity scattering*

The ionized impurity in a doped semiconductor provides an electron for the conduction band or a hole for the valence band. As a result, the remaining atom core becomes a positively charged ion for donor impurity and a negatively charged ion for acceptor impurity. The ionized impurity atoms residing in the lattice act as scattering centers to carriers. Around ionized impurities, the Coulomb potential locally scatter charge carriers. The relaxation time for ionized impurity scattering follows the relation $\tau_{IIS} \propto T^{-3/2}$. The ionized impurity scattering is more significant at low temperatures. In addition, as ionized impurity scattering is caused by Coulomb interaction in nature, it will mostly be screened in heavily doped semiconductors.

In polycrystalline materials, an upward trend of carrier mobility with increasing temperature is mainly attributed to ionized impurity scattering and GB scattering. [49, 44]. Because a similar temperature dependence of carrier mobility is observed in both ionized impurity scattering and GB scattering, it is challenging to distinguish the dominant carrier scattering mechanism between GB scattering and ionized impurity scattering. [49]

2.1.3.4 *Grain boundary scattering*

The GB effect on carrier mobility is especially obvious when the grain size becomes comparable to the electron mean free path in nanostructure materials. In order to reduce the impact of various GBs on carrier mobility, various syntheses, such as hot press (HP) and spark plasma sintering (SPS), have been applied to retain reduced mobility. [50, 51] However, this study has been hindered by experimental limitations. Meanwhile, phonon transport can still be scattered by GBs. The selection of desired phonons to reduce thermal conductivity has attracted many studies. Since GB scattering is the main context in this thesis, it will be explained in detail in the next section.

2.1.4 *Grain boundary scattering in thermoelectric materials*

When developing TE material systems, the first step of optimization is often to regulate the carrier concentration of the material to reach an optimized range. The second optimization step is often the introduction of various defects to enhance the scattering of phonons and suppress the lattice thermal conductivity to improve the TE optimum. The ideal defect strongly scatters phonons without significantly affecting the charge carriers.

As a common defect type, point defects often have a significant effect on carrier mobility. The experimental results of the $PbTe_{0.7}Se_{0.3}$ alloy show that the introduction of point defects can effectively reduce the lattice thermal conductivity, but the carrier mobility is also significantly reduced, resulting in a decrease in the TE figure of merit. [52]

GBs, two-dimensional defects, are frequently utilized to diminish lattice thermal conductivity to enhance the ZT value in TEs. The grain refinement strategy has been widely used in the past. The calculations for polycrystalline silicon give a theoretical foundation and demonstrate the fact. [53] When the mean free path of phonons in the material is much larger than that of electrons, it was thought that refining the grains on a scale above the electron free path could effectively reduce the lattice thermal conductivity without sacrificing electrical conductivity. This theory has been verified in the SiGe alloy. However, Mg-based alloys behave differently. In $Mg_{3.2}Bi_{1.5}Sb_{0.49}Te_{0.01}$ alloy, a strong GB scattering causes smaller grains to increase electrical conductivity, ultimately worsening the TE performance. [44]

When GB scattering has a significant effect on carrier transport, a thermally activated conductivity is observed, and it vanishes at high temperatures. These thermally activated conductivities have been reported for many material systems, as shown in Figure 9 (A). The thermal activation behaviour is often attributed to the GB scattering. However, it is still challenging to study the GB scattering in detail due to the complexity of the GBs. The composition variations, distortions, and second phases near the GBs have also influenced the properties of this region. So, it cannot be simply considered a thin layer of interfaces.

To sum up, optimal design of TE materials requires an in-depth insight into each scattering mechanism and its effect on the material. Hence, various models related to GB scattering is briefly explained.

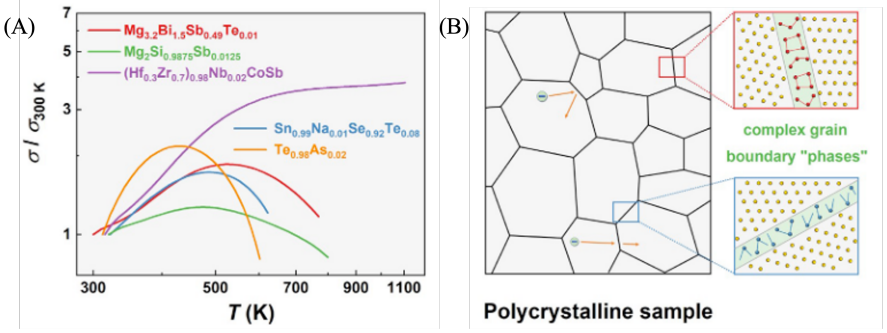

Figure 9: (A) Thermal activation behaviour for the electrical conductivity σ of a series of compounds; (B) Schematic diagram showing the complexity of the grain boundary region. [54]

2.1.4.1 *The model describing grain boundary scattering*

For metals and some heavily doped semiconductors, Matthiessen's rule is used to analyze the conventional GB transport. [55, 56] It assumes that the total scattering rate is the sum of individual scattering rates with each scattering mechanism, such as GB scattering and acoustic phonon scattering ($\tau^{-1} = \tau_{APS}^{-1} + \tau_{GBS}^{-1}$). Each scattering mechanism is treated as independent. This approach is designed for homogeneous systems, where GBs contribute to the overall carrier scattering along with other scattering mechanisms.

For electronic oxides such as ZnO and $SrTiO_3$ ceramics, the GB scattering is also observed, where the electrical property at the GBs can behave differently from those of the grains. [57, 58, 59] Matthiessen's rule is not applicable to these inhomogeneous systems.

A simple model (the brick layer model) is proposed to understand the GB. It simplifies the analysis of resistive GBs by considering a series and parallel combination of grains and GBs. The parallel contribution through the GB can be ignored entirely. The resulting series circuit part mainly contributes to the overall average resistivity, scaled with the average grain size d, which can be described in the following equation:

$$\rho_{total} = \rho_G + \rho_{GB}/d \tag{22}$$

in which ρ_{total} is the total resistivity, ρ_G is the resistivity of the grain, ρ_{GB} is the resistivity of the GB, and d is the average grain size. [60] Because of the inhomogeneity and variations in the GB resistance within a sample, the effective GB resistivity can be thought of as being dominated by the easiest path across the resistive grain boundaries. The effective grain size is determined by the high-angle GBs, which are typically more resistive than twin and low-angle GBs. Equation 22 facilitates complete characterization of the GB effect, requiring only the grain size to determine the macroscopic distance between boundaries,

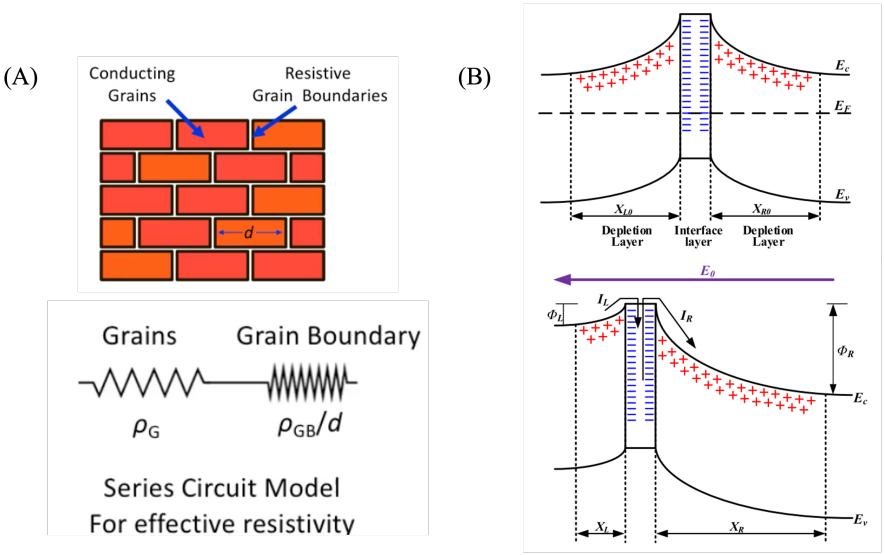

Figure 10: Schematic diagram of (A) bricklayer model [60] and (B) the Schottky barrier model.[61]

without the need for detailed resistivity profiles at the nanoscale or the thickness of the interfacial region.

The Schottky barrier model is is another frequently used approach for describing GB scattering in oxide semiconductors. As illustrated in Figure 10, the GB region has a back-to-back Schottky barrier. This barrier is caused by band bending at the junction between two dissimilar materials. Electrons can either tunnel through the barrier or be thermally excited over the barrier, where the transport is described by the Richardson equation, which predicts a thermally activated conductivity. The Richardson equation is written as:

$$\sigma = AT\exp(-\frac{\Delta E_b}{k_B T}) \tag{23}$$

where A is a prefactor, σ is the electrical conductivity, ΔE_b is the barrier at the GB region, k_B is the Boltzmann constant, and T is the absolute temperature. [62]

The Poole-Frenkel effect describes the field-assisted emission of carriers from traps, often at the GBs, and is useful for understanding non-ohmic current conduction in various dielectric and semiconductor materials. [63] In the Poole-Frenkel effect model, the free charge carriers are often considered to be trapped by the defect states in order to transport charge. In order to transport, they must be excited out of the trap states into the conduction bands. This charge carrier excitement can be considered a reduction in the effective number of charge carriers rather than a decrease in the mobility. Regardless of the interpretation, the resultant conductivity is thermally activated. The electrical conductivity is given by the Poole-Frenkel equation, which is expressed as:

$$\sigma \approx A\exp(-\frac{\Delta E_b}{k_B T}) \tag{24}$$

Alternatively, the classical hopping over a barrier is also a model to study the transport of carrier at the GB. [64] Any one of these models

or their combination could explain the observed thermally activated temperature dependence of the electrical conductivity.

2.1.4.2 *Trapping state grain boundary model*

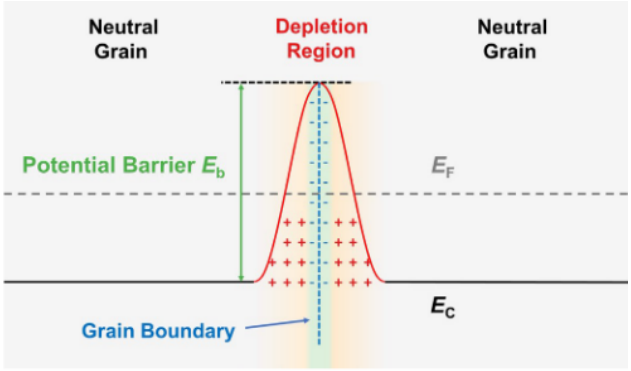

Figure 11: Schematic diagram showing the energy band near the grain boundary region of an n-type polycrystalline Si. [**kamins1971Hall**]

Currently, the most widely used models to describe GB scattering in TE materials are the trapping state GB model and the two-phase model. According to the model in Figure 11, the origin of GB scattering can be described as follows (as an example for n-type materials): the presence of a large number of incomplete bonds at GBs form trapping states which can capture free carriers. These states capture electrons, lower their concentration, and cause a shift in the Fermi energy levels E_F, driving electrons from the grain to the GB. The conduction band bends upwards to maintain the equilibrium of the Fermi energy level and creates a potential barrier that hinders the movement of carriers between the grains.

In the GB region, charge carriers with high energy ($E > E_b$) can overcome the potential barrier, generating thermionic emission current. A small number of low-energy carriers ($E < E_b$) can tunnel through the barrier, producing tunneling current via quantum mechanism tunneling. Under the small applied voltage V_a across the GB region, the thermionic emission current density J_{th} is presented as:

$$J_{th} = qn\left(\frac{k_B T}{2\pi m^*}\right)^{1/2} \exp\left(-\frac{qV_b}{k_B T}\right)\left[\exp\left(\frac{qV_a}{k_B T}\right) - 1\right] \tag{25}$$

where q is the charge of the carrier (electron), n is the density of the carriers in the depletion region, k_B is Boltzmann's constant, T is the temperature in Kelvin, m^* is the effective mass of the carrier, V_b is the barrier height measured in volts, and V_a is the applied voltage. [65]

For small applied voltages (V_a), we assume:

$$qV_a \ll k_B T \tag{26}$$

In this case, we can expand the last exponential function term, using a first-order Taylor expansion:

$$\exp\left(\frac{qV_a}{k_BT}\right) \approx 1 + \frac{qV_a}{k_BT} \tag{27}$$

Substituting this into equation 25:

$$J_{th} = qn\left(\frac{k_BT}{2\pi m^*}\right)^{1/2} \exp\left(-\frac{qV_b}{k_BT}\right)\left[\left(1+\frac{qV_a}{k_BT}\right)-1\right] \tag{28}$$

Simplifying the terms inside the bracket:

$$J_{th} = qn\left(\frac{k_BT}{2\pi m^*}\right)^{1/2} \exp\left(-\frac{qV_b}{k_BT}\right)\cdot\frac{qV_a}{k_BT} \tag{29}$$

$$= q^2n\left(\frac{k_BT}{2\pi m^*}\right)^{1/2} \exp\left(-\frac{qV_b}{k_BT}\right)\frac{V_a}{k_BT} \tag{30}$$

$$= q^2n\left(\frac{1}{2\pi m^* k_BT}\right)^{1/2} \exp\left(-\frac{qV_b}{k_BT}\right)V_a \tag{31}$$

According to Ohm's law, the relationship between the current density J_{th} and the applied voltage V_a follows a linear resistive behavior:

$$J_{th} = \sigma E = \sigma\frac{V_a}{L} \tag{32}$$

in which σ is the electrical conductivity, E is the electric field, and L represents the grain size.

By comparing equations 31 and 32, we derive the formula for the conductivity σ_{GB} in the GB region:

$$\sigma_{GB} = Lq^2n\left(\frac{1}{2\pi m^* k_BT}\right)^{1/2} \exp\left(-\frac{qV_b}{k_BT}\right) \tag{33}$$

Finally, we use the energy E_b measured in joules to replace qV_b, simplifying the formula as:

$$\sigma_{GB} = Lq^2n\left(\frac{1}{2\pi m^* k_BT}\right)^{1/2} \exp\left(-\frac{E_b}{k_BT}\right) \tag{34}$$

The potential barrier height E_b is determined as:

$$E_b = \begin{cases} \frac{q^2d^2N}{8\varepsilon} & \text{if } dN < Q_t \\ \frac{q^2Q_t^2}{8N\varepsilon} & \text{if } dN > Q_t \end{cases} \tag{35}$$

where q is elementary charge, Q_t is the density of trapping states at the GBs, and N is the concentration of the ionized impurity atoms. [64] Since most TE materials are heavily doped semiconductors, E_b here is calculated by the equation in the case $dN > Q_t$. In order to determine the E_b, the Arrhenius method is applied to determine the E_b on the $\sigma - T$ data. E_b is the negative value of the slope in the plot of $\ln(\sigma T^{1/2})$ versus $1/k_BT$.

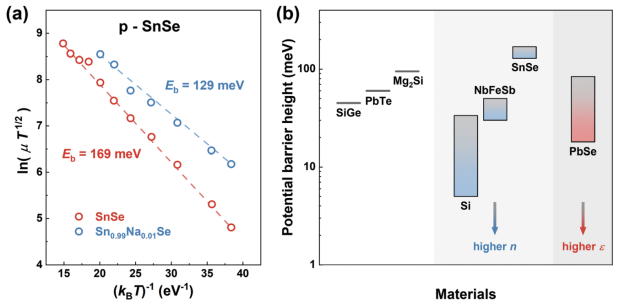

Figure 12: The potential barrier heights for various materials are determined using this method. [54]

The barrier heights vary from material to material. Even in the same material, a large variation in the barrier height also appears, which is mainly influenced by the carrier concentration and the dielectric constant. For instance in Figure 12, the different values of E_b are extracted in SiGe, PbTe, and Mg_2Si. In Si, NbFeSb, SnSe and PbSe, the values of E_b vary across a range as the carrier concentration and dielectric constant change. [54]

2.1.4.3 *Two-phase grain boundary model*

In TE materials and ceramics, the wider depletion zone and lower carrier concentration near the GB are the two reasons why Matthiessen's rule cannot be applied here. The depletion zone is several times wider than the GB region. The carrier concentrations near the GB and inside the grain are also far apart. Due to the high screening ability in metals, Matthiessen's rule is applied to deal with the GB scattering, assuming that scattering mechanisms are independent. It is not suitable to use the rule under this condition in TEs. Instead, the two-phase model is proposed by the Snyder group to illustrate the GB scattering mechanism. [66]

As shown in Figure 13 (b), the grain phase is a resistance in a crytal, while the GB phase is considered as a thermally activated resistance with a band offset ΔE, which is the same as the potential barrier E_b in equation 34. These two phases are consist of the series circuit configuration.

Under the assumption that the carrier concentration is constant between these two phases, the transferred charge carriers induce the band structure shift in the GB region. The $E_{f,GB}$ in the GB region is higher than $E_{f,G}$ in the grain region. The Fermi level in a GB phase is given as:

$$E_{F,GB} = E_{F,G} - \Delta E \tag{36}$$

Since the band offset ΔE is a empirical linear form, it can be described as:

$$\Delta E = \Delta E_0 + \alpha E_{F,G} \tag{37}$$

where ΔE_0 reference band offset at $E_{f,G} = 0$, a is a coefficient.

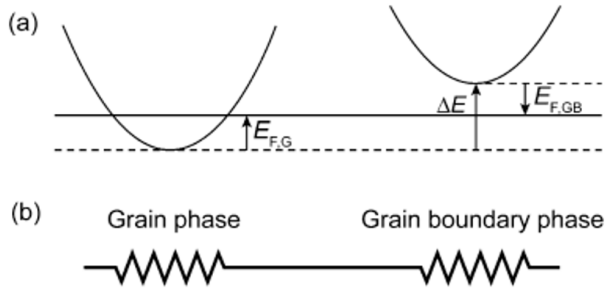

Figure 13: The two-phase model for grain boundary scattering.[44]

The electrical conductivity σ and Seebeck coefficient S of the grain and the GB phases can be calculated by the transport equations.

$$\sigma = \sigma_{E_0}(T) s F_{s-1}(\eta) \tag{38}$$

$$S = \frac{k_B}{e}\left[\frac{(s+1)F_s(\eta)}{sF_{s-1}(\eta)} - \eta\right] \tag{39}$$

in which $\sigma_{E_0}(T)$ is a temperature dependent, but an energy independent coefficient, T is the absolute temperature, s is the transport parameter related to different scattering mechanism, k_B is the Boltzmann constant, η is the reduced Fermi level ($\eta = \frac{E_f}{k_B T}$), and $F_{s-1}(\eta)$ is the Fermi-Dirac integral. $F_i(\eta)$ is calculated as:

$$F_i(\eta) = \int_0^\infty \frac{\epsilon^i}{1 + e^{\epsilon - \eta}}\, d\epsilon \tag{40}$$

and the reduced energy ϵ is determined by:

$$\epsilon = \frac{E}{k_B T} \tag{41}$$

where E is the particle energy.

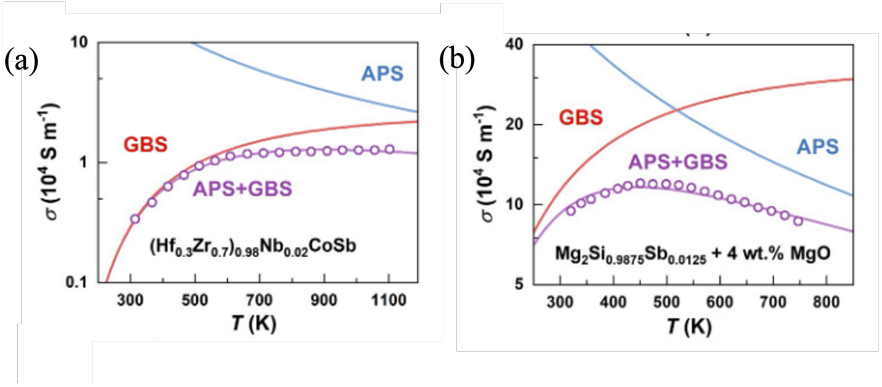

Figure 14: Temperature dependence of the electrical conductivity (σ) for (a) $(Hf_{0.3}Zr_{0.7})_{0.98}Nb_{0.02}CoSb$ and (b) $Mg_2Si_{0.9875}Sb_{0.0125}$ alloy with MgO. The solid curves are calculated using Equation 45. [54].

In the series circuit model of the grain and the GB phase, the total conductivity is the sum of the two phases, weighted by their size fraction, which is expressed as:

$$\frac{1}{\sigma_{total}} = \frac{1 - t_{GB}}{\sigma_{GB}} + \frac{t_{GB}}{\sigma_G} \tag{42}$$

where t_{GB} is the size fraction of the GB region. For the overall Seebeck coefficient, it is calculated as:

$$S = \frac{S_G \frac{1-t_{GB}}{\kappa_G} + S_{GB} \frac{t_{GB}}{\kappa_{GB}}}{\frac{1-t_{GB}}{\kappa_G} + \frac{t_{GB}}{\kappa_{GB}}} \tag{43}$$

where k is the thermal conductivity. Considering that t_GB is very small, the equation is simplified to:

$$S \approx S_G \tag{44}$$

Using the experimental data, we begin by extracting the reduced Fermi level η for the grain phase through equation 39. The reduced Fermi level for the GB phase is then obtained from equations 36 and 37. Finally, we apply the two-phase model to fit the electrical conductivity data.

Using the two-phase model, another fitting method is to use the combination of different scattering mechanisms in the grain and the GB phase weighted by their phase fraction. For example, in most heavily doped polycrystalline TE materials, the acoustic phonon scattering mechanism dominates in the grain phase, while the GB scattering mechanism plays a role at the GB phase. Thus, the total electrical conductivity can be expressed as:

$$\sigma_{total}^{-1} = \left(AT^{-3/2}\right)^{-1} + \left[CT^{-1/2} \exp\left(\frac{-E_b}{k_B T}\right)\right]^{-1} \tag{45}$$

in which A and C are prefactors, which contain the phase fraction of the grain and the GB phase. This expression of the total electrical conductivity derived from the two-phase model is similar to the Matthiessen's law, which is also a summation of the two conductivities caused by different scattering mechanisms. Nevertheless, two equations have different meanings. The Matthiessen law considers the summation of the collision probability, while in the two phase model, the total electrical conductivity is the sum of different temperature dependent electrical conductivities, which are caused by different scattering mechanisms at the grain and the GB phase. For Half-Heusler and magnesium silicide in Figure 14, the calculated total $\sigma(T)$ using equation 45 are in good agreement with the experimental data. The red line, denoting the fitting function for acoustic phonon scattering, aligns well with the data below 500 K. Conversely, the blue line, representing the GB scattering fitting function, accurately fits the data above 600 K.

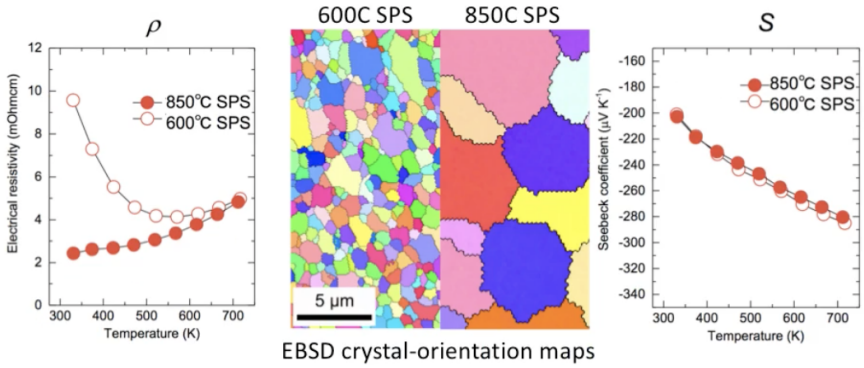

Figure 15: Temperature dependence of the electrical conductivity. [3]

2.1.4.4 *Key Factors Influencing Grain Boundary Scattering*

The main factors affecting GB scattering are the grain size, the carrier concentration, and the static dielectric constant. Grain size significantly affects the GB scattering, which is why grain refinement is initially used to enhance TE properties. In materials with strong GB scattering, smaller grain sizes lead to increased scattering. Figure 15 shows the grain size dependence of the electrical conductivity in $Mg_{3.2}Sb_{1.5}Bi_{0.49}Te_{0.01}$. [3] The sample grown at 600°C has thermally activated conductivity, while the conductivity of the sample grown at 800°C increases linearly with temperature. The EBSD images prove that a larger grain size is obtained at 800°C than at 600°C. At the same time, the Seebeck coefficient does not change much with the grain size. The modulation of grain size is easily achieved by changing the sintering conditions and other synthesis methods.

The carrier concentration is one of the factors determining the magnitude of the GB scattering. The GB scattering is more pronounced when the carrier concentration is higher. The carrier concentration can be modulated by doping or introducing defects. The conductivities as a function of temperature plotted in Figure 16 increase first and then decrease with rising Nb and Co content in (Hf, Zr)CoSb and NbFeSb half-Heusler TE materials, respectively. Thermally activated conductivities were observed only in two samples with low doping levels. [67, 4] Therefore, the GB scattering is not easy to observe in heavily doped samples. Due to the large value of the optimal carrier concentration being higher in heavily doped materials, the grain refinement strategy still works for heavily doped materials in order to enhance their TE performance.

The last factor is the dielectric constant. The larger the dielectric constant is, the smaller the GB potential barrier becomes. Slade et al. [68] have proved that the electrical conductivities decrease with more $NaSbSe_2$ doping in $PbSe$. The increase in electrical conductivity is because the dielectric constant of $NaSbSe_2$ is smaller than that of $PbSe$, which increases the GB potential barrier and increases the GB scattering.

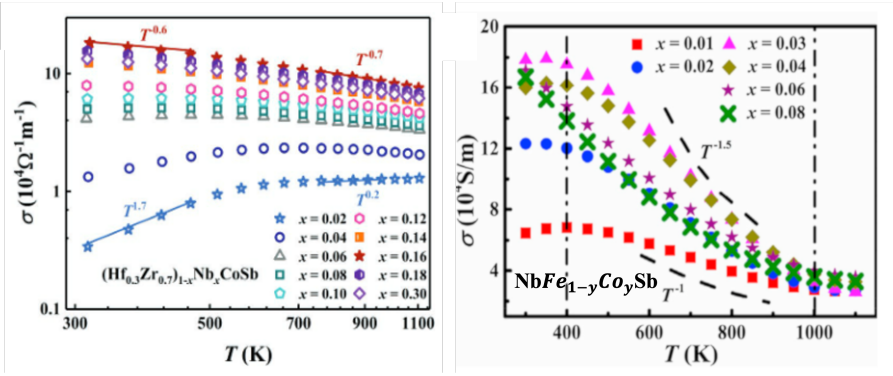

Figure 16: Temperature dependence of electrical conductivity for the $NbFe_{1-y}Co_ySb$ sample (right) with different carrier concentrations. [67, 4]

2.1.5 *Dielectric screening effect*

In a doped semiconductor, a charged ion will produce a Coulomb potential and scatter the carriers around it, as depicted in Figure 17 (a). This Coulomb potential is modified by screening from other free carriers. Free electrons or holes respond to the bare Coulomb potential by altering their distribution in space, which in turn, attenuates the potential. This modified Coulomb potential leads to weakened scattering of charge carriers, enhancing the electrical conductivity. This process is called the screening effect. [69] It is crucial for semiconductor and TE material applications. The schematic of the screening effect is described intuitively in Figure 17(b). Here, the free electrons cloud around a positively charged ion and redistribute their charge density, thereby reducing the Coulomb potential. Consequently, as an electron moves near the ion, it remains 'invisible' to it, lowering the possibility of scattering events.

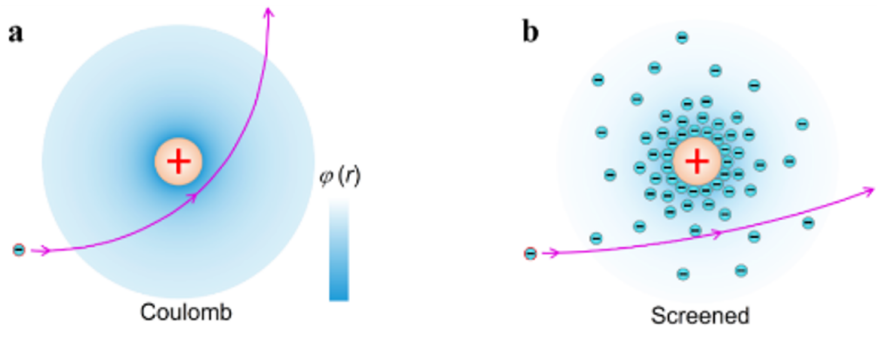

Figure 17: (a) Bare Coulomb potential field of a positive charged ion. (b) screened Coulomb potential. [70]

The Thomas-Fermi approximation is a method for approximating the screened Coulomb potential in heavily doped semiconductors. This approach provides a simplified, yet effective way to analyze the complex electron-ion interactions. The bare Coulomb potential can not describe it, $\phi(r) \propto \frac{1}{r^2}$, any more, while a new formular, $\phi(r) \propto$

$\frac{1}{r}\exp\left(-\frac{r}{r_{TF}}\right)$, should be applied. The screened potential drops more quickly than the bare Coulomb potential, and the scattering is weaker.

The degree of screening in a material is often quantified using the screening length or the Debye length. The Thomas-Fermi screening length r_{TF} is defined as:

$$r_{TF} = \left(\frac{\epsilon k_B T}{n e^2}\right)^{1/2} \tag{46}$$

In this equation, r_{TF} represents the Thomas-Fermi screening length, ϵ is the permittivity of the material, k_B is the Boltzmann constant, T is the temperature, n is the free carrier concentration, and e is the elementary charge. [26] This parameter describes the distance over which the electric field from a charged particle is significantly screened or reduced by the free charge carriers in the material. A shorter Thomas-Fermi screening length implies stronger screening, as the electric field is dropped more quickly. According to the Thomas-Fermi screening length, it depends on factors like the temperature, the concentration of free carriers, and the permittivity of the material. It is a key parameter in understanding the electrical behaviour of semiconductors, which are highly polarizable and have strong bonding strengths. Firstly, the Thomas-Fermi screening length (r_{TF}) exhibits a square root dependence on temperature, meaning the screening length decreases and the screening effect weakens with increasing temperature. This explains why ionized ion scattering and GB scattering becomes more pronounced at lower temperatures. In addition, carrier concentration is another vital factor in the screening effect. Higher carrier concentrations lead to a smaller r_{TF}, indicating a stronger screening effect, which in turn, reduces the modified Coulomb interaction. Finally, the permittivity ϵ is a measure of how easily the material can be polarized in the presence of an electric field. The response of different materials to an external electrical field is compared by the dielectric constant. A material with a higher dielectric constant is expected to have a stronger screening ability and, consequently, a smaller Thomas-Fermi length. Nonetheless, equation 46 shows that increased permittivity results in a longer screening length. This direct proportion contradicts the fact that a higher permittivity would decrease the screening length. To solve this puzzle, researchers have introduced a new metric, charge shielding ratio α_{BD}, the ratio of the effective Bohr radius to the Thomas-Fermi length, providing a more accurate metric for assessing the screening characteristics of various materials. [54] The dimensionless parameter α_{BD} is defined as:

$$\alpha_{BD} = \frac{a_B^*}{L_D} = \frac{4\pi\hbar^2\varepsilon_s n}{m_b^* e^2\sqrt{N_v k_B T}} \tag{47}$$

in which a_B^* is the effective Bohr radius, L_D is the Thomas-Fermi screening length, ε_s is the static dielectric constant, n is the free carrier concentration, m_b^* is the band effective mass, N_v is the effective density of states, k_B is the Boltzmann constant, and T is the temperature. From equation 47, α_{BD} parameter is proportional to the square

root of the dielectric constant. When ε_s increase, α_{BD} also increase, which means a stronger screening ability.

Therefore, the screening effect can be tuned by these factors to weaken the defect scattering, including ionized impurity scattering, GB scattering, and even the optical phonon scattering. Ren et al. reported that the screening effect in half-Heusler TE materials can be tuned via chemical doping in order to adjust the carrier concentration. [70] Su et al. also clarified that an effective control of the screening in defects at GBs is achieved by attenuating the dielectric constant though the composition, leading to reduced GB scattering and optical phonon scattering in perovskite photovoltaics. [71]

2.2 FUNDAMENTALS OF METAVALENT BONDING

Functional materials have been developed to meet the increasing demands of semiconductor products. Phase change materials (PCMs) are used in optical storage applications, where a larger data storage capacity requires a large optical contrast between the crystalline and amorphous states. TE materials, on the other hand, are utilized in power generation that demand a high heat-to-electricity conversion efficiency by balancing thermal conductivity and the power factor. Similarly, superconductors are developed for applications that operate near room temperature, demanding a high critical temperature by strengthening the Cooper pairing of electrons.

Design a material with desired properties is a key step in the development of functional materials. Traditional approaches to material design in physics begin with a specific atomic arrangement, calculate the resulting band structure, and then predicts the physical propertiesto to ensure application requirements. Scientific method, such as X-rang diffraction and electron microscopy, are the common techniques to investigate the atomic arrangement. The strong correlation between atomic arrangement and physical properties enables tailoring the physical properties of materials by modifying the atomic arrangements. How these atoms are arranged and what specific atomic structures form determine a material's chemical bonding. The chemical bonding is the interaction between atoms that holds them together in solid. The link between the chemical bonding and the atomic arrangement of materials has been well studied. If we can establish a direct link between chemical bonding and physical properties, we propose a new approach in material design. This approach starts by quantifying chemical bonding with specific descriptors to predict physical properties, allowing for target applications. To quantify the chemical bonding in materials, we employ a material map, providing a direct link between the chemical bonding and the physical properties. This map is based on quantum chemical descriptions. The electron transfer and sharing between atoms are chosen as the map descriptors and calculated by quantum calculation tools. [72, 73] Thus, the material map serves as an effective method to tailor the material's property by modifying the chemical bonding.

This section introduces the basics of metavalent bonding and its evolution. Then, the fingerprint and characteristics of metavalently bonded solids are summarized. At the end, the section also investigates the unique bond rupture in metavalently bonded compounds, quantitatively meassured by the probability of multiple events (PME) in APT.

2.2.1 *Basic of metavalent bonding*

2.2.2 *Evolution of map for chemical bonding*

The first and widespread map is a Van Arkel–Ketelaar triangle, a tool used to represent and classify compounds based on their chemical bonds. It has been proposed by two Dutch scientists Anton Eduard van Arkel and Jan Antonie Arie Ketelaar in 1941. [74] The triangle is divided into four regions, each representing a different type of chemical bond: covalent, ionic, metallic and other chemical bonding. Compounds are positioned within the triangle based on their electronegativity difference and average electronegativity. The map is empirical and does not have atomic structure dependency. For example, the graphene and diamond have distinct structures, but they are located in the same point in the map.

The quantum theory of atoms and molecules provides a mean to characterize the chemical bonding upon quantum mechanics. A quantum mechanical map is generated, which employs the Schrödinger equation. Two quantities are calculated via the DFT calculation. One is the number of electrons transferred (ET) to characterize how much charge is transferred between adjacent ion cores. The case in sodium chloride is that a sodium atom loses about an electron and transfers it to a chlorine atom, resulting in a sodium ion and a chloride ion. The second quantity is the number of electrons shared (ES). The neighboring atoms exhibit electron correlation. It means that there's a probability of finding an electron in one basin and a covariance indicating the conditional probability of finding a second electron in the second basin. This concept closely aligns with Pauling's idea of electron pair formation, effectively describing shared electrons between adjacent basins. With these two quantities, a map based on quantum mechanics (QM) is created. [75] The map appears disorganized due to an issue: compounds like MgO and BaO differ from NaCl in electron transfer. Less electron transfer occurs in NaCl than in MgO, but the oxidation state of oxygen in MgO is higher than the negative electron state of chlorine in NaCl. By normalizing the charge transfer by the oxidation state, we obtain an ordered graph in Figure 18.

We can classify these compounds into different groups in the map. Metals occupy the bottom left corner of the map, characterized by no charge transfer between adjacent atoms and limited charge transfer. Van der Waals compounds lie in an area with no or small charge transfer. Ionic compounds are located the bottom right corner, where the amount of charge transfer is high, but the number of electrons shared is minimal. Covalent compounds are positioned where electron pairs form with a high degree of electron sharing. Materials like GeTe, PbTe do not fit into metallic, ionic, or covalent categories. They form their own distinct class due to their unique bonding properties that don't align with traditional bonding classifications. [75] This map succeeds in classfying the different types of chemical bonds in different areas.

Finally, a third dimension, which use the material physical properties, is added to the QM map. Figure 19 shows a series of maps,

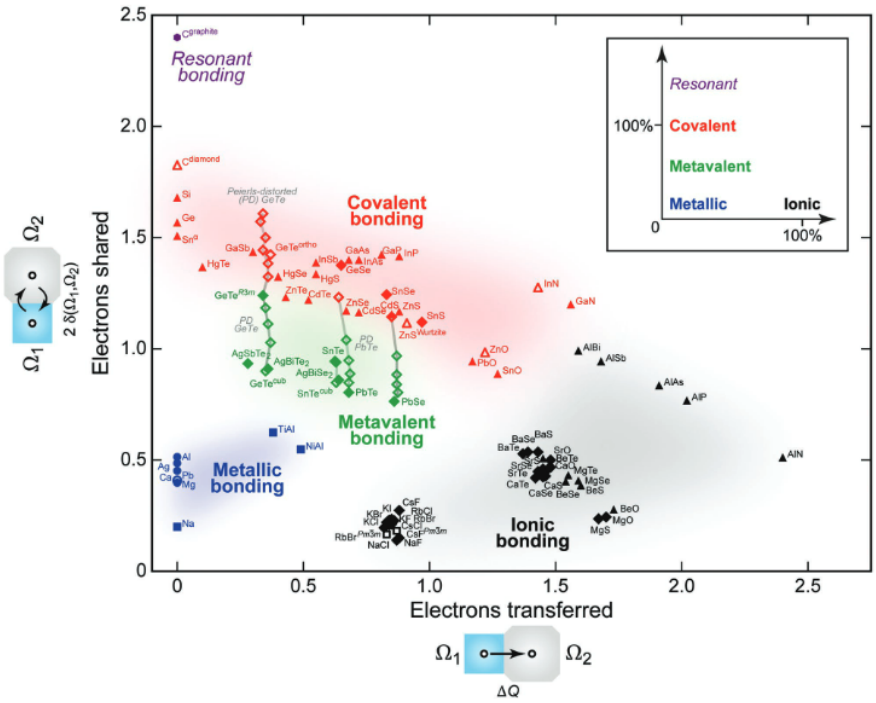

Figure 18: A two-dimensional map of electronic interactions and bonding in materials. The number of electrons transferred (x-axis) and electrons shared between neighboring atoms(y-axis) is computed using quantum-topological methods. [75]

each with the optical dielectric constant, Born effective charge, and Grüneisen parameter as the third axis. The material's position on the 2D map is determined by its calculated ET and ES values, and its experimentally measured physical properties are represented along the third axis. The different color bar represent materials with distinct bonding types: green bars for MVB, red bars for covalent bonding, and black bars for ionic bonding. The height of each bar represents the value of the corresponding material property. Metavalently bonded materials exhibit anomalously high values of these properties. [75] This 3D map helps differentiate between MVB, covalent, and ionic materials based on their physical properties. The 3D map indicates their position in 2D map and their physical properties along the third axis. Therefore, MVB can not be explained as a combination of present bonding mechanisms.

2.2.2.1 *Metavalent bonding definition*

The chemical bondings in solid are generally classified into covalent, ionic, metallic, van der Waals, and hydrogen chemical bonds. Covalent bonding forms through the sharing of electron pairs between two neighboring atoms, resulting in the localization of valence charges. Ionic bonding arises from the charge transferred between atoms, which localizes valence charges at the cation or anion sites. Metallic bonding involves the formation of a Fermi sea of delocalized valence electrons. From the map shown in Figure 18, a new bonding, called metavalent bonding (MVB), has been found. These MVB

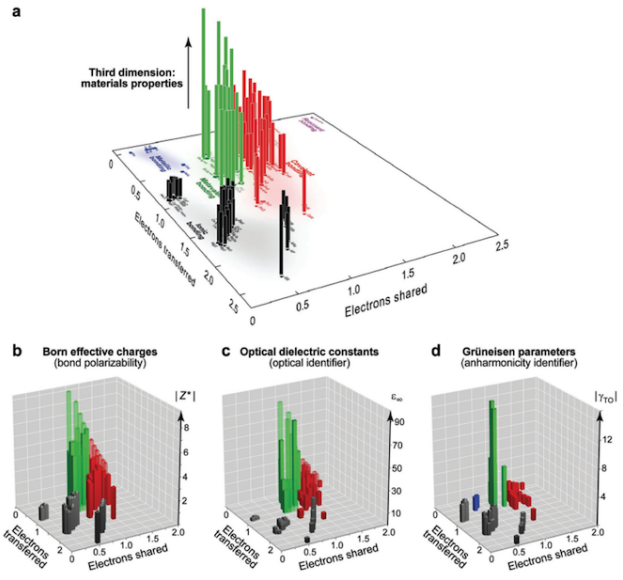

Figure 19: A 2D map with two axes for ET and ES, expanding into a third dimension, as depicted in (a). The third axis represents Born effective charge, optical dielectric constants, and Grüneisen parameter, respectively. These 3D data visualizations with different third axis is shown in (b), (c), and (d). These visualizations illustrate the distribution of three types of materials — matevalently bonded (green bars), covalently bonded (red bars), and ionically bonded (black bars) materials— within the base plane. Additionally, they displays the corresponding property values for these materials along the third axis, which varies to represent Born effective charge, optical dielectric constants, and Grüneisen parameter. The values on Born effective charge (b), optical dielectric constants (c), and Grüneisen parameter (d) for MVB materials are significantly higher than those for the other two materials. [75]

compounds locate where the average ES is around 1.0, and ET is relatively low, generally below 0.3. This bonding type lies between covalent and metallic bonding, suggesting moderate electron sharing and low charge transfer characteristics. These compounds with MVB are widely applied in PCM, TE, and topological chalcogenides.

2.2.2.2 *Evolution of metavalent bonding study*

Initially, resonant bonding has been found in crystalline PCM. This unique bonding mechanism is the fundamental reason for the large optical contrast between the crystalline and amorphous phases. The dielectric function measurement proves that the unique bondings in the crystalline PCM exhibits a high eletronic polarizability, which is characterized by Born effective charges Z^*. The unique electron configuration reveals one electron shared by two neighboring atoms, results in the distorted octahedral atomic arrangement. The nearest neighbors in the crystalline PCM are more than in covalent bonding, but less than in the close-packed atomic structure in metals. [76, 77]

There are similarities and differences of the resonant bonding between graphite, benzene and crystalline PCMs. In benzene, each car-

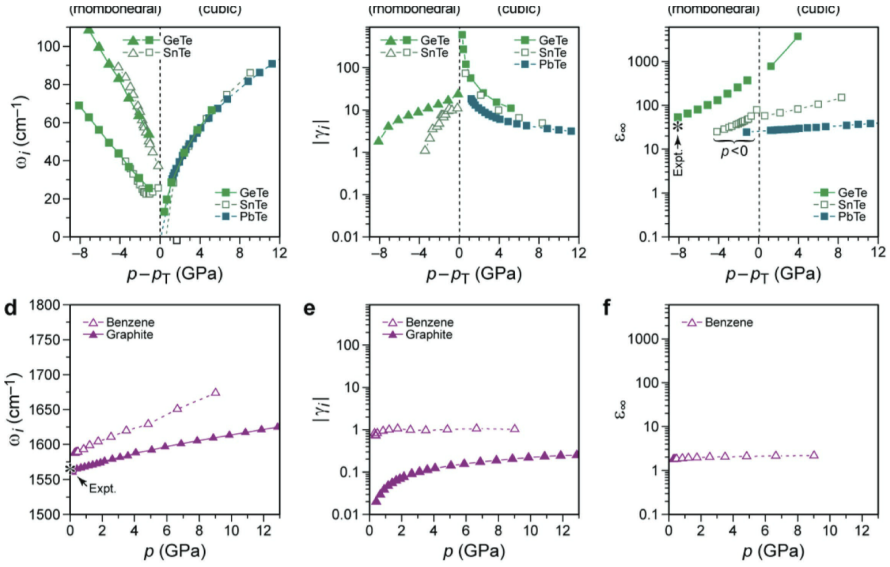

Figure 20: Physical properties of different resonantly bonded materials: (a) Phonon frequencies ω_i for transverse optical modes in GeTe, SnTe, and PbTe as a function of pressure. Since GeTe and SnTe transform from a rhombohedral to a cubic structure, the respective transition pressure is set as reference ($p_T = 8.1$ GPa for GeTe, 0.7 GPa for SnTe). (b) Absolute Grüneisen parameters, $|\gamma_i|$, for transverse optical modes, as an indicator for an anharmonic lattice instability. (c) Optical dielectric constants ε_∞, an indicator for the electronic susceptibility. [78]

bon atom has two σ bonds with neighboring carbons and one σ bond with hydrogen in the hexagonal ring, along with delocalized π bonds above and below the plane. In graphite, each carbon atom has three σ bonds within the hexagonal lattice and delocalized π bonds across the entire sheet. In the crystalline phase of PCMs, each atom only has three σ bonds, formed by the half-filled p-electrons. The octahedral atomic arrangement in crystalline PCM is intrinsically unstable towards the dimerization, or towards the charge transfer. Whereas the benzene and graphite are stable in their atomic arrangement. The pressure experiment in Figure 20 provides evidence that the chemical bonding in crystalline PCMs is distinct from the resonant bonds in benzene and graphite. The experiment measures different physical parameters, including pressure dependent phonon frequencies, specific-mode Grüneisen parameters, and optical dielectric constants in these resonantly bonded materials. GeTe, PbTe, and GeSeTe exhibit different trends and values from that of graphite and benzene. [78]

Another evidence for the differences in resonantly bonded materials comes from the distinct bond rupture observed in APT measurements. As an allotrope of graphene, carbon nanotubes have similar atomic arrangements with resonant bonds. The resonant bonds in carbon nanotubes break similarly to covalent bonds, with each laser pulse having a high probability of ejecting a single fragment. However, the unique resonant bonds in the crystalline PCMs experience distinct behaviors, characterized by a high probability of multiple events. [79] Thses two evidences suggest that the unique bonding

mechanism in the crystalline PCMs is fundamentally different from the resonant bonding in benzene and graphene. Hence, this unique chemical bonding is no longer suitable to be called resonant bonding and is redefined as metavalent bonding (MVB).

Later, five physical property fingerprints are proposed as bonding indicators to identify MVB. Metavalently bonded solids differ from covalent bonds in their behavior, approaching the metallic regime and are therefore named as "incipient metals". [80]

2.2.3 *Fingerprint of metavalent bonding*

MVB is a distinct type of chemical bonding with a unique property portfolio. So here we have five fingerprints to characterize the properties of MVB materials: electrical conductivity σ, effective coordination number ECoN, optical dielectric constant ϵ_∞, and mode specific Grüneisen parameter γ_{TO}. Employing these fingerprint as criterions, relevant properties have been determined for over 150 materials and are summarized in a table. Table 1 provides an overview of the characteristics of differently bonded materials. [80] Compared with inoic, covalent, and metallic bonding, MVB stands out due to its unique properties. MVB has a moderate electrical conductivity (10^2 – 10^4 S/cm), a high optical dielectric constant ($\varepsilon_\infty > 15$), a large Born effective charge ($Z^* = 4 - 6$), a high mode-specific Grüneisen parameter ($\gamma_{TO} > 3$) and its effective coordination number that does not follow the 8-N rule. [75] These fingerprints are discussed one by one to reveal MVB's unique portfolio.

	Ionic (e.g., NaCl, MgO)	**Covalent (e.g., Si, GaAs)**	**Metavalent (e.g., GeTe, PbTe)**	**Metallic (e.g., Cu, NiAl)**
Electronic conductivity (electrical identifier)	Very low ($< 10^{-8}$ S · cm^{-1})	Low to moderate (10^{-8}–10^5 S · cm^{-1})	Moderate (10^2–10^5 S · cm^{-1})	High ($> 10^5$ S · cm^{-1})
Effective coordination number[a] (structural identifier)	4 (ZnS), 6 (NaCl), 8 (CsCl)	8–N rule typically satisfied	8–N rule not satisfied	8 (bcc), 12 (hcp/fcc)
Optical dielectric constant ϵ_∞ (optical identifier)	Low (2–3)	Moderate (5–15)	High (> 15)	—
Born effective charges Z^* (chemical bond polarizability)	Low (1–2)	Moderate (2–3)	High (4–6)	—
Mode-specific Grüneisen parameters (anharmonicity)	Moderate (2–3)	Low (0–2)	High (> 3)	Low (0–2)

Table 1: The table is a comparison between the metavalent and other types of bonding. [80]

The electrical conductivity σ, as the first fingerprint, is an electrical identifer. Metavalently bonded solids possess moderate electrical conductivities, which range from 10^2 to 10^4 Scm^{-1}. [78] The electrical conductivity is a result of the competition between electron localization and delocalization. The electron delocalization in metal results in high σ. In contrast, ionic materials experience electron transfer

from cations to anions, creating strong electrostatic attraction and a large bandgap, with electrons tightly bound within ions, leading to very low σ. Covalent bonds involve localizing eletrons as electron pairs shared between atoms. The bandgap in covalent solids restrict free carriers, resulting in low to moderate σ compared to metals. In metavalent solids, adjacent atoms share approximately one electron, producing high electron delocalization, which means the valence electrons are not firmly bound to the adjacent ion cores. This highly electron delocalization allows for electrical conduction, but not to the extent of metals. [81]

The second characteristic fingerprint of MVB is its moderate effective coordination number (ECoN), which lies between those of covalent solids and classic metals. The ECoN represents the distance-weighted average number of adjacent atoms, making it particularly useful for identifying the trend of atomic arrangements in the structure distortion. For covalently bonded compounds, silicon follows the 8-N rule and has 4 nearest neighbor atoms. The close packed structure in metals rise the ECoN to be 8 or 12. MVB materials, like GeTe, with distorted octahedral atomic coordination, have a higher ECoN of 5.2. [80, 75] The increased ECoN of MVB does not follow the 8-N rule for covalently bonded compounds, and is lower than the one in metals.

Another defining feature of chemical bonding is the Born effective charge Z^*. It is indicative of the chemical bond polarizability and characterized the change of the polarization induced by small distortion. It quantifies the change in polarization P per unit displacement u of an atom, mathematically expressed as:

$$Z^* = \Omega_0 \frac{\partial P}{\partial u} \tag{48}$$

where Ω_0 represents the unit cell volume. [75] The metavalently bonded solids have a large Z^* value.[76] The Born effective charge is meassured by Far-infrared FTIR spectra. The parameter characterizes the sensitivity of lattice distortion and is indicative of the unique properties of MVB. MVB compounds also display a high Born effective charge that characterizes the chemical bond polarizability, leading to a significant splitting between the longitudinal and transverse optical phonons. As a consequence of the Lyddane-Sachs-Teller relation, MVB compounds exhibit a large static dielectric constant. The Born effective charge is meassured by Far-infrared FTIR spectra.

The fourth feature of MVB is a large value of specific-mode Grüneisen parameter. This quantity is linked to the lattice anharmonicity. The Grüneisen parameter for transverse optical modes γ_{TO} measures the volume dependence of frequency ω_i for a given vibrational mode, its calculation is given by:

$$|\gamma_i| = \frac{V}{\omega} \frac{\partial \omega_i}{\partial V} \tag{49}$$

in which V is the volume and ω is the frequency of the vibrational mode. The Grüneisen parameter is a measure of the anharmonicity

of the interaction potential. [80] Unlike the covalent bonding that can be modeled as springs, with atoms oscillating in a harmonic potential well, MVB exhibits significant anharmonicity. The strong anharmonicity in MVB materials leads to a decrease in thermal conductivity. This feature is exemplified by PbTe, [82] a material with low thermal conductivity that is further studied in Chapter IV and V for its grain boundary scattering mechanisms.

One key characteristic of metavalent bonding (MVB) is its high optical dielectric constant, ϵ_∞, which probes the electronic polarizability of valence electrons in metavalent compounds. The optical dielectric constant, ϵ_∞, is the component of the dielectric function $\epsilon(\omega)$ that specifically measures the material's ability to polarize in response to an external electric field at high frequencies. The dielectric function, $\epsilon(\omega)$, quantifies the material's overall response to an external electric field across a range of frequencies, with ϵ_∞ capturing this response at high frequencies. [83, 84] The electronic configuration of MVB, with one electron shared by two neighboring atoms, causes pronounced electron delocalization in MVB, leads to a significantly increased electronic polarizability. [83] This is because the highly delocalized valence electrons in metavalent compounds are less tightly bound, allowing them to respond more strongly to external electric fields. This fast response enhances the material's polarizability and yields a high ϵ_∞. In addition, the combination of small average band gaps and significant optical transitions due to large matrix elements results in enhanced electronic polarizability, leading to a high optical dielectric constant in MVB materials. [77, 85]

Overall, the set of fingerprints provide a comprehensive understanding of the unique physical properties of MVB, which once again confirm MVB is a new chemical bonding mechanism.

2.2.4 *Nature of metavalent bonding*

From a chemist perspective, the tyical structure of metavalently bonded materials is an octahedral-like structure. The term octahedral-like structure means that each atom has six nearest neighbours with small distortion. There are two types of octahedral-like structures in metavalently bonded materials shown in Figure 21 (a): the rocksalt structure, utilized in PbTe, and the rhombohedral structure, as employed in $GeTe$ and Bi_2Te_3. The rhombohedral structure is a disorted rocksalt atomic arrangement. The common motif of these two atomic structures is that each atom has six neighboring atoms. For rocksalt structures, such as PbTe, since the s-orbital is lower in energy than the p-orbital, the p-electron is responsible for the bond formation. Pb and Te atoms contribute six p-electrons in total. Each atom has an average of three p-electrons for six neighboring atoms. To form six electron pairs, six electrons per atom are required. With three p-electrons available for six neighboring atoms, each bond between two atoms occupies only one electron. Thus, metavalently bonded materials are charac-

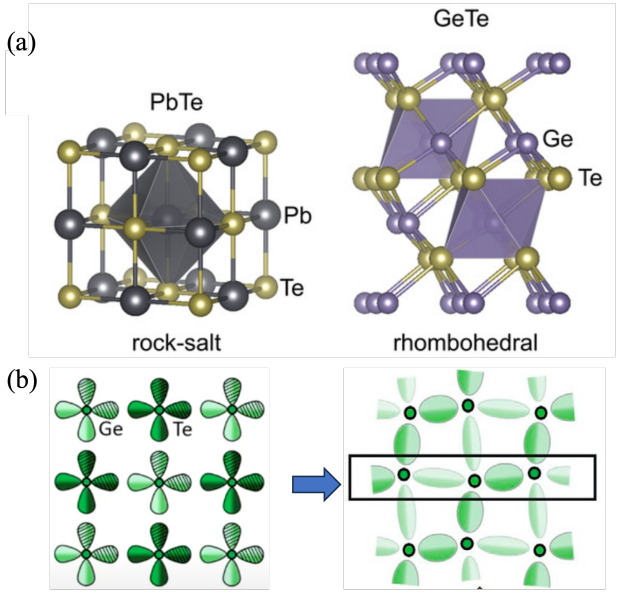

Figure 21: (a) Typical octahedral-like structures in metavalently bonded materials. [86] (b) half-filled σ bond of p electron in GeTe, a typical metavalent bonded material. [87]

terized by the octahedral-like atomic arrangement, not terahedra-like atomic arrangement.

2.2.4.1 *The bond and band structure of metavalent bonding*

The nature of MVB is dominated by p-electrons in σ-bonds. The large energy difference between s- and p-orbitals makes the contribution of s-electrons negligible. In the case of GeTe, shown in Figure 21 (b), the p-electrons along the (001) plane demonstrate an overlap between adjacent p orbitals. In the octahedral atomic structure, each atom has three p electrons. Overall, one electron is shared between two neighboring atoms, forming a σ bond. The σ-bonds formed by p-electrons are only partially filled, unlike the electron pairs that form covalent bonds.

From the physics perspective, the band structure of metavalent solids is characterized by a narrow band gap, which is a result of the instabilities of the incipient metallic state. The instabilities are caused by the ET and ES induced by the distortion. For instance, the σ bonds in GeTe are formed from p-orbitals, which are occupied by about half an electron pair (ES = 1), resulting in a metallic band (blue curves on the left of Figure 22 (a)). However, a Peierls distortion, a common type of distortion in MVB material, opens a narrow gap in the band structure and reduces the energy of the occupied states. In the density of states diagram in Figure 22 (a), the occupied states decrease from the blue region (metallic band structure) to the green region (MVB band structure) after the band gap opens. The states below the energy gap will be completely occupied, while the ones above the gap will remain unoccupied, resulting in a transition from a metal to a semiconductor. [88] This metal-semiconductor transition has an influence on the electrical conductivity. The range of electrical conductivity in

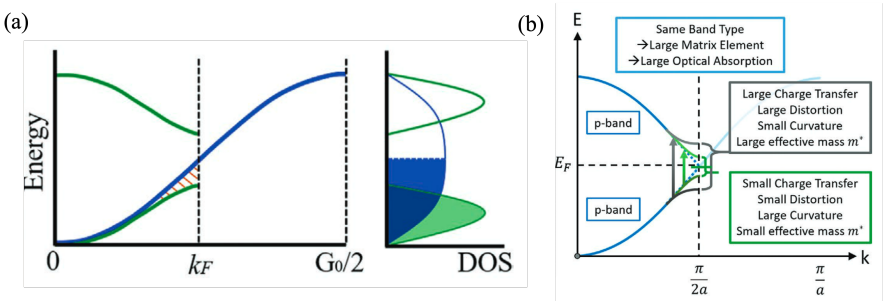

Figure 22: (a) Band structure (left) and density of the state (right) of metavalently bonded materials. [86] (b) modification of band gap by electron sharing and electron transfer. [87]

metavalently bonded solids is between 10^1 and $10^4 S \times cm^{-1}$, which approaches the typical range of metals (around $10^5 S \times cm^{-1}$). [86] With the increase of the Peierls distortion, the electrical conductivity in metavalently bonded solids decreases.

The modulation of the band gap in metavalently bonded materials can be achieved by tuning the degree of electron sharing (ES) and electron transfer (ET), which directly influence the electronic structure and the physical properties. As shown in Figure 22 (b), the electron sharing in metavalently bonded materials can be adjusted by the degree of Peierls distortion. A higher degree of Peierls distortion increases the band gap. For a larger band gap, the E-k curve has less curvature, indicating a larger effective mass, as the effective mass is linked to the second derivative of E with respect to k. Similarly, increased electron transfer between atoms also widens the band gap, flattening the E-k curve and resulting in a higher effective mass.

The QM map not only confirms the existence of MVB, but also helps to predict material properties based on its position within distinct bonding regions (Figure 23). The map highlights four areas: the red region represents covalent bonding, where electrons are localized between ion cores through electron pair formation; the black region indicates ionic bonding, characterized by strong electron localization at the ion cores; the blue region corresponds to metallic bonding, featuring delocalized electrons that reduce the kinetic energy; and the green region represents the transition zone of MVB, showing a competition between electron delocalization (as in metals) and localization (as in covalent and ionic bonds). This allows for the prediction and modification of essential properties such as electrical conductivity, effective mass, and optical dielectric constant based on the positioning within the QM map.

Furthermore, while the previous analysis of the band structure illustrates how adjusting ES and ET affects the band gap to tune the properly in metavalently bonded materials, the map in Figure 23 offers another approach. By using ES and ET as the x and y axes, the map provides a broader framework to predict key properties, including their effective mass m^*, electrical conductivity σ and dielectric function $\varepsilon_2(\omega)$.

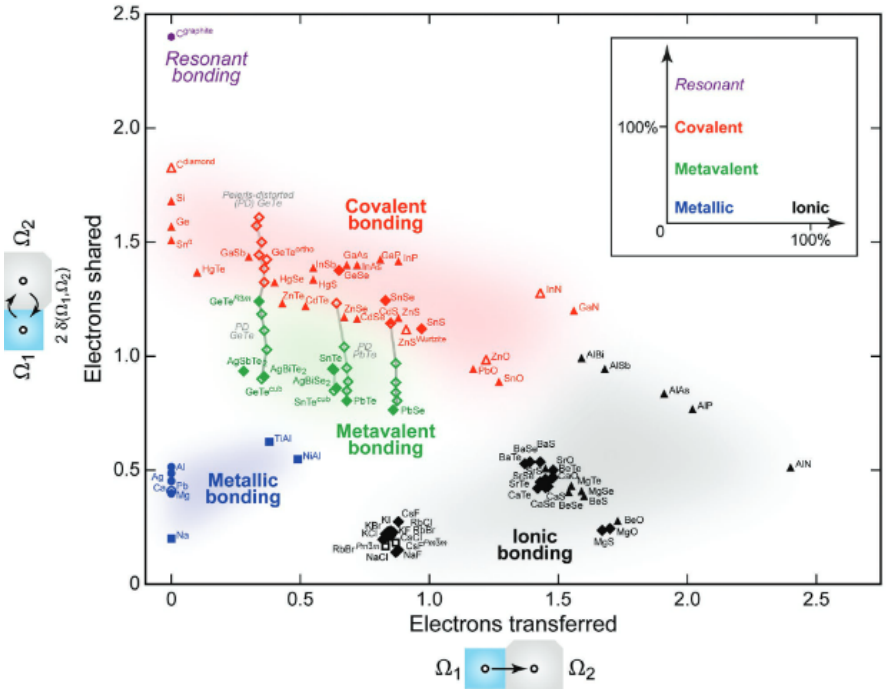

Figure 23: A two-dimensional map of electronic interactions and bonding in materials. The amount of electrons transferred(x-axis) and shared between neighboring atoms(y-axis) is computed using quantum-topological methods. [75]

To conclude, MVB features half-filled σ bonds and a band structure characterized by a narrow band gap. The QM map serves as a guiding framework to distinguish metavalent bonding from other types, predicts metavalent bonded solid's properties and enables targeted tuning of material properties by adjusting ES and ET.

2.2.4.2 *Peierls distortion*

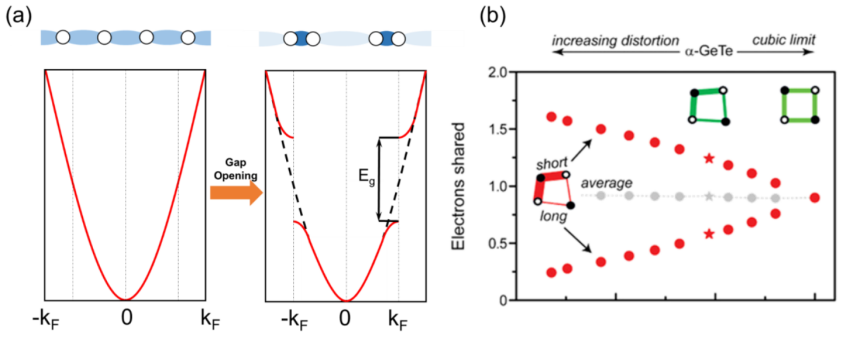

Figure 24: (a) Illustration of the Peierls distortion and the opening of an energy gap.(b)The effect of Peierls distortion on the eletron shared in GeTe. Reproduced from ref [89].

The Peierls distortion is a local distortion that occurs in periodic lattices due to a half-filled band. The Peierls distortion occurs when the energy gain due to the distortion is higher than the elastic energy,

resulting in the total energy after the distortion being lower than that of the undistorted phase. The process of the Peierls distortion is illustrated in Figure 24 (a). In a one-dimensional atomic chain with a parabolic band structure, the instability of atoms at the position of Fermi vector k_F within the Brillouin zone causes the zone to shrink. This shrinkage results in the doubling of the unit cell and leads to the formation of a narrow band gap with a size value of $2|V_{K_F}|$. [88]

Consequently, the Peierls distortion opens a band gap and alters the atomic arrangement, shifting from an ideal octahedral structure to a distorted one with three short and three long bonds. The changed atomic arrangement corresponds to a reduced value of the number of coordination (ECoN) from 6 to 3. This reduced coordination number does not follow the $8-N$ rule in semiconductors, which is also a sign denoted the distinct nature of MVB. [81, 86]

As for the electron localization, the six bonds in the ideal octahedral structure transform into three short bonds and three long bonds due to a Peierls distortion. The change of the short bond-to-long bond ratio causes a redistribution of valence charges. As the octahedral structure distorts further, more shared electrons are localized at the shorter bonds, while fewer shared electrons are left at the long bonds. During the redistribution of shared electrons, the average number of electron transferred remains constant. [75] The increased localization of shared electrons at short bonds eventually breaks down MVB and transits to covalent bond. Figure 25 indicates the transition from metavalent to covalent bonding via electron localization. The electron localization impacts on material properties, including the electrical conductivity σ, optical dielectric constant ϵ_∞, and others. The degree of Peierls distortion can be adjusted by introducing strain, alloying, creating defects and nanostructures. [75]

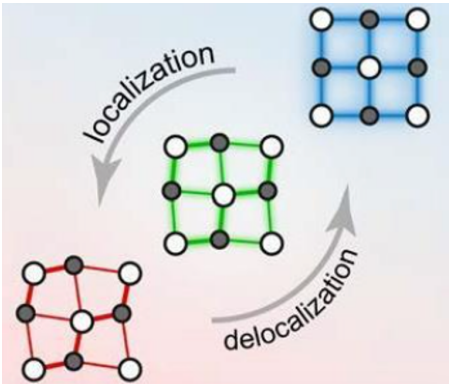

Figure 25: Tunable transition of MVB to its two extreme, metallic and covalent bonding, though electron localization and delocalization. [80]

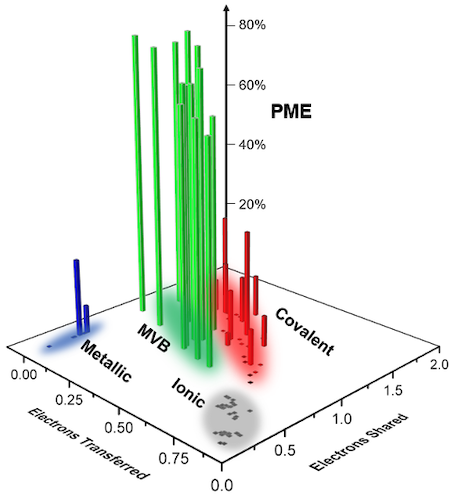

Figure 26: PME value on the basal plane as a function of electrons transferred (ET) and shared (ES), representing quantum chemically calculated chemical bonding. [75, 90].

2.2.5 *Multiple events in atom probe tomography*

2.2.5.1 *Basics of atom probe tomography*

The atom probe tomography (APT) technique operates based on the principle of field evaporation. Under an extremely high electric field, typically in the range of 10 V/nm, the surface atoms are positively ionized. [91] The bonds between adjacent atoms can be broken under the high field in conjunction with a short laser pulse, which is used to control the evaporation process to achieve a low detection rate. The ions generated by the broken chemical bond fly to the detector. Interestingly, the bond breaking results by APT can classified into two type: one ion generated by one laser pulse and several ions generated by one laser pulse. Applying APT technique, for InSb as a sp^3 covalent bond material, most experiments observe a single ion after a laser pulse, only in very rare cases, two ions are generated. The same result is also observed in GeSe, a sp^3 covalent bond material. On the contrary, for MVB compounds, the bond breaking result in majority experiments changes to several ions generated by one laser pulse. A successful laser pulse should dislodge only one single fragment (ion), called a single event, while the process that generates more than two ions within one laser pulse is referred to as a "multiple event". In order to quantify the bond breaking process, the probability of multiple events (PME) is defined as the ratio of multiple events to total events. Based on the measurement result of 80 materials, it has been found that all compounds employing MVB exhibit an abnormally high value of PME, which range from 60% to lager than 80%. Whereas, the PME values do not exceed 30% in covalent, ionic and metallic bonded materials. [10, 87] Therefore, the high PME value is utilized as an indicator of metavalent bonding. The PME value is also a quantity to characterize the bond breaking process in atom probe tomography.

However, the causality between chemical bonding and PME value is still unclear. The reason comes from some unclear questions in APT technique, such as the very complex evaporation process involving high electrical fields, surface states, band bending, and the interaction between specimen and laser. Another possible reason is chemical bond properties. For metavalent bonding, it is a soft bond. So it could be more unstable under high fields and laser excitations and, thus, several bonds break under one laser pulse generating multiple events.

We have also built a correlation between the high PME value and the unique material properties of MVB-based materials. Figure 26 shows the PME value on the basal plane as a function of ET and ES, representing quantum chemically calculated chemical bonding. The PME value is high in the region of low ET (ranged from 0 to 0.6) and moderate ES (around 1), which corresponds to the region of MVB (green region). These different regions with different bonding type possess unique material properties including the electrical conductivity σ, the Born effective charge Z^* as a measure of the chemical bond polarizability, the effective coordination number, the optical dielectric constant ε_{st} as a measure of the electronic polarizability as well as the Grüneisen parameter as a measure of the bond anharmonicity. Hence, there is clearly a correlation between metavalent bonding and bond breaking in the atom probe.

The electron delocalization and localization is a sign of bond transition from metal to covalent bond. Thus, we try to use the electron delocalization and localization to denote bond transition in atom probe tomography. Figure 27 is the result of PME value plotted against the room temperature conductivity as $\log(\sigma)$. The figure shows that only metavalently bonded compounds with electrical conductivities around 10^3 to 10^4 S/cm show high PME values. Doped semiconductors like P-doped Si, which have similar conductivities as well as low-conductive solids and good metals on the contrary do not show high PME values. There is clearly a remarkable correlation between the electrical conductivity and the bond rupture.

We have found some possible correlations between the high PME and the large penetration depth of the electric field, which depends on the optical dielectric constant and effective masses of materials according to the Debye screening length for semiconductors. Interestingly, MVB compounds are characterized by large optical dielectric constants and small effective masses, leading to a large penetration depth of the electric field.

2.2.5.2 *Determination of the probability of multiple events*

Atom probe tomography is a type of microscopy in which just the specimen itself is used to generate a picture. Figure 28 displays the typical setup of the atom probe. With a radius of less than 100 nm, the specimen emits ions that travel 80 - 200 mm to a detector with a diameter of 35 - 80 mm.

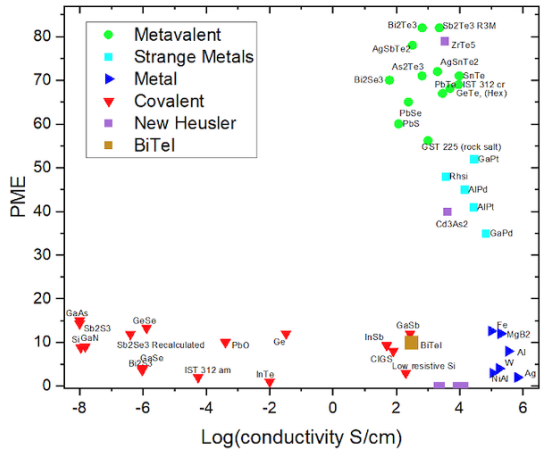

Figure 27: Probability of Multiple Events (PME) determined by atom probe tomography plotted against the room temperature conductivity as $\log(\sigma)$. [92]

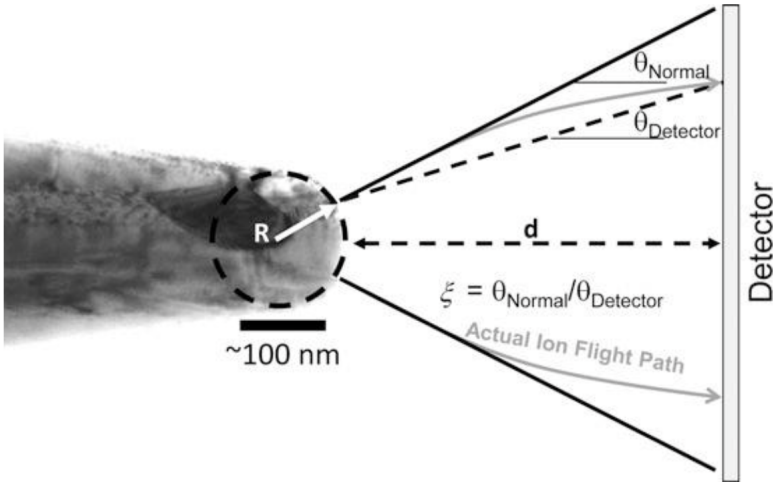

Figure 28: Geometrical relation between tip radius (R) and image compression factor (ξ), influencing tip image angular magnification. [93]

The creation of 3D atomic-by-atomic images follows a two-stage process, assuming a projection model. Firstly, each ion detected at coordinates (X_D, Y_D) is demagnified using a reverse-projection model to determine its original position within the specimen, based on impact coordinates (X, Y). In this case, X and Y are given by

$$X = \frac{x_D}{M} \tag{50}$$

$$Y = \frac{y_D}{M} \tag{51}$$

Here, M represents the magnification factor, given by

$$M = \frac{L}{(\xi R)} \tag{52}$$

where R is the radius of curvature of the emitter apex, L is the tip-to-detector distance, V is the total applied voltage, E is the evaporation field of the alloy, and β is a parameter ranging from 2 to 8.

In the second stage, the depth coordinate is determined. The sequence of evaporating ions provides information about the z-depth. Assuming ions emanate from an emitting surface with a peak at depth z_{tip}^{i} for the ith observed ion, the emitting surface is incrementally displaced by dz as ions are atomically eliminated during reconstruction. This displacement is given by

$$z_{tip}^{(i+1)} = z_{tip}^{(i)} + dz \tag{53}$$

$$d_z = \frac{\Omega}{\eta s_A} + R(1 - \sqrt{1 - \frac{x^2 + y^2}{R^2}}) \tag{54}$$

The CAMECA Integrated Visualization and Analysis Software (IVAS) was used in this study for the analysis and reconstruction of LEAP data.

3

METHOD

3.1 SAMPLE SUBSTRATE PREPARATION

3.1.1 *Electrode design layout*

In this thesis project, we have investigated various nanostructures, including individual grain boundaries in Ag-doped PbTe, twin boundaries in $Bi_2Te_{2.7}Se_{0.3}$, and precipitates in doped Te. We developed a focused ion beam (FIB) assisted device fabrication method to study individual nanostructures. The design aimed to separate resistance measurements between the grain boundary and neighboring grain regions.

The initial design consisted of eight electrodes with square contact pads in a hall-bar geometry (Figure 29(a)). The contact pads were used for wire bonding to connect the sample with the electrical measurement system. The two horizontal ends were used for the current source, while the six remaining electrodes were used to measure the horizontal voltage drop in the resistivity measurement upon cooldown and the vertical voltage drop in the Hall measurement. The upper image in Figure 30 indicated that the grain boundary was placed vertically between the four left voltage ends. However, the increase in the number of electrodes led to a high failure rate in device fabrication. It required excellent FIB operation skills to transfer the grain boundary to a narrow distance of only 3 µm between the four vertical electrodes.

After analyzing the failures, we changed the electrode design to a six-electrode hall-bar geometry that was suitable for the grain size of about 2 µm in the polycrystalline bulk material used in the project (Figure29(b)). The length and width of the transferred sample region were adjusted to accommodate different grain sizes in different materials.

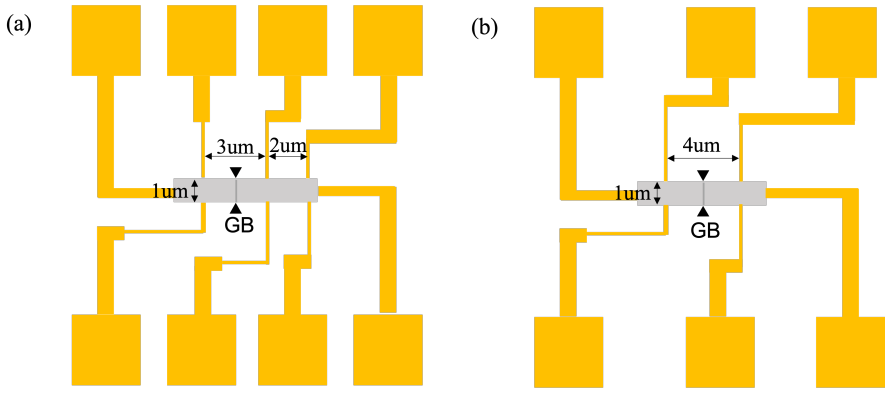

Figure 29: Two type electrode design:(A)eight electrodes (B)six electrodes

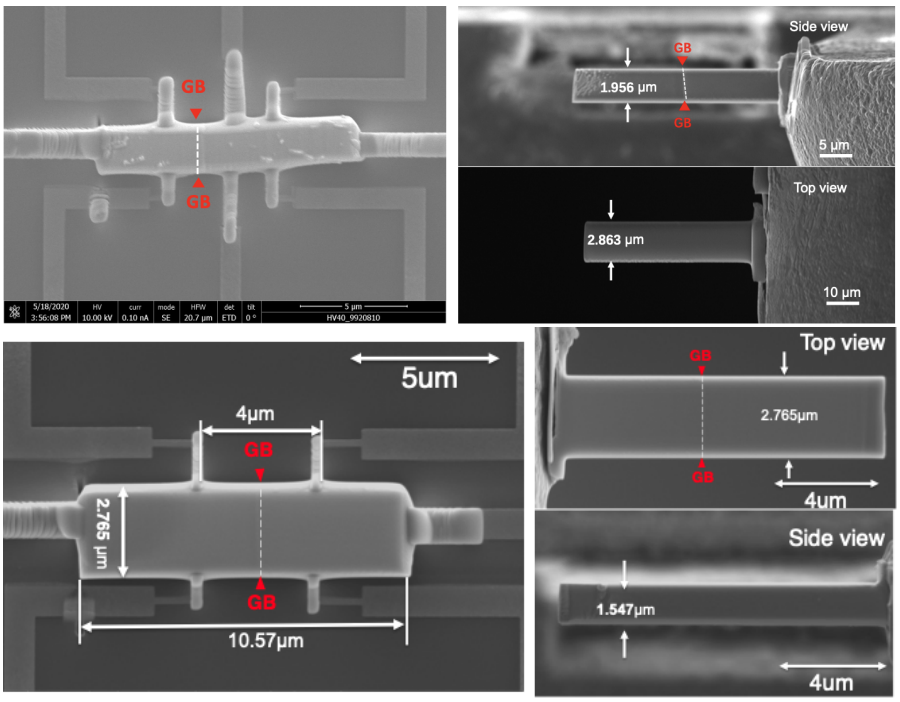

Figure 30: SEM image depicting a vertical grain boundary located between the four left voltage ends. Upper image: transferred devices onto eight electrodes, and lower images: transferred devices onto six electrodes in hall bar geometry.

The design layout was created using both the Keylayout software and the electron beam lithography software provided by Raith. The design layout was saved as a GDS file, which was readable for the lithography machine. The GDS file contained a design of hall-bar-like geometry electrodes for a thermoelectric grain boundary study device, which is attached in appendix A. The design layout included six layers, with Layer 1 and Layer 2 not requiring writing. Layer 1 was the working field with a size of 1000×1000 µm. Layer 2 was the target location where the lamella sample will be transferred following the FIB process. The electron beam lithography (EBL) writing layers were Layer 3, 5, 6, and 7, which correspond to contact pads with sizes of 150×300 µm, 1 µm broad lines, 200 nm broad lines, and 5 µm broad lines, respectively.

3.1.2 *Electron beam lithography*

The lithography process creates structures on a wafer by utilizing light energy. Light can be the exposure source, transferring the designed structure through a patterned mask onto the wafer. In contrast, electron beam lithography (EBL) replaces the light source with an electron beam as the exposure source. The EBL system, depicted in Figure 31, comprises of an electron source that emits the beam, an anode that accelerates it, and coils that focus and deflect it. Ultimately, a focused e-beam, with a diameter of approximately 5 nm, can be generated and used to expose patterns based on the GDS design file. The pattern can be designed in the GDS file, which makes

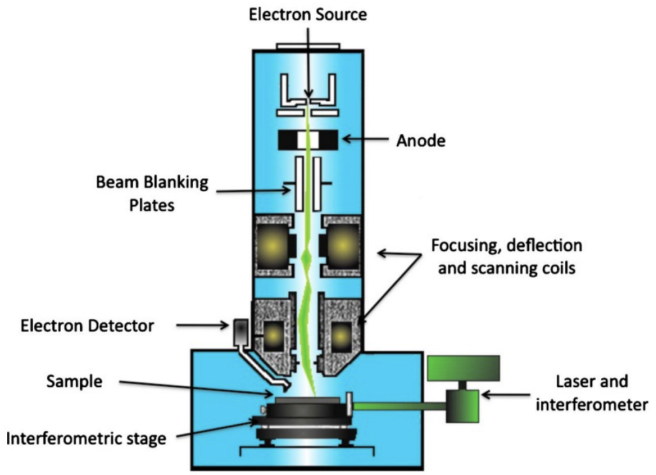

Figure 31: EBL set up system

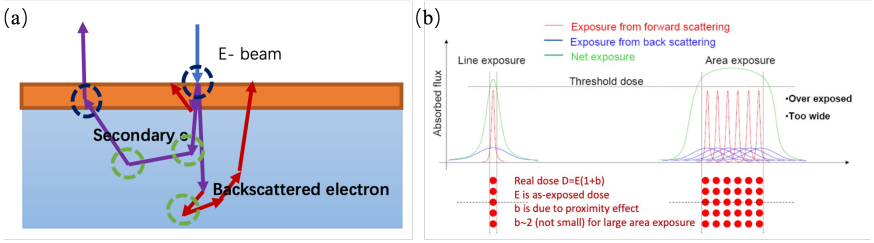

Figure 32: (a)Electron interaction (b)proximity effect

the EBL highly customizable and eliminates the need for the Chrome (Cr) Photomask. Beam blanking plates prevent exposure in unwanted regions during the whole writing process. The patterning process is split into several writing fields. When the exposure in one writing field is complete, the substrate moves to the next writing field by the motor equipped on the sample stage along the x- or y-axis. [94]

EBL employs polymethyl methacrylate (PMMA) as an e-beam photoresist, differentiating it from UV-lithography processes. When initial electrons collide with the surface, they scatter with the resist layer and substrate, generating secondary and back-scattered electrons. (Figure 32(a)) These electrons undergo multiple scatterings, returning to expose the e-beam resist layer. This leads to a high total electron dose and inaccuracies in the exposed pattern's size and shape, known as the proximity effect. As illustrated by the proximity effect in Figure 32(b), the exposed regions or line sizes can become wider than planned, and the total electron dose can also be higher than expected. Therefore, a dosage test is necessary before exposing the sample. The proximity effect depends on the density and atomic mass of the substrate material, and the energy of the electron beam. In addition, since large and small patterns that are placed close together can cause fluctuations in the total electron dose, this factor must be considered when designing the pattern. While EBL offers numerous advantages, including high resolution and no lithography mask, it is unsuitable for mass production because of its long writing time and high cost.

EBL becomes the preferred technique for producing feature sizes of around 20 nm. In this thesis project, electrode lines with a width as small as 100 nm near the position of the transferred sample were successfully created using EBL, demonstrating the technique's exceptional resolution capability, as shown in Figure 33. The EBL machines utilized for this project were the Raith machine located in the Physics clean room and the machine in Julich. Due to equipment issues, different batches of substrates were processed in different clean rooms. In the physics department clean room, the writing process was sometimes halted due to software issues, which could usually be resolved by restarting the software or seeking technical assistance. For this reason, it is recommended that EBL be performed in Julich. The experiment's accelerated voltage and expose dose were 30 kV and 700 $\mu C/cm^2$, respectively.

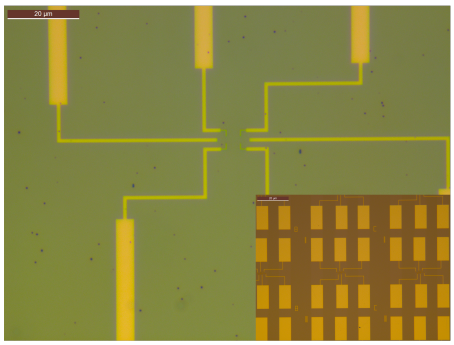

Figure 33: Microscopy image of electrodes: demonstration of EBL's resolution capability with electrode lines as small as 100 nm.

3.1.3 *E-beam evaporation*

The process of depositing metal coatings onto a semiconductor surface is called evaporation or metallization. This process uses an evaporator within a vacuum chamber, as depicted in the schematic diagram shown in Figure 34. Heaters or an electron beam are employed to melt the metals in the crucible. [95] The evaporator is classified as a thermal or e-beam evaporator, depending on the specific melting pro-

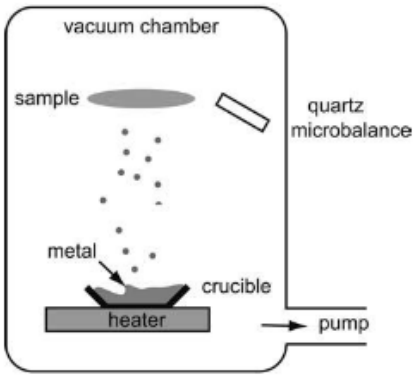

Figure 34: Schematic diagram of the evaporator

cess utilized. The sample is inserted into the evaporator in a reverse orientation. Once the temperature within the evaporator reaches a sufficient level, the metal evaporates onto the sample's surface at approximately one nanometer per second. The resulting film's thickness is measured using a quartz microbalance that oscillates. It is essential to ensure that the thickness of the deposited metal does not exceed 1/3 of the resist thickness when considering subsequent lifting process. The typical thickness of the deposited metal ranges from 20 nm to a few micrometers.

3.1.4 *Electrode fabrication flow*

In this experiment, n-type silicon (Si) wafers with a 400 nm silicon oxide (SiO_2) layer on top were used as substrates. To keep the samples flat when mounted on the sample stage in the focused ion beam (FIB) dual beam system, the wafers were diced into 1×1 cm² squares.

3.1.4.1 *Photoresist coating process*

The polymethyl methacrylate (PMMA), AZ639.04 and 679.02, with molecular masses of 50K and 150K respectively, were employed in this thesis. A double-layer approach, involving PMMA with differing molecular masses, was adopted to enhance lift-off process efficiency, as well as to achieve better resolution and aspect ratio. The lower layer's higher sensitivity to light, as compared to the upper layer, allows for more precise exposure and development.

The PMMA was coated onto the substrate using a spin coater. The substrate was first cleaned by rinsing it in acetone and isopropanol for 2 minutes each using ultrasonic cleaning. The clean substrate was then placed onto the vacuum stage in the spin coater, and the PMMA was dropped onto the surface and evenly spread to cover the entire substrate surface. The coating recipe was divided into two different acceleration velocities, as shown in the table in Appendix B.

3.1.4.2 *Exposure process*

In the test process, the exposed dose was 300-900 $\mu C/cm^2$ for the same structure. The exposure dose interval was $50\mu C/cm^2$. After development and metallization, the electrodes were formed. Under microscopic observation, it was found out that the structure with dose parameter 700 $\mu C/cm^2$ was the best exposed. So, the final exposed parameter was 700 $\mu C/cm^2$.

After the exposure, the substrate was developed in the developer 600-55 for 75 s and immersed into isopropanol for 30 s to stop the development. At the end, the developed substrate was blown by nitrogen and checked under a microscope as shown in Figure 33. To find an appropriate developing time, a test was done in 80 s and 95 s to confirm the right developing time.

3.1.4.3 *Metallization*

In order to get a high-quality film, the e-beam evaporator was adopted to deposit 2 nm Ti as an adhesion layer and subsequently a 10 nm Au layer.

For the lift-off process, the sample was immersed in acetone for 2 hour. Subsequently, the sample was immersed in the ultrasonic bath for 10 s to lift off the film. Finally, a microscope was used to check the resulting pattern on the substrate. The images after lift-off are shown in appendix C.

3.2 FOCUSED ION BEAM

As an imaging and nanofabrication tool, a FIB has been developed based on research into ion-solid interactions. When FIB is scanned across the sample surface, it operates similarly to the Scanning Electron Microscope (SEM). For the FIB system, the ion source generates the ion beam and focuses it on a nm-sized spot on the sample's surface to mill the sample. It is a versatile tool capable of imaging, milling, and deposition. Due to the significant mass difference between ions and electrons, and the ion's high energy, FIB can also precisely mill materials. Simultaneously, the focused ion beam is capable of deposition because it can precisely deliver the precursor gas to specific areas on a sample. For imaging, focused ion beams can provide high-resolution images with ~ nm resolution. Nevertheless, it will damage the sample surface. In conclusion, a FIB is the most efficient equipment for materials characterization and tomography observation on the nanometer scale and an indispensable tool for studying material properties.

FIB technology has been widely used in material science, engineering, biology, and medicine. This method can observe and characterize materials and the tomography on the surface of materials. Recently, focused ion beams have become commercially available and are widely used in the semiconductor industry for quality control. Despite their unique capabilities for micro-sample preparation, FIBs are employed relatively infrequently in physics research. The primary goal of this PhD project is to fabricate devices with individual nanostructures using FIBs and to pre-characterize these nanostructures with the material characterization function in a dual beam FIB/SEM system.

3.2.1 *FIB/SEM system basic principle*

The FIB/SEM system utilized in these experiments was a Dual-Beam Helios NanoLab 650, which integrates the FIB and the electron beam in the same instrument. The ion beam column is angled at 52° relative to the electron beam column when at the home position of the stage. This feature enables simultaneous imaging and milling, simplifies navigation, and overcomes geometric limitations during three-dimensional (3D) imaging, analysis and sample preparation. For in-

stance, when cutting a slab at the region of interest in the bulk sample as shown in Figure 35, the SEM column offers non-invasive, high-resolution imaging, and the FIB column mills the sample simultaneously.

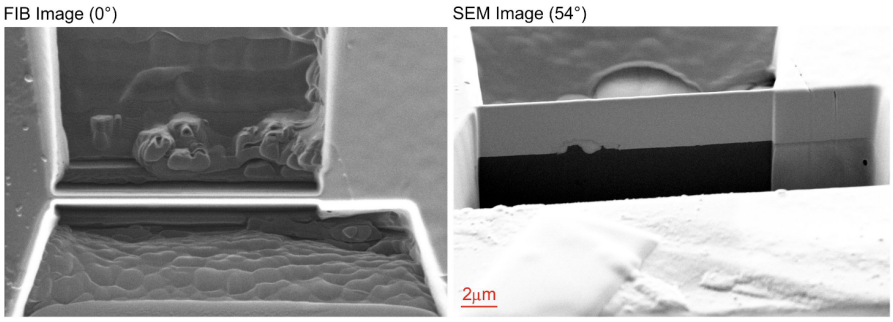

Figure 35: FIB image at normal incidence (0°) (left) and SEM image at 54° (right) of the same micro-structured sample. [96]

Gallium (Ga) is often chosen as the source material due to its low melting temperature, which is close to room temperature. However, caution must be taken to avoid Ga doping in materials. In our laboratory, we have observed that the gallium ions penetrate to a depth of approximately 10 nm below the surface of the material in atomic probe tomography analysis. The level of Ga contamination in FIB-prepared specimens is influenced by the acceleration voltage and current. Research has shown that at 30 kV, Ga can penetrate Si up to a depth of approximately 40 nm. [97] In this study, we employed a very low voltage (2 kV) and current (4 pA) to clean the specimen surface during the final step. As a result, the Ga contamination is expected to be minimal. Furthermore, no Ga signals were observed in the atom probe tomography specimen, providing additional evidence that the Ga contamination has minimal influence on the measurement result.

Figure 36 shows the FIB-SEM system that was utilized in this study. The FIB column consists of an ion source, accelerator stage, and electronic lenses for beam focusing and shifting. Besides the FIB and SEM columns, the system on the left side of Figure 36 is equipped with a gas injection system (GIS) to deposit metals or insulators. The sample is mounted onto the sample stage, which is controlled by a precision mechanical stepper motor in the NVision. The NVision is a sophisticated platform software to control the FIB system. This provides sub-micrometer precision for moving, rotating, and tilting the sample stage, allowing for the preparation of specimens used for electrical measurements. The omniprobe is used for the extraction process.

The dual beam system becomes powerful with various detectors for non-destructive material characterization. These characterizations include Electron Backscatter Diffraction (EBSD) and Energy Dispersive X-ray Spectroscopy (EDX or EDS), which have been applied in this thesis project to characterize nanostructures. EBSD is a technique utilized for investigating the phase and crystal orientation of a crystalline lattice. To perform EBSD analysis, the specimen is required to be polished in order to minimize topography effects. This is because

the backscattered electron has an energy up to the incident beam energy and is usually very near that energy.

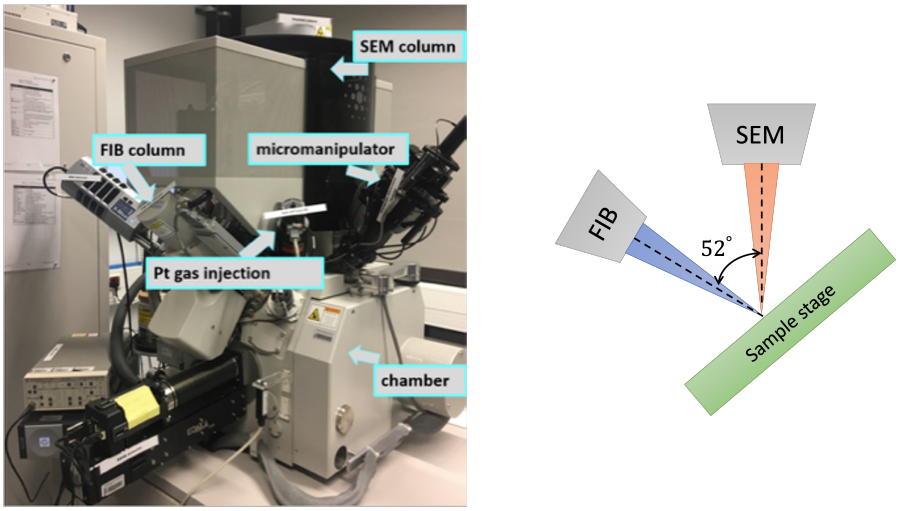

Figure 36: Left: Dual-Beam Helios NanoLab 650 in the RWTH institute of physics, 1A. Right: Sketch illustrating the 52° angle between the SEM and FIB columns.

The incident electron beam interacts with atoms, generating backscattered electrons with high energy (> 50 eV). In the EBSD analysis (Figure 37(a)), these backscattered electrons interact with the crystalline lattice and produce the diffraction pattern. The resulting Kikuchi pattern, shown in Figure 37(b), represents the lattice structure of an iron crystal in the [110] direction (Figure 37(c)). Specialized software processes this EBSD data to produce crystallographic information, including the orientation of each grain, as indicated in Figure 37(d). The software also enables the calculation of the misorientation angle between the crystallographic orientations of adjacent grains. This is achieved through mathematical algorithms that compare orientation matrices or the orientations themselves, quantifying the angular difference between neighboring grains. This is applicable to determine the misorientation angle of individual grain boundaries in this thesis. However, the EBSD image can only recognize and classify phases but cannot indicate the presence of elements or their concentration levels.

The energy dispersive analysis assisted by X-ray spectroscopy(EDX) meets the need to determine the elemental composition or concentration on the sample surface. When the electron beam interacts with atoms in the sample, it excites inner-shell electrons. As these electrons are ejected, outer-shell electrons fall to lower energy states, releasing energy in the form of X-rays. The characteristic X-ray emission process are shown in Figure 38. The X-rays are detected using an energy-dispersive detector, which presents the signal as a spectrum or histogram. The spectrum displays various peaks on an x-y axis, representing the number of X-rays detected and their corresponding unique energies. By comparing peak intensities and using standardized reference materials, the EDX software calculates the composition ratio of each element. Even different isotopes of the same elements and their composition ratios can be measured by more advanced tech-

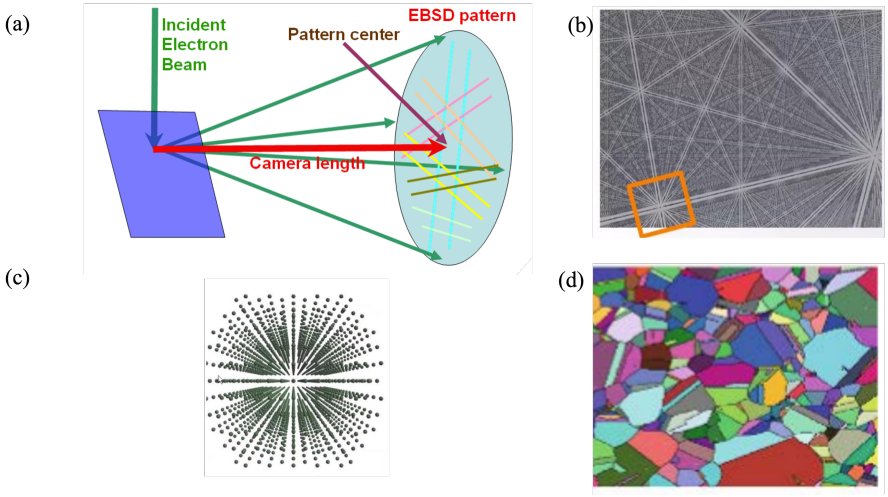

Figure 37: (a) Illustration of the working principle of Electron Backscatter Diffraction (EBSD). (b) Lattice structure of an iron crystal measured in the [110] direction. (c) The corresponding Kikuchi pattern. (d) EBSD map showing the data collected for an iron crystal.[98]

niques like Secondary Ion Mass Spectrometry (SIMS) or Inductively Coupled Plasma Mass Spectrometry (ICP-MS). In a SEM-FIB dual

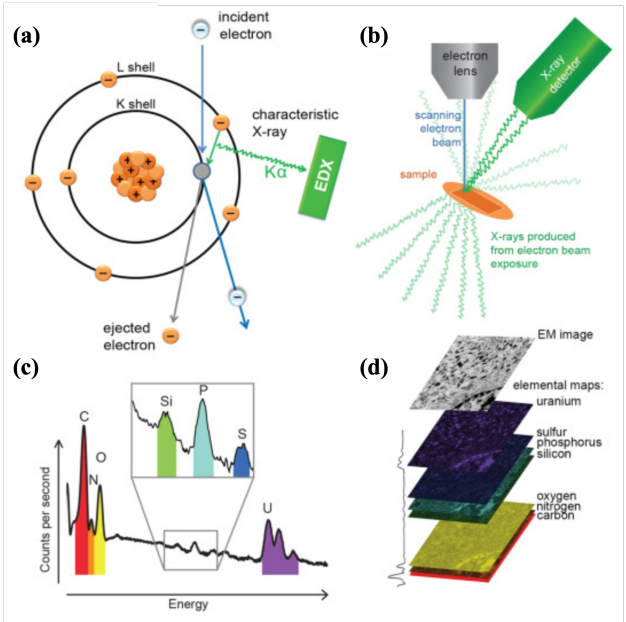

Figure 38: (a) characteristic X-ray emission (b) EDX measurement process (c) peak intensity spectrum corresponding to elements such as C, O, Si, and U, with higher peak intensities indicating greater elemental concentrations (d) elemental maps generated from the EDX data, highlighting distribution of elements like uranium, sulfur, phosphorus, silicon, oxygen, nitrogen, and carbon within the sample scanning area.[99]

beam system, the electron beam can be rastered over an area of the sample to produce X-ray element distribution maps, which show how the concentration of one or several elements varies over that area.

In this thesis, both characterization methods have been adopted. The EBSD is used to characterize the orientation of crystalline lattice and determines the misorientation angle between neighboring grains in the chapter 5 and chapter 6, while the EDS/EDX measurements are applied to determine the existence of precipitates in bulk doped Te by the variation of composition as illustrated in the chapter 7.

3.2.2 *Lamella extraction from Bulk Sample: the Milling Process*

In the FIB system, energetic Ga ions hit the surface of a solid sample, generating secondary ions and electrons used for imaging. Due to the ion beam's large mass and high energy, FIB imaging can damage the sample. Typically, a low current is used for imaging, while a high current is used for material removal, known as milling.

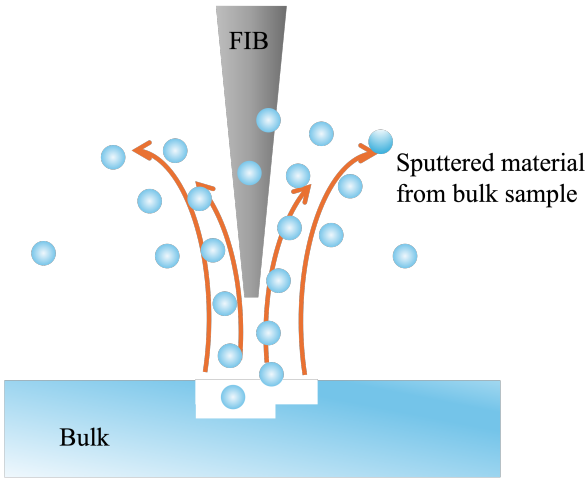

Figure 39: Schematic representation of milling process using focused ion beam

When a highly energetic ion beam is applied, the material is sputtered away, as shown in Figure 39. This allows for selective sputtering with nanometer-scale precision. The high kinetic energy and very large mass of Ga ions allow them to transfer substantial energy and momentum to the atoms in the sample, overcoming the binding energy and causing sputtering. A Ga ion, 130000 times heavier than an electron, effectively knocks atoms out of the material. [100] In this thesis, Ag-doped PbTe, Bi_2Te_3, and various doped Te samples have been successfully cut using the ion beam.

The milling process using FIB removes materials atom by atom, even during imaging. SEM is used to observe this process. When the material is milled, it does not fully evaporate. Instead, sputtered atoms form a redeposition layer. This layer limits trench milling, especially micro-structure sculpting. Therefore, the cut area should typically have an aspect ratio below 2 : 3. In this study, three rectangles were drawn with a large geometry ratio in the region of interest to avoid redeposition when applying the ion beam for lamella extraction.

3.2.3 *Electrical contacts: ion-assisted metal deposition*

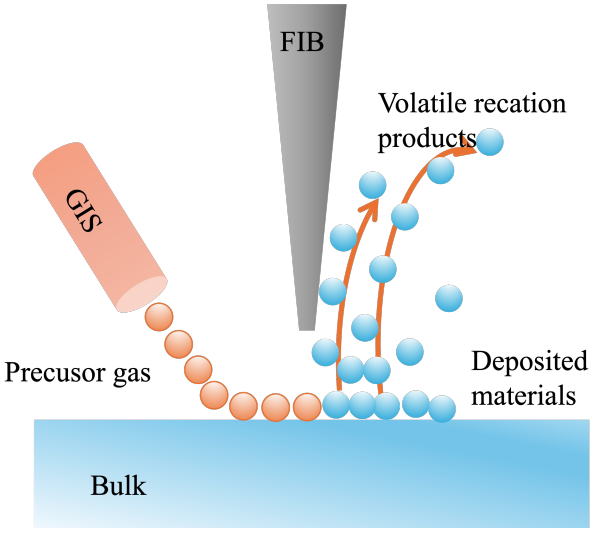

Figure 40: Working principle of FIB-assisted deposition.

The FIB system is equipped with a GIS that allows for the deposition of metals and insulators. The GIS is a nozzle that can be positioned close to the sample surface, which is shown in Figure 36(left). After defining the desired pattern, the nozzle releases a precursor gas locally into the chamber at low pressure (around 10^{-5}mbar). The basic principle is ion-assisted chemical vapor deposition in Figure 40, and in this case, the gas molecules from the nozzle reach the sample surface, where some of them are absorbed. The absorbed gas molecules in the defined pattern region are then subjected to a focused ion beam, leading to dissociation and decomposition. Finally, this process results in the deposition of materials and the removal of organic ligands.

The choice of precursor gases depends on the desired deposition, with metal organic gases used for metal deposition and tetraethyl orthosilicate for SiO_2 insulator deposition. In our FIB system, the available metals for deposition are platinum(Pt) and tungsten. However, it's important to note that the deposited Pt is not a pure metal, but rather a complex compound consisting of approximately 46%Pt, 24%C, 28%Ga, and 2%O. Therefore, confirming the ohmic contact is crucial to maintaining the accuracy of measurements when characterizing the materials' physical properties.

To achieve ohmic contact, the FIB-deposited Pt film should be carefully adjusted to be low-resistance. The resistance of the Pt film is determined by the ion beam's current and dwelling time. A series of experiments were performed to determine the optimal current and dwelling time in this project to find a suitable parameter. Finally, the optimal current dose per irradiated area was identified as 7.7 $pA/\mu m^2$. The dwelling time is remarkably essential for electrical contacts. The dwelling time for the current ends is set to 2 min, while the setting time for the voltage end is controlled in ~ 30 s. The resulting

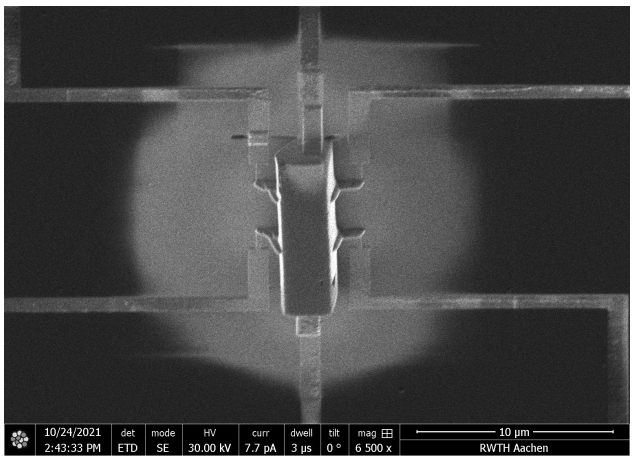

Figure 41: SEM image shows a sponge-like Pt layer on transferred lamella, confirming an excellent conduction.

Pt film should form a sponge-like structure, shown in Figure 41, in order to obtain a better contact.

Furthermore, it has been reported that the FIB-deposited films may be improved by heating the film for only 10 min to 300°C in an oxygen atmosphere or heating to 300°C on a hotplate for 10 min. [101] The current parameter in this experiment already produced a good conducting Pt film, even without curing.

3.2.4 *Lamella sample preparation*

The polished bulk is fixed to a sample stage using a silver paste to enhance the removal of charge buildup in FIB operation. Before this fabrication process, the region of interest (ROI) is pre-characterized using FIB, EBSD, and EDX techniques to obtain information such as crystalline grain direction, tilt angle in a polycrystalline sample and composition of precipitates in the doped sample. To ensure the position of the ROI is not lost during tilting of the sample stage or column changes, a Pt cross marker is often used to mark the position. Specific observation parameters are established to achieve a good FIB image of a grain boundary with an accelerated voltage of 30 kV and a current of 0.24 nA. In addition, irradiating the bulk sample surface with an ion beam assists in obtaining a clear outline of the grain boundaries. To mitigate the influence of grain boundary orientation on carrier transport, the focus was only on vertical grain boundaries as the target.

3.2.4.1 *Lamella Extraction*

The lamella extraction process is similar to the sample preparation in transmission electron microscopy (TEM). Initially, the selected grain boundary was positioned vertically in the SEM and FIB windows. Subsequently, the stage was tilted precisely to an angle of 52°, perpendicular to the FIB column. In Figure 42(a), three trenches are cut around the region of interest (ROI). In grain boundary studies, the GB

position should be centralized in the lamella, whereas in precipitate studies, the cut lamella should contain a pre-characterized specific precipitate. The sample stage needs to be tilted back to 0° to cut the underside of the lamella, as depicted in Figure 42(b). The removal of the lamella from the bulk is crucial, and should only proceed once a cut line appears at the bottom, indicating that the lamella has been completely removed. Another tip to check the FIB current, which causes a vibration once the lamella is free. Otherwise, the lamella may break easily during the final extraction step using the omiprobe, as shown in Figure 42(e).

The prepared specimen is typically $1.5 \times 2 \times 10$ µm in size, and the process requires coarse FIB with a high ion current of 0.79 nA and 30 kV acceleration voltage to cut the trench, and a lower ion current of 0.24 nA to remove the other sides of the lamella.

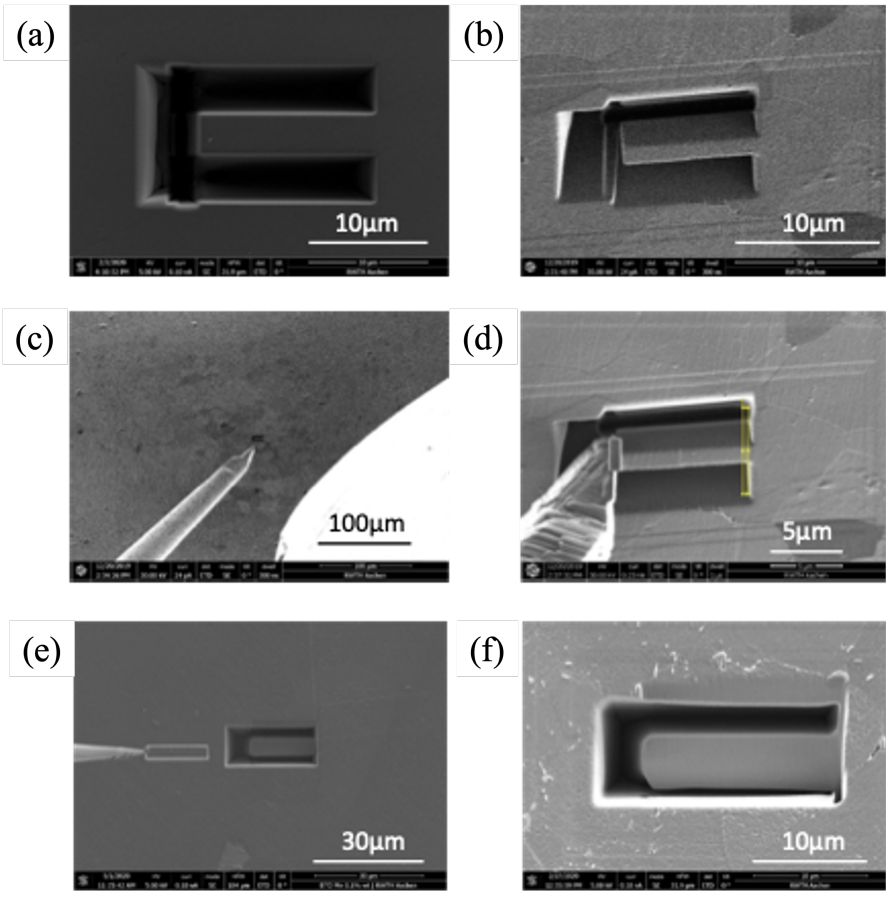

Figure 42: Sequential steps in the extraction process of a lamella with pre-characterized nanostructure from the bulk sample: (a) Formation of three trenches. (b) Removal of the bottom side of the lamella. (c) Approach of the micro-manipulator towards the cut lamella. (d) Fixation of the cut lamella using Pt deposition by the micro-manipulator. (e) Complete removal of the cut lamella from the bulk after cutting the left side. (f) The left trench after removing the lamella from the bulk.

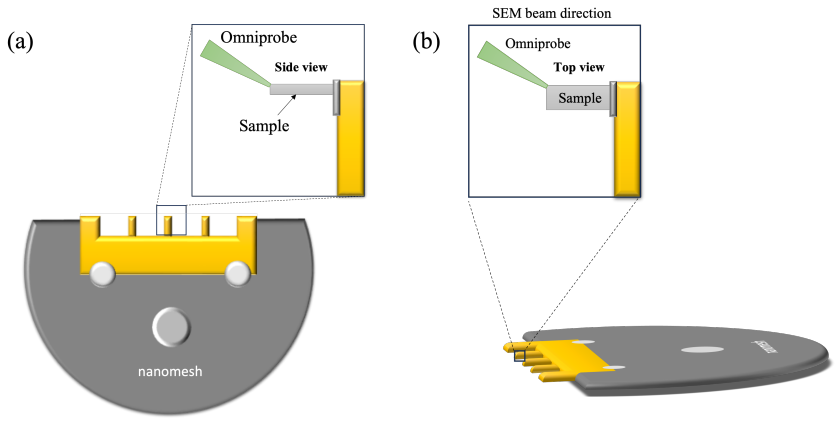

Figure 43: Manual rotation of the copper grid: (a) The cut lamella on the copper grid and the zoomed inset in side view (b) The cut lamella on the copper grid after a manual 90° rotation to define the width of the lamella, viewed along the SEM beam direction; the zoomed inset in the top view.

3.2.4.2 *Lamella reshaping*

In this sample preparation step, the extracted lamella is fixed onto a copper grid using an omniprobe. Its thickness is defined, then its length and width are reshaped by rotating the copper grid. The lamella thickness is critical for improving the accuracy of the electrical measurements, but it cannot be reduced below 1µm due to limitations in the following process. After defining the lamella thickness to around 1µm, the copper grid is manually turned 90° with a tweezer to change the lamella's direction. The rotation process is shown in Figure 43. The lamella, now reoriented, is further reshaped to a length of approximately 10 µm and a width of around 2 µm to match the electrode design, as illustrated in Figure 44. The milling process is performed in three steps: coarse, medium, and fine milling. The closer the ion beam comes to the lamella, the smaller the currents used for milling. Typical current settings for the preparation stages are 0.77 nA in coarse, 0.24 nA in medium, and a cross-section mode with 2 kV accelerator voltage and 4 pA current is applied for fine polishing. The final milling step in cross-section mode is to remove the Ga doping effect.

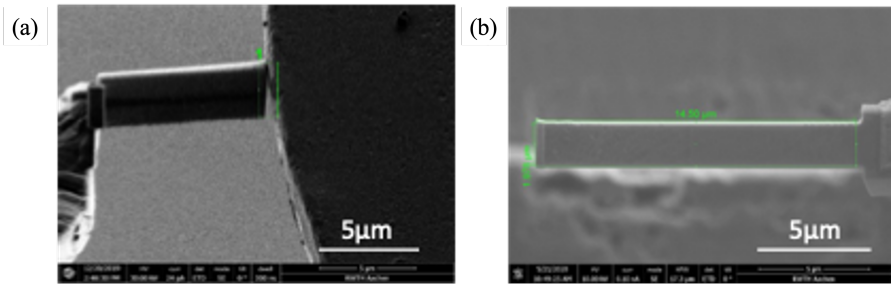

Figure 44: Lamella reshaping process: (a) the cut Lamella affixed onto the copper grid. (b) definition of the thickness of the lamella by milling.

3.2.4.3 *Lamella transfer onto electrodes*

The final stage of the lamella fabrication process involves transferring the lamella onto a substrate that has patterned gold electrodes. The substrate is composed of 400 nm or 1000 nm SiO_2 on p-type Si, which causes a local charge buildup and distorts the resulting image. Various approaches were attempted to address this problem, including silver paste, carbon epoxy, and copper tapes. A specialized sample stage with a metal clipper was used to secure the substrate and facilitate charge conduction through the clipper and copper tapes. This process requires prompt operation under the FIB column to prevent excessive brightness during imaging. If the image becomes too bright, the ion beam must be deactivated to allow electrons to pass through. To avoid damaging the substrate, ion beam exposure should be kept to a minimum.

The omniprobe removes the lamella from the copper grid and lowers it towards the substrate. The electron beam focuses on both the lamella and the pre-patterned gold electrodes. To avoid vibration, the Pt needle is inserted while the omniprobe is still at a distance. Once the omniprobe is sufficiently lowered, the lamella is fixed to one current end and detached from the omniprobe. The remaining electrodes are fixed by rotating the stage 90° four times, taking out the Pt needle each time. Attaching each voltage electrodes takes 30 seconds, while the larger electrodes take about 2 minutes. The details and parameters of the Pt deposition process at the electrodes are provided in the FIB metal deposition section. Figure 45 depicts the lamella transfer process and the final device is shown in Figure 45(c) and (d). The whole process to fabricate the device with specific nanostructures requires approximately 2 to 3 hours.

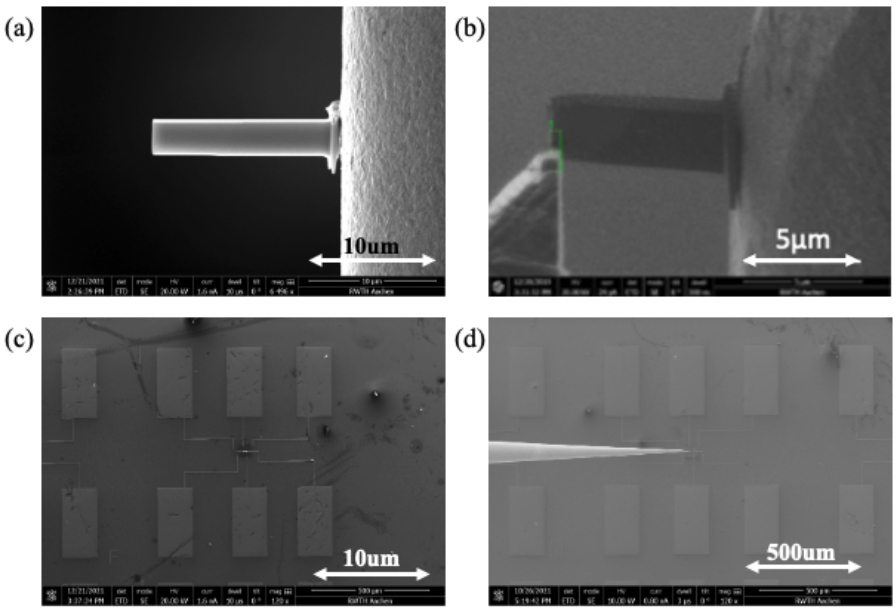

Figure 45: Lamella transfer process onto the nano-electrode substrate: (a) Lamella with specific nanostructure after accurate geometry definition. (b) Lamella being detached from the copper grid using a micro-manipulator. (c) The hall-geometry gold nano-electrodes. (d) The lamella is transferred using a micro-manipulator and affixed to the gold electrode by depositing Pt.

3.3 FABRICATION FLOW OF INDIVIDUAL GRAIN BOUNDARY SAMPLE

To address the challenging task of measuring local electrical properties of individual grain boundaries (GBs), we propose a novel method that combines EBSD, site-specific lift-out technique with a FIB, and nano-device fabrication. This approach allows for the extraction of a specific GB from millions of randomly distributed GBs in a bulk sample. A schematic of the fabrication process for a single GB device is shown in Figure 46.

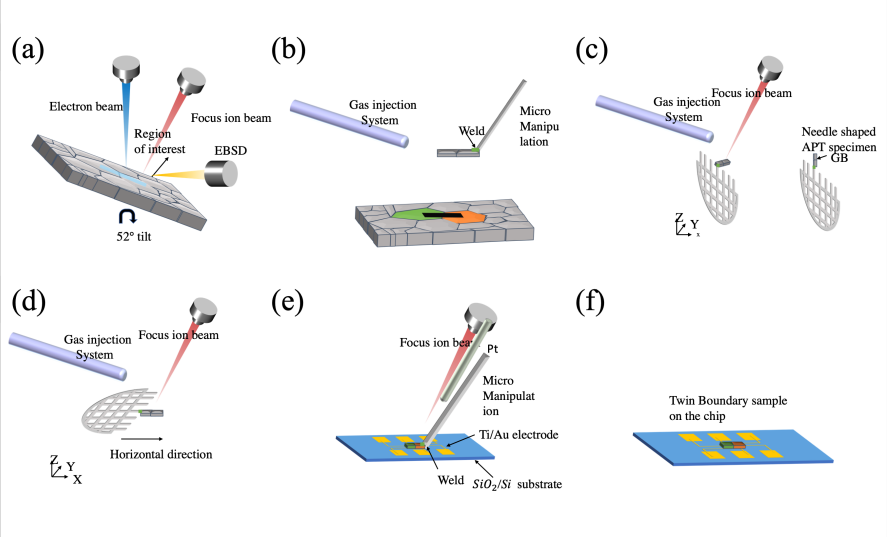

Figure 46: Schematic of the Fabrication process for a single grain boundary device: (a) Selection of target GB using EBSD, SEM, and FIB; (b) 'Lift-out' process for individual GB lamellae; (c) Transfer of individual GB lamellae and corresponding atom probe tomography(APT) specimen; (d) Manual rotation and reshaping of lamellae geometry; (e) Transfer of individual GB lamellae onto a microcircuit with electrodes; (f) Schematic of the final individual GB device.

In the first step, EBSD is used to identify the GB of interest with a specific misorientation angle (Figure 46(a)). Subsequently, a lift-out approach similar to preparing a transmission electron microscopy (TEM) lamella is performed (Figure 46(b)). The lamella, containing a GB with a certain misorientation angle or selected region of interest, is then attached to a copper grid and manually rotated by 90° to define the lamella geometry (Figure 46(c) and (d)). Finally, a micromanipulator is used to transfer the lamella to an electrode microcircuit and fix each end with Pt in the FIB (Figure 46(e)).

To correlate atom probe tomography (APT) and local electrical transport of the individual GB, the specimen is extracted for APT analysis from closely spaced positions at the selected GB region, and APT specimens are prepared using FIB. This approach allows for correlating APT with local electrical transport measurements of the GB. The APT specimen, taken from the same grain boundary region, is displayed on the right side of Figure 46(c). The Kikuchi diffraction

(TKD) is used on the APT specimen to ensure the misorientation angle of its grain boundary aligns with that of the single grain boundary device measured.

3.4 ELECTRICAL MEASUREMENTS

3.4.1 *Electrical transport measurement system (ETMS)*

The first step in connecting the fabricated device with measurement equipment is to use a wire bonding machine to connect the electrodes of the samples. This machine precisely controls wire placement and bonding, ensuring reliable and reproducible electrical connections.

Since high resistance is a common problem with FIB-deposited metal, it is essential to confirm that the contact resistance is acceptable and, that there is ohmic contact between the transferred sample and metal electrodes. Therefore, we use our electrical transport measurement system (ETMS) to check the contact. The linear I-V curve in Figure 47 shows a good ohmic contact between Ag-doped PbTe fixed by Pt and gold electrodes.

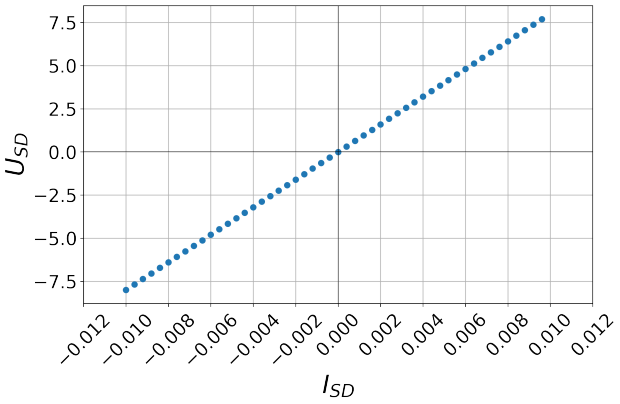

Figure 47: Linear I-V curve showing good ohmic contact between Ag-doped PbTe fixed by Pt and gold electrodes.

The ETMS here is designed and built by our group to meet our flexible measurement needs. The system consists of DC and AC sources, a multimeter, and two lock-in amplifiers, which can be controlled through a user interface designed and coded by our group. The system offers improved flexibility for various electrical measurements, including lock-in, AC, and magnetic field-related measurements. The control software was designed and coded in Python by previous group members, allowing for easy modification and automated design. I also modified it to meet my measurement requirements. The system can also be connected to a PPMS Dynacool for low-temperature and high-magnetic-field measurements via a specific breakout box. The instant plot function in the control Python application improves work efficiency and helps identify problems, contributing to the success of the sample fabrication.

3.4.2 *Physical properties measurement system (PPMS)*

The physical properties measurement system (PPMS) DynaCool is a powerful tool for investigating the physical properties of materials. Figure 48 shows the PPMS produced by Quantum Design company. This measurement equipment controls the chamber cooling down using a helium-based cooling system. The machine's working principle is a single two-stage pulse tube cryocooler that cools the superconducting magnet and the temperature control component. Liquid helium circulates through the system to absorb heat from the sample chamber, vaporizes, and is then recondensed for reuse. The temperature control precisely regulates helium flow using valves and feedback from temperature sensors to get stable low temperatures. The system can measure temperatures ranging from 1.8 K to 400 K and apply magnetic fields from -9 T to 9 T, allowing for precise measurements of the sample's electrical properties.

Due to the micrometer size of these measured devices, the bonded gold wires connect the metal pads on the chip and the sample holder, known as the puck. The puck is then connected to the sample chamber using a bottom connector to interface with the measurement system. The sample chamber is evacuated and maintained under a high vacuum using an inbuilt cryopump during measurements. All measurements in this study were conducted under 5 Torr to lower the chamber temperature to 2 K.

Figure 48: Physical properties measurement system (PPMS) DynaCool produced by Quantum Design

In this thesis, the temperature-dependent resistance and Hall measurements by PPMS were performed on devices with specific nanostructures. To measure the longitudinal resistance of a sample, the device is connected as shown in Figure 49. A constant current of 1 μA was applied to the two horizontal electrodes, which served as the current ends. The xx-direction longitudinal resistance was continuously recorded while temperatures were cooled down from 300 K to 2 K.

The resistivity of the device with a specific nanostructure can be calculated as:

$$\rho_{xx} = R_{xx} \cdot \frac{wt}{L} \tag{55}$$

in which t is the thickness, L is the length, w is the width of the device, and R_{xx} indicates the resistance in x direction.

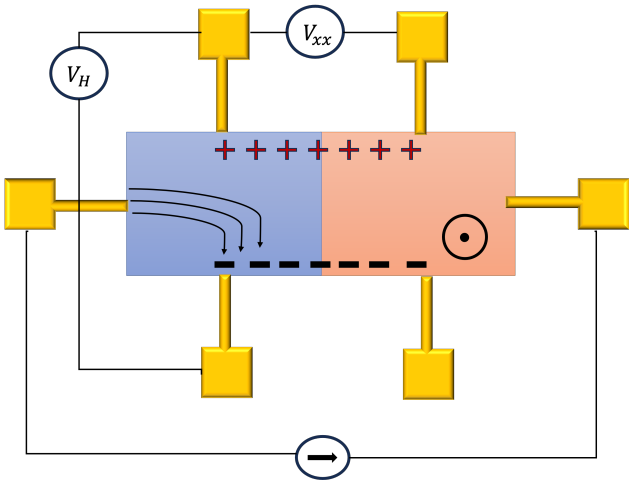

Figure 49: The sample connections under the longitudinal resistance cooldown and Hall measurement

The Hall resistance was measured at each temperature level, starting at 2 K and increasing in 25 K intervals until it reached room temperature. The system was kept stable at each temperature level to sweep the applied magnetic field from −1 T to 1 T. Under a magnetic field perpendicular to the applied current, the Lorentz force deflects the charge carriers, and a Hall voltage is generated. This voltage balances the electrical field in the opposite direction caused by accumulated charges. The Hall concentration n_H and mobility μ_H can be determined as follows:

$$\frac{U_H}{I} = R_{xy} = \frac{1}{n_H e t} B \tag{56}$$

In the formula 56, the resistance in xy direction R_{xy} is calculated by the hall voltage U_H dividing by the current I. The Hall concentration n_H can be determined by the measured R_{xy}, charge e, thickness t, and magnetic field B.

$$\mu_H = \frac{\sigma_{xx}(B = 0)}{e n_H} \tag{57}$$

in which the Hall mobility μ_H can be calculated by the longitudinal conductivity σ_{xx} at zero magnetic field, charge carrier concentration n_H, and charge e.

3.5 ATOM PROBE TOMOGRAPHY

Atom probe tomography (APT) is a microscopic analysis technique used to obtain a more detailed examination of a material's microstructure and chemical composition at the nanoscale. [102] It allows for

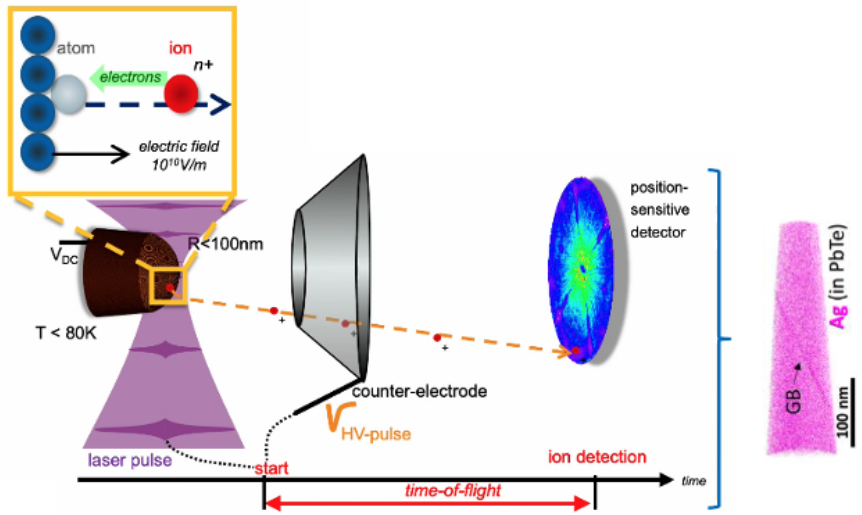

Figure 50: The working principle of APT.

high-resolution 3D imaging, complementing the information obtained from transmission electron microscopy.

Figure 50 describes the working principle of APT. It is based on generating a very high electric field at the apex of a sharp needle-shaped specimen. [103] When the field reaches a certain threshold, the surface atoms of the specimen are ionized. These ions are then accelerated by the field and fly along trajectories, which are determined by the distribution of the electrostatic potential in the chamber. The ions are collected onto a detector sensitive to the impact position, and the time of flight is measured using either high voltage pulses that temporarily increase the amplitude of the electrostatic field, or laser pulses that temporarily increase the temperature of the specimen apex. This gives a means of using time-of-flight mass spectrometry to identify each ion, and we can associate each ion with an elemental identity. This information is used to build a 3D point cloud, where each point is an ion detected and repositioned in three dimensions. [97, 104, 105]

In APT, mass spectrometry is the primary technique for identifying the composition of the analyzed specimen. It provides a mass spectrum that gives the quantity of atoms from each isotope present in the material. The mass spectrometry enables chemical identification according to the equation:

$$\frac{m}{q} = 2eV\frac{t_{TOF}^2}{L^2} \tag{58}$$

in which q represents the charge state of the ion (e.g., +1, +2, +3), m denotes the mass of the ion, e signifies the charge of an electron, V corresponds to the voltage applied to the specimen, L represents the flight path, which is typically 90 mm, and t_{TOF} denotes the time-of-flight, calculated as the difference between the arrival time of the ion at the detector (t_1) and the time at which the pulse was initially applied (t_0). For example, Figure 51 shows a piece of steel that contains vanadium and chromium, we can see the different isotopes of

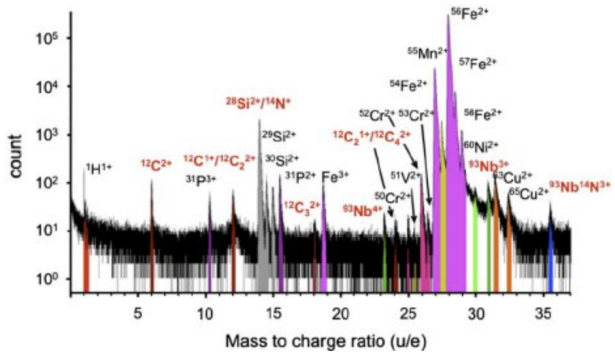

Figure 51: The mass spectroscopy in APT of steel. [106]

chromium, manganese, iron and the relative amplitude of each peak reflects the relative amount of specific atoms of a specific species within the sample that was analyzed. [106]

The second aspect of APT is its capability to locate atoms in three dimensions at a sub-nanometer scale, with part-per-million (ppm) sensitivity, in which segregation, precipitation, and multiple phases are easily identified. [107] For example, the nanocrystalline aluminum alloy has been analyzed in Figure 52. This 3D spatial volume of aluminum alloy reveals Ni and Y enrichment in the interface between pure Al nanograins. We can isolate an individual element to look at its distribution map (Figure 52(a)) and composition variation near the grain boundaries (Figure 52(b)). Sometimes, we actually can find traces of the crystallography of these different grains. So, we can image different sets of atomic planes within the reconstruction. [108]

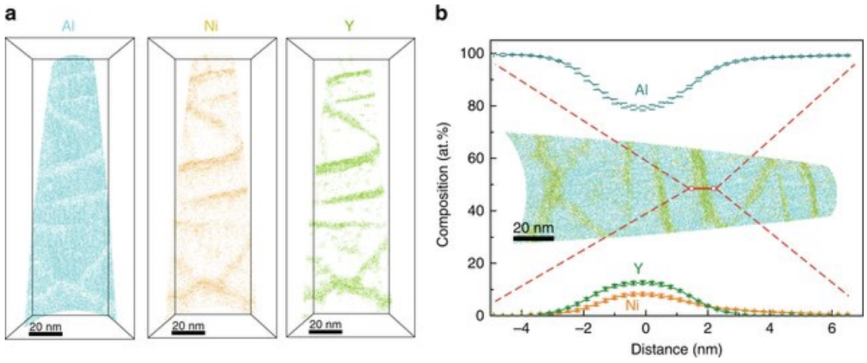

Figure 52: A 3D map in APT analysis of aluminum alloy: (a) atomic distribution maps of Al, Nb and Y (b) variation in the number of atoms detected at a GB in the 3D APT tip. [108]

In this thesis, experiments were carried out using a local electrode atom probe (LEAP 4000X Si, Cameca), employing ultraviolet laser pulses of 10 ps duration and 22 pJ energy. The average detection rate was one ion per 100 pulses, with a pulse repetition rate of 200 kHz, a specimen base temperature of 40 K, and an ion flight path of 160 mm. Due to the distance between the microchannels on the detector plates, the detection efficiency of the microscope is limited to 50%. IVAS 3.8, a commercial software package, was utilized to process the APT

data. We adopt a site-specific specimen preparation method. [97] This technique relies on field evaporation as its fundamental operating principle, which involves the ionization and desorption of surface atoms from the needle-shaped specimen.

4

INDIVIDUAL GRAIN BOUNDARY SCATTERING IN AG DOPED PBTE

4.1 INTRODUCTION

A good thermoelectric (TE) material should possess a significant Seebeck coefficient (S), high electrical conductivity (σ), and low thermal conductivity (κ). To enhance the figure of merit (ZT) value, effective strategies, such as nanostructure and defect engineering, have been developed. [109, 110, 21] Among these, doping is the most common strategy to obtain significant energy conversion efficiency. The inhomogeneous distribution of doped ions causes ion segregation, forming secondary phases, precipitates, and other microstructures. According to the reports on TE materials, Ag segregation at the GB area in Ag-doped PbTe will increase the electrical conductivity. [39, 111] In other circumstances, when the Ag concentration at the GB approaches 60%, a second phase Ag_2Te occurs in the Ag-doped PbTe. This second phase serves as a scattering center, limiting the flow of charge carriers. [112] These discrepancies in performance were ascribed to the critical role of GBs and their different microstructures by Ag doping upon carrier transport. Nevertheless, all these existing studies could not determine the true impact of individual nanostructures on the TE properties. This is because determining these TE properties locally at the nanostructure level is challenging. Essentially, since normal commercial TE materials are polycrystalline, current studies are limited by static results measuring millions of GBs. The experimental method proposed in this study can extract the single GB using an FIB to study its local effect on transport.

In this chapter, a comprehensive investigation of single GBs in highly Ag-doped PbTe on electrical transport was performed in the temperature range from 2 K to 300 K. Previous studies have proven that doping of Ag in PbTe largely improves energy conversion efficiency. [110, 37, 113] PbTe with Ag doping can also be utilized to examine the effect of element segregation at the GB. Firstly, the fabrication method is illustrated. Then, the investigation of GB scattering in Ag-doped PbTe is studied in detail, and different attempts to extract the resistivity of a single GB are described. The following section introduces correlative techniques for analyzing the microstructure of the single GB measured in the previous electrical test. The final part emphasizes how ion segregation leads to different GB scattering behavior. The result reveals an in-depth understanding of the individual GB effects on carrier transport and the corresponding impact of ion segregation on GB scattering.

4.2 FABRICATION METHOD: INDIVIDUAL GRAIN BOUNDARY SAMPLE

To solve the challenging local electrical measurement of a single GB, we have proposed a novel method to measure the charge carrier transport across an individual GB by combining a site-specific lift-out method with an FIB and nanodevice fabrication. Since it is the first attempt to fabricate a single GB device, we try to observe it under SEM scanning. In some cases, the outlines of grains were not clear. We adopted FIB to mill the sample surface for a while or change the FIB column to scan the polycrystalline bulk surface in order to determine the location of the grains. The whole process is similar to the fabrication process illustrated in the methods chapter.

Overall, this approach provides an accurate and efficient way to measure charge carrier transport across individual GBs and a successful beginning for the following work in this thesis. The sample fabrication and APT measurement were carried out by Jiaqi Wen, Yuan Yu and Riga Wu.

4.3 INVESTIGATION OF GRAIN BOUNDARY SCATTERING IN AG DOPED PBTE

4.3.1 *Two strategies to study a single GB device*

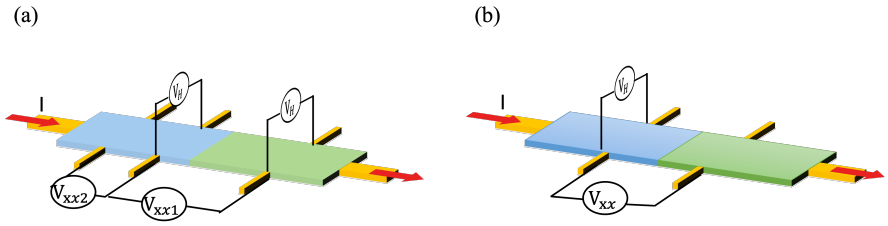

Figure 53: Two types of micro-electrode design: (a) eight electrodes: The grain boundary located vertically between the right four perpendicular electrodes in order to achieve the electrical measurement across grain boundary and neighboring grain; (b) six electrode: The grain boundary in the transferred lamella is placed between the perpendicular electrodes and required to align vertically. To compare with the electrical measurements of neighboring grains, another sample without a grain boundary is prepared.

Two types of micro-electrodes for single GB devices' electrical measurements are shown. The first type is an eight-electrode design depicted in Figure 53(a), which allows the measurement of both the GB region and neighbouring grain regions at the same time. The right four vertical electrodes are connected to do the electrical measurements across a single grain boundary, while the left four are used for the grain part's measurements. However, this design has certain disadvantages. It is difficult to fabricate, and the single GB must be placed between the right four vertical electrodes, with a distance of 4 μm. Moreover, the current flows through the entire sample, which

can affect the grain region. One possible improvement is to use an FIB to cut the sample at the GB region after measuring the GB sample, and then use the van der Pauw method to measure the physical properties of the grain part. However, this approach carries the risk of damaging the device by the ion beam. The second type of microelectrode discussed is a six-electrode design, which requires more fabrication time, but increases the success rate of the device. Two samples are required for comparison: one with an individual GB, and another one without GB. The design is sketched in Figure 53(b).

The APT investigation has also evolved in the experiment to correlate the local transport with atomic structure at the individual GB region. Initially, we planned to cut the APT sample from the measured device, which added to the difficulty of sample preparation and raised the risk of experimental failure. Therefore, we modified the method to cut the APT sample from the same GB region, parallel to the GB specimen.

4.3.1.1 *Resistivity measurement of device design I*

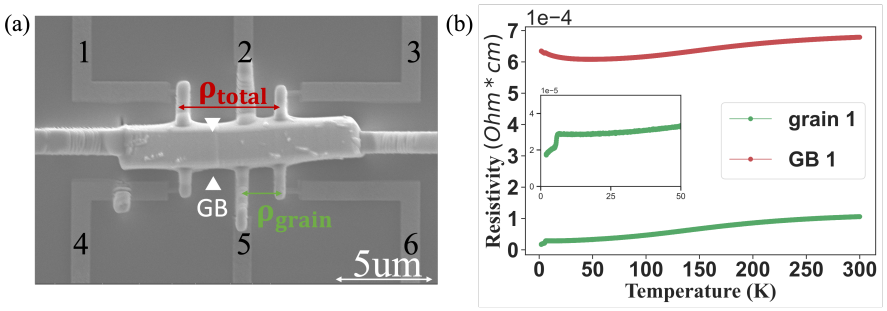

Figure 54: Simultaneous measurement: (a) SEM image of device containing a single grain boundary, denoted as GB1; (b) Temperature-dependent total resistivity and grain resistivity of the highly Ag-doped PbTe sample containing GB1.

The first experiment was conducted according to the device design I. The hall-bar geometry was used to measure both the voltage drop through the GB and the voltage drop of the pure grain portion not through the GB, as depicted in Figure 54(a). To assess the electrical resistivity of samples derived from the grain part and GB part, a two-step measurement was performed using different connections. A constant current was applied through the horizontal electrodes. The voltage drop between contacts 1, 3, 4, 6 was measured to determine the resistivity of the sample with a GB. Similarly, the voltage drop between contacts 2, 3, 5, 6 was measured to determine the resistivity of the sample without a GB. This approach was utilized to evaluate the GB's resistivity in this sample, as shown in Figure 54(b). For convenience, the GB sample is denoted as GB_1. The results indicate that the resistivity of the GB part is significantly higher than that of the grain part, with a total resistivity above 6×10^{-4} Ω·cm, which is around six times higher than that of the grain region. These findings demon-

strate that the simultaneous measurement approach can be used to study single GBs, albeit with high fabrication requirements.

4.3.1.2 *Resistivity measurement of device design II*

Due to the high failure rate in fabricating devices following this Design I, the device design has been proposed to study the GB effect in Ag-doped PbTe. The second experiment followed the device design II. A focus ion beam was utilized to extract the first lamella containing a GB, then directly extracting a second lamella from the pure grain near the GB. Figure 55(a) and (b) indicate the GB position selection under SEM and the specimen extraction.

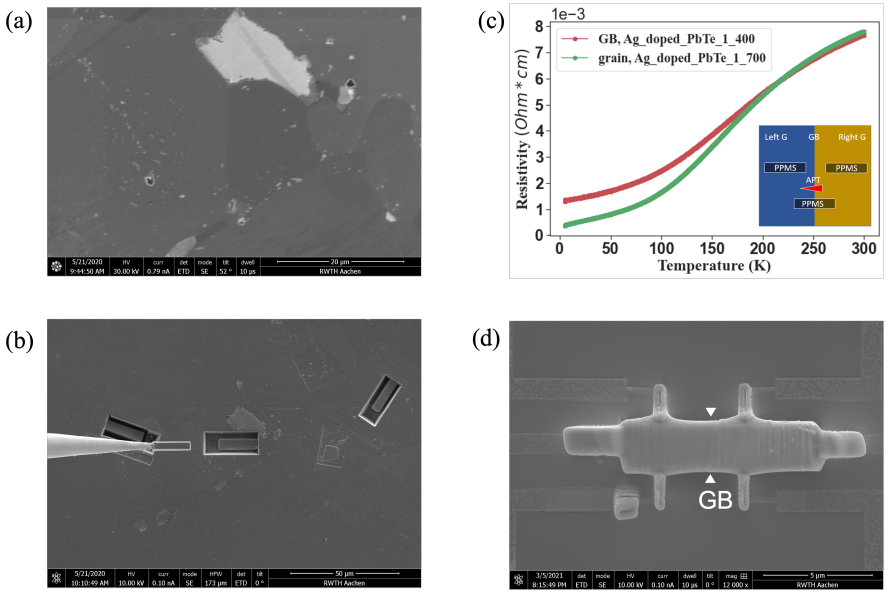

Figure 55: (a) SEM image showing the selected GB and its adjacent grains; (b) SEM image of GB and its corresponding grain lamella extraction process; (c) Temperature dependent conductivity of individual GB sample (red dot line), compared with its grain sample (green dot line); (d) SEM image of final device with single GB.

Figure 55(c) shows the temperature dependence of the resistivity in these two specimens. In the high-temperature range above 175 K, both samples' electrical resistivity coincides at higher temperatures, and these two values increase with the rise in temperature in the entire temperature range. This temperature dependence is characterized by a degenerate semiconductor. [37] At temperatures ranging from 2 K to 175 K, the electrical conductivity of the pure grain sample differs qualitatively from that of a sample having a GB. At 2 K, the sample with the GB has a higher electrical resistivity than the sample without GB, which is nearly twice larger. This difference in electrical conductivity can be traced to the influence of the GB. Furthermore, the significant discrepancy in the electrical resistivity of samples used in device designs I and II is attributed to inhomogeneous doping in highly Ag-doped PbTe. Figure 55(d) depicts the GB (denoted as GB_2) position between two voltage electrodes.

4.3.2 *Electrical properties of individual GB devices and their grain devices*

The measurements of electrical properties of two different individual GB samples are depicted in Figure 56. The electrical conductivity σ_{xx} of the GB and corresponding grain samples are derived from the resistance measurement with the four-point probe method, illustrated in Figure 56(a) and (b), which follows Ohm's law. The temperature-dependent carrier concentration n and mobility μ of the sample are displayed in Figure 56(c)-(d). The carrier concentration was determined from the slope of the resistivity in various magnetic fields in Hall measurement at each temperature level, while the mobility μ is then calculated using $\sigma = q\mu n$, in which q denotes the electron charge.

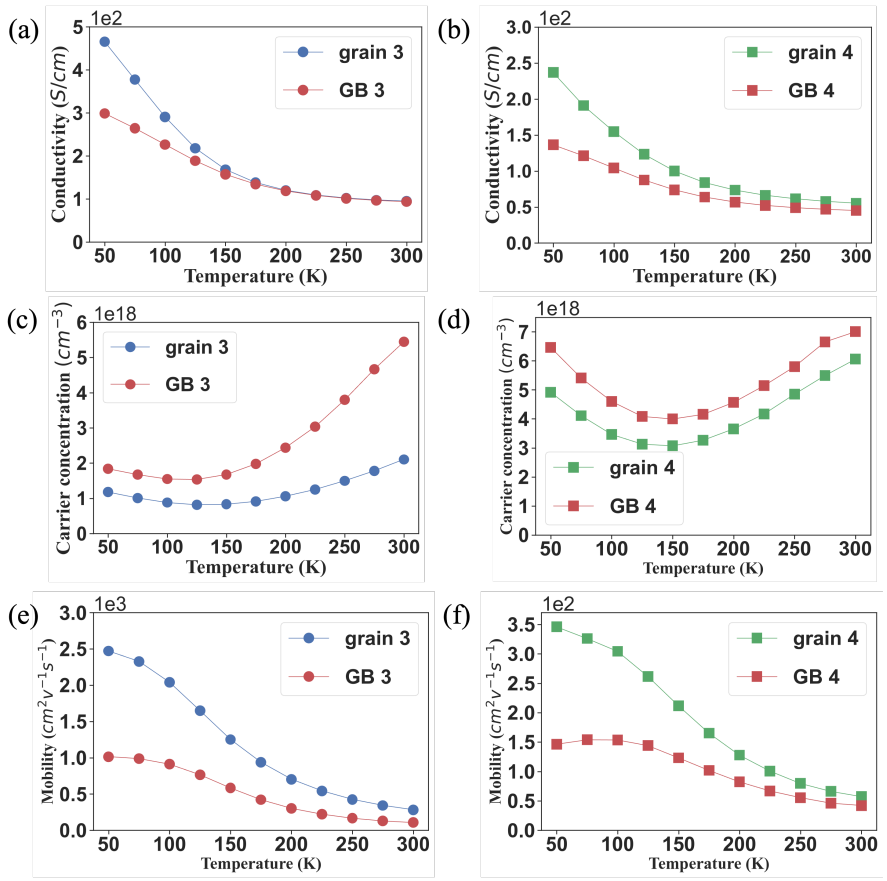

Figure 56: Electrical transport of individual GB sample and neighboring grain sample. Left side: GB_3 and its grain. Right side: GB_4 and its neighboring grain.

The negative slope of temperature-dependent conductivities shows the degenerate semiconductor behaviour in Figures 56(a) and (b). Single GB samples, represented by red curves (GB_3 and GB_4), exhibit lower conductivities than adjacent grain samples (green and blue curves) across all temperatures. Moreover, a large discrepancy between the conductivities of the two types of samples is observed at low temperatures (below 150 K). Essentially, at 50 K, the conductivity of the pure grain sample is 1.5 times higher than that of the sample

with GB_3. This difference in electrical conductivity can be traced to the influence of the GB.

As depicted in Figure 56(c) and (d), both the sample GB_3 and the pure grain display a similar trend of carrier concentration with temperature, with the carrier concentration reaching a minimum at approximately 150 K. At 50 K, the carrier concentrations have relatively large values in the order of $10^{18} cm^{-3}$. This is attributed to the high static permittivity and small effective mass of lead chalcogenides, which allows the Ag atoms to be completely ionized at very low temperatures. [38] The initial slight decrease in carrier concentration may be due to the gradual increase in the conduction band edge and thus, the increase in the difference between the Ag impurity levels and the conduction band edge with increasing temperature, which weakens the doping concentration of Ag. [114] As temperature continues to rise, the carrier concentration increases again, which is brought about by the dynamic doping effect. This effect is tuned by a temperature gradient, which influences the solubility of Ag in the PbTe matrix and leads to changes in carrier concentration. [36] Compared with the pure grain sample, the carrier concentration of the GB sample is slightly higher, as shown in Figures 56(c) and (f). The higher carrier concentration seen in GB_3 and GB_4 is caused by aggregated Ag atoms along the GBs, which work as reservoirs. [36, 64] Although these four samples' carrier concentrations are in the same order of magnitude, the distribution of carrier concentration is not uniform. The carrier concentrations of GB_3 and its grain are from $1.0 \times 10^{18} cm^{-3}$ to $5.0 \times 10^{18} cm^{-3}$, while the carrier concentrations of GB_4 and its grain are from $3.0 \times 10^{18} cm^{-3}$ to $7.0 \times 10^{18} cm^{-3}$. The large difference in carrier concentration is due to the Ag doping inhomogeneity of the grains and Ag segregation to GB. The samples are randomly extracted from various grains of the bulk material. The inhomogeneity of the grains and Ag segregation to GB will be discussed in detail in the following section.

In Figures 56(e) and (f), the mobilities of pure grain samples (blue and green curves) are higher than that of the sample with a GB (red curves). This is consistent with the conductivity results, which show that the value in the pure grain sample is higher than the one in the sample with a GB. Similar to the conductivity trend, there's a notable difference in mobility between grain and GB samples. Above 150 K, both types show decreasing mobility with rising temperature, and their mobility differences are relatively small. However, below 150 K, the mobility variation becomes more significant. At lower temperatures, the GB sample's mobility is substantially lower than that of the pure grain sample. For instance, at 50 K, the mobility of the pure grain sample is 2.5 times higher than that of the GB_3 sample, as depicted in Figure 56(e). Furthermore, the mobility of GB_4 displays thermally activated behaviour at low temperatures, a characteristic of the GB scattering effect. [44] Conversely, ionized impurity scattering, which also causes an increase in mobility with rising temperature, could also contribute to this effect. [115] This thermally activated mobility might be due to either ionized impurity scattering or GB scattering. To de-

termine the predominant scattering mechanism responsible for the thermally activated mobility and the significant variation in mobilities between grain and single GB samples, an analysis of the mobility curves at various temperatures is necessary.

4.3.3 *Scattering mechanism analysis in Ag doped PbTe*

The temperature dependence of the conductivity or mobility is evidence for the dominant electron scattering mechanisms. In fact, multiple scattering mechanisms exist in real materials, with certain types becoming dormant at certain temperature ranges. By analyzing mobility curves at different temperatures in grain and GB samples, the dominant scattering mechanism can be determined. [116, 44]

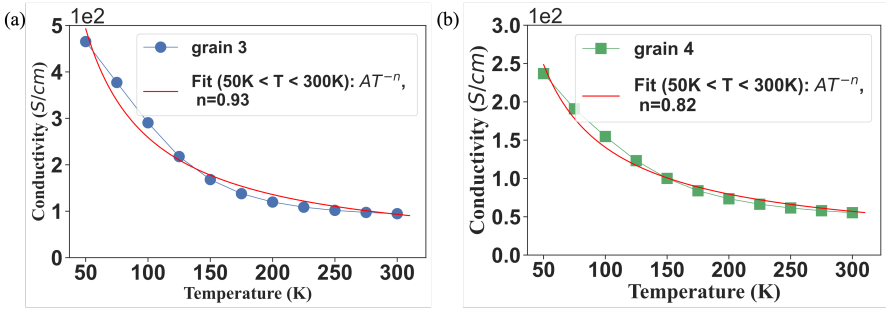

Figure 57: Fitting of scattering mechanism for grain 3 and grain 4 in temperature range (50 K < T < 300 K).

In PbTe, the dormant scattering mechanisms include both long wavelength acoustic phonon scattering and optical phonon scattering. The acoustic phonon scattering in reduced conductivity is characterized by a $T^{-2.5}$ temperature dependency due to the combined effect of temperature dependence of relaxation time and effective mass ($m^* \sim T^{-3/4}$ so that $\mu \sim (T/m^*)^{-3/2} \sim T^{3/2}$). The polar optical phonon scattering also leads to a decrease in conductivity with temperature. [117, 118] We use the function $\sigma(T) = A \cdot T^{-n}$ to fit the conductivity curves of grains 3 and grain 4, where A is a prefactor and n is the power law exponent. The result in Figure 57 indicates $n = 0.79$ and 0.82 in grain 3 and 4. The values of n are much smaller than the typical value of 2.5 for acoustic phonon and optical phonon scattering in PbTe. [37] This discrepancy suggests a suppression of the standard phonon scattering mechanisms, likely due to Ag doping effects that introduce additional scattering centers, such as dislocations or precipitates.[36, 119] The APT results, as shown in Figure 63 and discussed in the following section, confirm Ag segregation within the grains of the Ag-doped PbTe sample. PbTe have strong dielectric screening due to their high static permittivity. However, dislocations or precipitates can locally alter the dielectric constant, weakening the screening and enabling ionized impurity scattering, which may follow a $T^{1.5}$ power law. [120] This combination of charge carrier scattering mechanisms results in an effective temperature dependency closer to 0.8. This result implies that Ag doping modifies the scattering mechanism in PbTe, leading to mixed scattering contributions that reduce the im-

pact of phonon scattering on the overall temperature dependence of conductivity.

Due to the same temperature dependence of $T^{-2.5}$ for both mechanisms, it is hard to distinguish them in conductivity curves. According to lead chalcogenides studies, reduced conductivity or mobility is mainly due to acoustic phonon scattering as optical phonon scattering weakens below 77 K. Their inelastic nature precludes analysis using the relaxation time approximation. [121] When the temperature rises above 77 K, carrier concentration changes significantly, affecting scattering. In grain 3 samples with carrier concentrations below $4 \times 10^{18} cm^{-3}$, polar scattering becomes more pronounced in the temperature range between 77 K and 250 K. Conversely, when the concentration exceeds this threshold, acoustic phonon scattering continues to be prominent. [38] In this way, the acoustic phonon scattering dominates in grain 4.

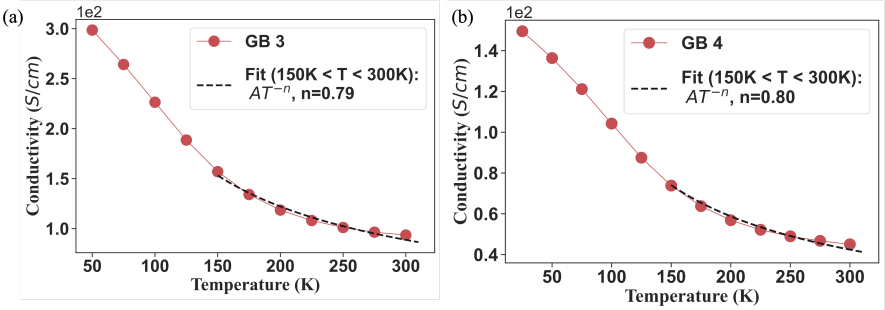

Figure 58: Fitting of scattering mechanism for GB 3 and GB 4 in high temperature range (150 K < T < 300 K).

The same fitting method is applied to the GB samples to illustrate the scattering mechanism. Figure 58 shows the fitting results of the conductivity curves of GB 3 and GB 4 samples in high temperature range. The power law exponent n is 0.79 and 0.80 in GB 3 and GB 4, respectively. This dindicates that the combined scattering mechanisms of acoustic phonon and optical phonon scattering also impact the GB samples in high temperature range above 150 K. However, at the low temperature range, the large variation in the conductivity and mobility between grain and GB samples still need to be explained further.

We employed the two-phase model to interpret the impact of GB-associated features on the electrical conductivity. In a series circuit, the conductivity of materials can be expressed as :

$$\sigma_{total}^{-1} = \sigma_{grain}^{-1} + (\sigma_{GB}^{-1} - \sigma_{grain}^{-1}) t_{GB} \tag{59}$$

where σ_{grain} and σ_{GB} refer to the grain phase and the GB phase, respectively, while t_{GB} is the size fraction of the GB phase. This two-phase model accounts for the effect of grain size on the electrical conductivity through t_{GB}. [109] The volume fraction of GBs is calculated by $t_{GB} = 1 - (\frac{d-h}{d})^3$, where d is the grain size and h is the width of the GB-phase. [122] Here, the width of the GB phase is assigned a value of 5 nm in accordance with the APT data later in this chapter. The grain size is obtained as 4 µm by the distance between two

voltage terminals. According to Equation 59, the contribution of grain interior to the total conductivity is excluded and the conductivity of the only GB (σ_{GB}) is calculated. Based on the GBs research, the GB interfacial conductivity can be expressed as:

$$\sigma_{GB} = \frac{\sigma_{GB}}{L_{GB}} = e^2 n_c \left(\frac{1}{2\pi m^* k_B T}\right)^{\frac{1}{2}} \exp\left(-\frac{E_b}{k_B T}\right) \tag{60}$$

where e is the electron charge, n is the carrier concentration of GB, m^* is the effective mass, k_B is the Boltzmann constant, E_b is the GB potential barrier height, and T is the absolute temperature. [123] To further extract the barrier height of GB, the equation is derived as:

$$\ln\left(\sigma_{GB} T^{\frac{1}{2}}\right) = -\frac{E_b}{k_B T} + \text{constant} \tag{61}$$

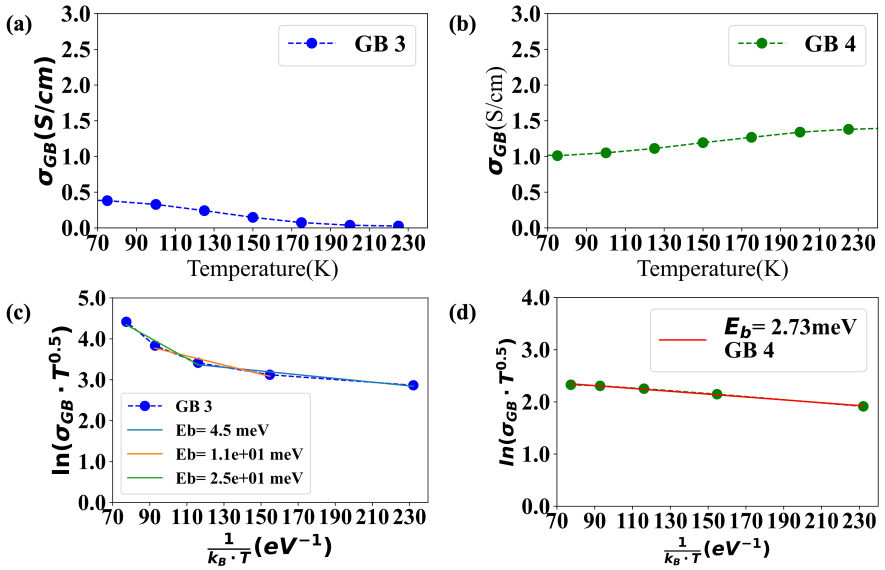

Figure 59: The calculated grain boundaries conductivity of GB_3 and GB_4 and their extracted GB potential barrier.

Figures 59 (a) and (b) present the GB interfacial resistivity of two GBs from two highly Ag-doped PbTe samples calculated using Equation 59. The temperature dependence of σ_{GB} can be used to calculate the GB potential barrier height according to Equation61. Figure 59(c) demonstrates that the $\ln(\sigma_{GB} \cdot T^{0.5})$-T curves of GB 4 fits well with the linear fitting, with a barrier height of $E_b = 2.73$ meV. Whereas, The corresponding curve of GB 3, shown in Figure 59(d), is nonlinear. The average barrier height of GB 3 is $E_b = 13.5$ meV, determined from the linear slope of every three data points. This value is much higher than that of GB 4. The large difference in the barrier heights of GB 3 and GB 4 might be attributed to the different local composition and microstructure of GBs in highly Ag-doped PbTe. This finding is supported by related research, which suggests that Ag segregation at grain boundaries impacts their composition and microstructure, and consequently influences the electrical conductivities. [111, 112]

4.4 CORRELATIVE TECHNIQUE COMBINING ATOM PROBE TOMOGRAPHY WITH LOCAL ELECTRICAL MEASUREMENT

From the analysis of the result shown in Figure 56, GB scattering happens in both GB_3 and GB_4 samples. Yet, a difference in the variation of mobility in these two GB samples has also been pointed out. The strength of GB scattering is affected by the grain size and ion segregation at GB. [124, 109] Since the measured sample is highly doped PbTe, the ion segregation at GB is an essential factor in influencing the GB scattering. Therefore, the correlative APT measurement is an effective approach to reveal the atomic structure of GB. We have initiated a "one-to-one" correlative technique by combining APT with local electrical transport at the GB, which allows for the correlation of the transport properties of GB with its chemical composition and microstructure.

The correlative atomic structure and local transport results for GB_3 are depicted in Figure 60. The needle-shaped specimen containing the GB_3 is investigated by APT, quantifying the Ag content at the boundary and the compositional changes of the matrix elements. The reconstruction of atomic arrangement in Figure 60(a) shows Ag ions segregated to GB. The composition profile in the middle of Figure 60(c) reveals that the Ag concentration at the GB is slightly lower than 10 at.%, which is higher than the Ag concentration in the grain interior. This confirms that the Ag segregation at grain boundaries in doped samples also plays a role in reducing the mobility or conductivity, not only the GB scattering effect. [125] When discussing the reduction in mobility or conductivity due to GB scattering, it is essential to consider the microstructure and chemical composition at the GBs for a thorough analysis.

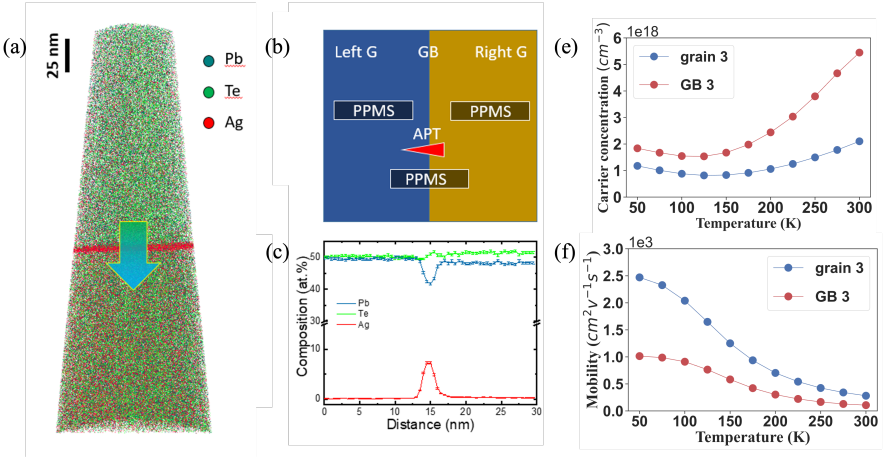

Figure 60: Correlative microscopy applied to study the effect of the grain boundary for Ag doped PbTe: (a) 3D reconstructed tip with GB_3; (b) schematic diagram showing the position of this APT sample with GB_3 and meassured devices extracted from the GB_3 and its grain regions; (c) composition profile of Pb, Te and Ag in the GB_3; and the corresponding local transport properties of GB_3 and its neighboring grain: (e) temperature dependent carrier concentration; (f) temperature dependent mobility.

4.5 DIFFERENCE IN PERFORMANCE ON GRAIN BOUNDARY SCATTERING CAUSED BY SILVER SEGREGATION

In the last section, the APT correlative measurements have shown that the Ag segregation at boundaries might influence the electrical conductivity or mobility of the GB. In this section, we will discuss the influence of Ag segregation on the electrical conductivity of the GB and grain.

4.5.1 *Correlative analysis of grain boundary samples*

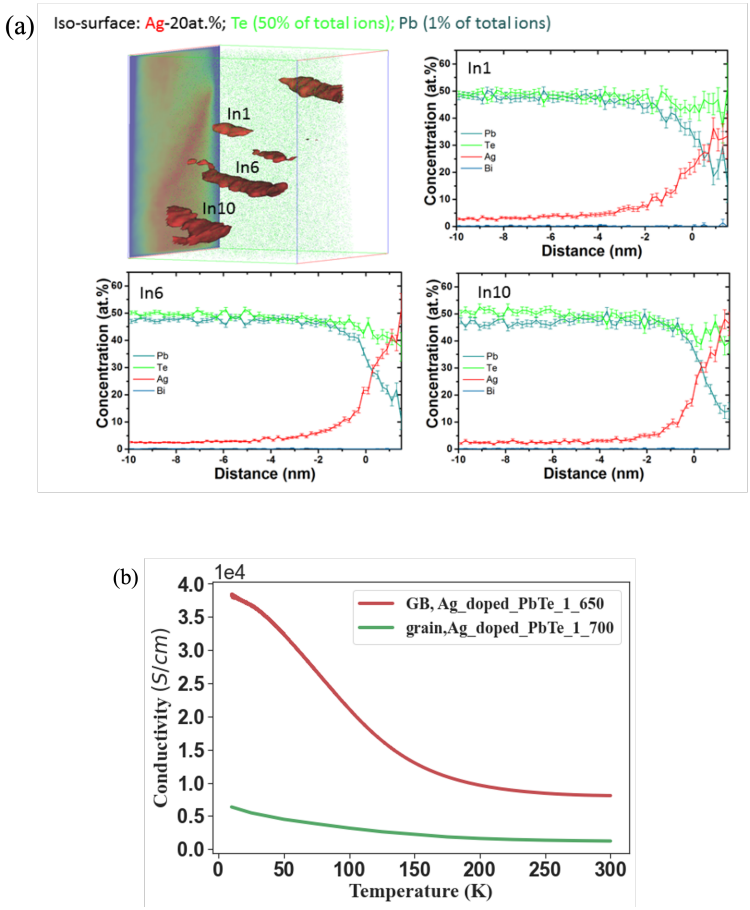

Figure 61: (a) APT result and (b) corresponding temperature dependence of conductivity: supersaturated Ag at GB enhances its electrical conductivity.

By utilizing the correlative technique, the variations of GB resistivities have been explained by the corresponding atomic distribution provided by APT measurements. It is evident that Ag segregation occurs near the GB area. In Figure 61(a), some Ag-rich precipitates at the grain border are observed in the reconstruction of the specimen, extracted at the same GB as the single GB device. The chemical composition of these Ag-rich precipitates with an average concentration of 20 % at the GB is detected from the cuboid region of interest, as depicted at the bottom of Figure 61(a). These supersaturated Ag precipitates enhance the electrical conductivity of TE materials. The

corresponding resistivity measurement results shown in Figure 61(b) are consistent with this hypothesis.

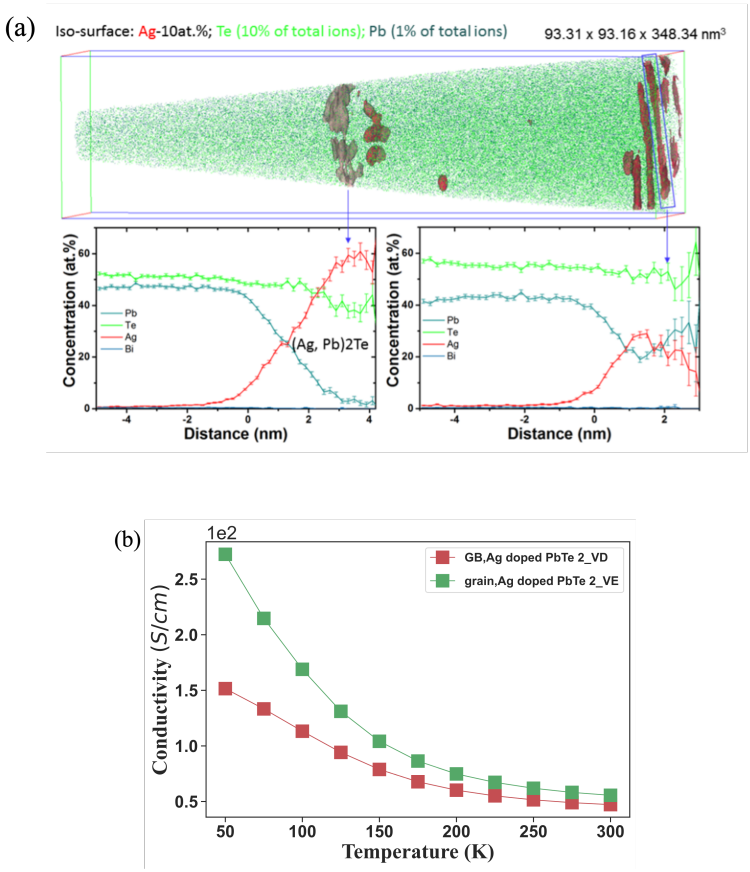

Figure 62: (a) APT result and (b) corresponding temperature dependence of conductivity: secondary phase formed at GB strengthens GB scattering.

Another type of Ag segregation observed by APT reveals a second phase in Figure 62(a). As the composition profile, the Ag concentration at the GB is 60 at%, indicating that the Ag atoms have partially replaced the Pb atoms to produce a secondary phase Ag_2Te. The secondary phase of a material serves as a scattering center, restricting the motion of charge carriers. As a result, the electrical conductivity of the GB sample in Figure 62(b) will be drastically reduced.

4.5.2 *Correlative analysis of grain samples*

In the first section, the larger variation observed in the magnitude of electrical conductivity in GB1 and GB2 is explained by the doping introducing an inhomogeneity in the GB and grains. With the correlative APT-PPMS technique, the influence of inhomogeneous doping in the grain on the electrical conductivity can be further investigated.

These measured grains are single grains, randomly selected from the bulk material. In the temperature-dependent conductivity plot in Figure 63(a), the red line of grain 2 has significantly more conductivity than the other two lines, representing grain 1 and grain 3. Essentially, a superconducting transition is observed in the temperature-

dependent resistivity data of grain 2 at 7 K, as shown in Figure 63(b). The curves of grain 1 and grain 3 exhibit a small change in conductivity over the temperature range from 2 K to 300 K. This finding is caused by the inhomogeneous Ag doping in PbTe. Since the cubic lattice structure of PbTe is isotropic, the difference in electrical conductivity across the grains can be attributed to their different chemical composition profiles.

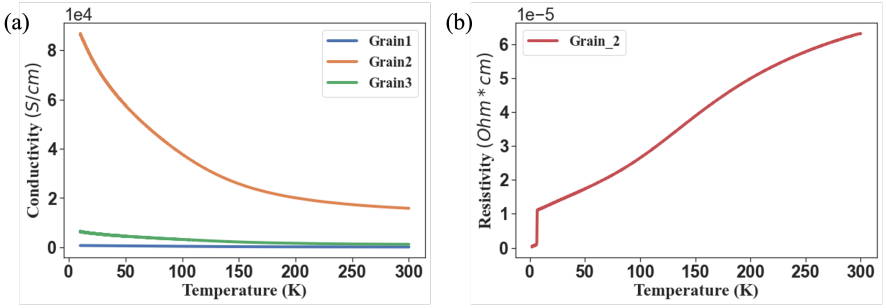

Figure 63: (a) The variation in temperature dependence of conductivities in grains 1, 2, 3; (b) the superconductivity observed in temperature dependent resistivity data, which is for the Pb-rich filament in grain 2.

The APT results of the three grains are shown in Figure 64. 20 at.% Ag has been observed in grain 1, while no Ag has been detected in grain 2 and grain 3. The Ag segregation in grain 1 scatter the charge carriers, resulting in a decrease in electrical conductivity. That is why the conductivity of grain 1 is the lowest among the three grain samples. The superconducting-like transition in the temperature dependence of the conductivity of grain 2 can be explained by the 3D atomic reconstruction in Figure 64. Numerous Pb-rich tubes are detected in grain 2.

These Pb-rich tubes are not composed of pure elemental Pb. Instead, they represent regions of increased Pb concentration within a PbTe matrix, forming a Pb-enriched telluride phase. This is due to the thermodynamic preference for maintaining a telluride structure rather than segregating into pure Pb metal. The presence of Te within these regions, as shown by the corresponding concentration profile in Figure 64, supports this interpretation. The charge carriers can pass through Pb-rich tubes with low resistance as the fast route and be scattered less, resulting in a dramatic enhancement in conductivity. The APT result for grain 3 (Figure64) demonstrates a uniform distribution of Pb and Te. Even though the APT possesses great chemical sensitivity, no Ag atoms in the PbTe matrix have been identified. These different microstructures of the grains in Ag-doped PbTe also indicate the low solubility of Ag in the matrix of PbTe, which is also a challenge for Ag doping in PbTe. [37, 36] The doping in TE enhances the carrier concentration and phonon scattering, but the precipitates and other nanotubes introduced by doped ions can also decrease the electrical conductivity.

The analysis of the chemical composition of the three single grains suggests that compositional non-uniformity can lead to a local vari-

ation in electrical conductivity, as demonstrated by Shi et al. [126] The structural and compositional non-uniformity can influence not only the electrical conductivity, but also the Seebeck coefficient and thermal conductivity. Because inhomogeneity can cause large fluctuations in the performance factors of TE materials, obtaining samples from different positions in the bulk material for testing might lead to inaccurate performance estimates. In order to attain a more stable performance in TE materials, it is essential to reduce the inhomogeneity.

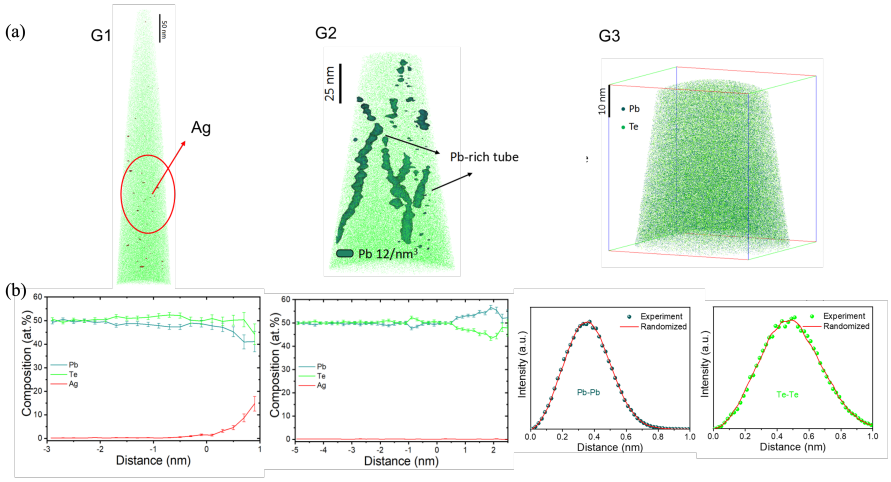

Figure 64: (a) APT images of grains G1, G2, and G3. G1 shows Ag segregation (circled in red). G2 displays Pb-rich tubes (dark green regions) with elevated Pb concentration (~ 12 atoms/nm^3). G3 shows a uniform Pb and Te distribution. (b) Composition profiles: G1 highlights Ag presence with stable Pb and Te; G2 shows increased Pb in the tube regions while Te remains present, indicating a Pb-rich telluride phase; G3's Pb-Pb and Te-Te intensity profiles match experimental and randomized data, confirming uniformity.

4.6 CONCLUSION

This chapter investigated the individual GB in Ag-doped PbTe using a novel FIB-assisted device fabrication. The findings reveal intriguing insights into the electronic properties and chemical composition of the individual grain boundaries. Specifically, the study confirms the effectiveness of the technique in observing the GB scattering effect on individual GBs, resulting in a reduction of the mobility and conductivity due to the creation of a potential barrier. Additionally, the correlative technique combining local electrical measurements with APT enables the observation of the influence of atomic structure and compositional fluctuation on the GB's electrical properties. The study highlights the critical issue of compositional heterogeneity's significant impact on electrical conductivity within individual grains, which has been largely overlooked in prior investigations. Moreover, APT characterization reveals that Ag segregation at the GB enhances the electrical conductivity, while the second phase, formed by Ag replac-

ing Pb atoms, serves as a scattering center. The study finds out that obtaining precise GB resistivity helps in designing higher-performance TE materials. The resistivity of the GB can be determined by subtracting the averaged resistivity of the neighboring grains from the total resistivity with the GB using the model presented by Adam W. Tsen et al. [122]

5

MISORIENTATION-ANGLE DEPENDENT ELECTRICAL TRANSPORT AT INDIVIDUAL GRAIN BOUNDARY IN PBTE

5.1 INTRODUCTION

Grain boundaries, typical line defects, result in intriguing electronic and mechanical properties. [127, 128, 66, 54] In semiconductors, GBs serve as scattering sites for both charge carriers and phonons. In thermoelectrics, the ZT value can be derived as $ZT = eT(S^2n)\frac{\mu}{k}$ to illustrate the charge carrier and phonon transport, in which n represents the carrier concentration, and the ratio $\frac{\mu}{k}$ signifies the ratio of carrier mobility to phonon thermal conductivity. [28, 34, 19] The ratio of μ to k_L is generally used to judge whether one strategy is beneficial for ZT or not. Grain refinement engineering is a common strategy to enhance the ZT value by reducing thermal conductivity via GB engineering. [4] This strategy is based on the fact that the introduction of GBs can scatter phonons more effectively than charge carriers. When the average free path of phonons is much longer than that of electrons in a bulk material, it is believed that refining the grain size to below the electron free path can effectively reduce lattice thermal conductivity without sacrificing electrical conductivity. However, there are exceptions. Snyder and his team reveal that GB scattering is the primary mechanism influencing charge transport in Mg_2Sb_3, whose ZT performance at room temperature makes it competitive with commercial bismuth telluride. [116] Thus, it is essential to explore the effect of GBs on electrical transport for achieving optimum TE performance, especially considering the prevalent use of polycrystalline in industry.

As an interface between two grains with different orientations in polycrystalline material, GB can be described crystallographically by the misorientation angle between adjacent grains. [129] With 5 macroscopic degrees of freedom, multiple types of boundaries form. [130] These various types of GBs have different influences on charge carriers passing through them. Furthermore, the presence of composition gradients, ion segregation, and even dangling bonds at the GB also affect its local physical properties. [131, 132] The complexity of GB's atomic structure results in unique physical properties for different GB types. The GB transport research in two-dimensional materials has demonstrated that only tilt GBs degrade the carrier transport and lower their mobility or electrical conductivity. [133, 134] Focusing on an individual GB and its atomic structure in correlative characterization is necessary to better understand how GBs alter specific properties.

To access a single GB, the most challenging technique for the direct measurement of its electrical transport properties is to isolate particular GBs from the bulk so that their transport mechanism can be de-

termined. Previous GB studies in grain refinement engineering of TE materials measured a macroscopic electrical property of a polycrystalline bulk sample by changing the grain size and then normalizing it by the number of grains using mathematical models. [3] However, this method only yields average electrical properties over numerous grains, potentially obscuring the distinct behaviors and contributions of individual boundaries. A different, promising strategy for examining a single GB in two-dimensional materials involves the growth of bicrystals and then measuring across a single GB. [122, 135] However, it is usually challenging to grow bicrystals of TE materials. Expanding the available methodologies, an alternative technique has been developed for metals, i.e., copper, using a specialized setup equipped inside a FIB system. This setup includes piezo-driven micromanipulators that precisely inject current and measure the voltage drop across a GB. In this way, this technique accurately determines the electrical resistivity of a single GB by the four-point probe method. [5, 6, 7] However, this method requires a specialized setup and is solely capable of determining resistivity, providing only a single value. Therefore, it is demanding to find a more flexible way to isolate a desired GB from the bulk sample. This will give a chance to explore an emerging phenomenon that exists only in GBs.

5.2 AIM AND NOVELTY OF THE CORRELATIVE TECHNIQUE

The novel experimental method combining a FIB and a nanodevice fabrication technique to examine the target individual GB from bulk PbTe has been applied again in this chapter. We determined the misorientation angle of the selected GB via EBSD. As an example of the 45°single GB, the electrical properties measurement and corresponding APT analysis have been studied in detail. Then, a systematic investigation of individual GBs with different misorientation angles has been conducted to reveal the dependence of GB scattering on misorientation angle. This observation has been explained by APT analysis. The APT results indicate the variation of doped Ag concentration and different chemical bond-breaking behavior between LAGBs and HAGBs.

The advantages and novelty of this correlative study are manifold. Firstly, it is possible to extract any target GB from millions of randomly distributed GBs in bulk with the help of a FIB. Secondly, before conducting an electrical measurement on a GB, EBSD can characterize it to help in selecting a target GB. Further, the entire process, from choosing a target GB to characterization and, finally, sample fabrication, can be carried out inside the FIB system. These facts significantly enhance the efficiency of device fabrication. Thirdly, unlike GB research in metals or other solids, transport measurements are not restricted to a narrow temperature range and can get only GB resistivity. [5, 6, 7, 136, 137] Fourth, the GB tomography and compositions can be revealed by APT, which has no 2D projection effect and much higher chemical sensitivity than the electron-beam-based techniques

such as TEM [8, 9] and associated EDS. Lastly, the unique attribute of APT to capture the bond-breaking behavior can provide information on the chemical bonding mechanism at and aside from the GB. [10] This will greatly enrich our understanding of the origin of GB charge carrier scattering by taking the structure, composition, and bonding into account.

5.3 FABRICATION METHOD: INDIVIDUAL 45° GB SAMPLE

The experiment has been outlined comprehensively in detail in chapter 3. As schematically shown in Figure 65(a), EBSD was first utilized to characterize different types of GBs and mark the interesting GB with a certain misorientation angle. The orientations of bulk PbTe are characterized by EBSD microscopy in Figure 65(b), confirming a selected GB with a 45° misorientation angle. Subsequently, the lift-out was performed by employing the micro-manipulator with a dual beam FIB system. A well-shaped cuboid lamella with defined dimensions can be prepared by carefully cleaning the surfaces using the FIB. This lamella is then transferred onto gold nano-electrodes. Figure 65(d) presents the final configuration of the measurement device in a Hall-bar shape, in which the GB is located in the middle of two voltage electrodes as indicated by the arrow. In order to correlate the atomic structure, stoichiometry and local electrical transport of the 45° GB, the specimen is extracted for APT analysis from closely spaced positions at the same 45° GB region. Subsequently, APT specimens are prepared using FIB, as shown in Figure 65(e). The TKD profile of this APT specimen with a 45° GB is sketched in Figure 65(f). In this way, atom probe tomography and local electrical transport measurement of a 45° GB can be correlated.

To make a comparison of the GB effect in grain and GB region, we extract three lamellas across the GB, the neighboring right grain and left grain, representing the red, dark gray and light gray slots in Figure 66(a). The final device with this 45° GB shown in Figure 65(d) is 3 μm wide and 1.55 μm thick. The distance between the two voltage electrodes is 4 μm. The sample fabrication and APT measurement was carried out by Shuo Jia, Marco Wegener and Riga Wu.

5.4 LOCAL ELECTRICAL TRANSPORT AND APT MEASUREMENT OF INDIVIDUAL 45° GB

5.4.1 *Electrical transport of individual 45° GB*

Electrical measurements conducted by Dynacool were performed on the 45° single GB and its adjacent left and right grain device to allow single GB and grain sample comparison. Four electrical contacts were manufactured parallel to the GB so that the overall current flow applied by the two horizontal electrodes occurs perpendicular to the GB to avoid the different GB direction impact on the transport. The en-

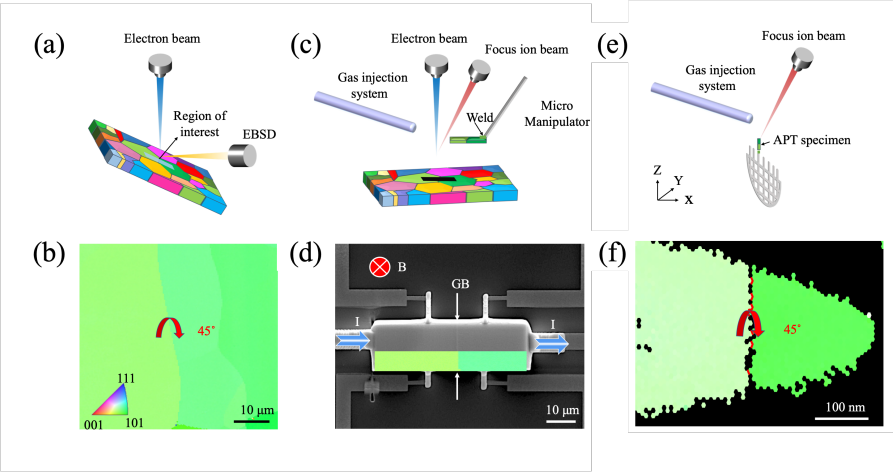

Figure 65: Schematic diagrams of an individual GB device fabrication process: (a) Identifying target GB with SEM, EBSD, and FIB; (b) EBSD map revealing a 45° misorientation angle in GB; (c) Individual GB lamella lifted out and transferred with FIB and gas injection; (d) Hall-bar geometry device with a lamellar sample containing a 45° GB and mounted on a Si/SiO_2 substrate pre-deposited with gold electrodes; (e) APT specimen cut from the same GB for PPMS measurement; (f) Misorientation angle and position of GB confirmed in TKD image of APT specimen, matching the PPMS sample.

tire electrical measurement results are summarized in Figure 66. The temperature range was from 10 K to 300 K.

For the 45° GB in Figure 66(b), representing the red dots, the mobility rises initially and subsequently decreases with increasing temperature, reaching the maximum value of $3 \times 10^3 cm^2 V^{-1} s^{-1}$ at 100 K, in contrast to the linear behavior of two gray dots, denoted two grain devices over the entire temperature range. The existence of GB might cause an apparent difference between GB and grain samples. For the two grain samples, the monotonously decreasing mobilities of grain devices follow the relation $\mu(T) \sim T^{-2.5}$, showing the acoustic phonon and optical phonon scattering in PbTe. [117] In the high-temperature range above 100 K, the trend of red dots, representing the single GB's mobility, closely resembles the value of light and dark gray dots, denoted the left and right grain devices. The slight deviations just come from the error in the sample geometry. Furthermore, at low temperatures, the mobility of two grain devices is also higher than that of a single GB device. At 10 K, the mobility in crystalline grains is roughly $7 \times 10^3 cm^2 V^{-1} s^{-1}$, which is 3 times larger than the GB sample. It once again proves the ability of GB to restrict the carrier motion. This different scattering mechanism will be analyzed in the next section.

Besides GB scattering, the ionized impurity scattering is another possible origin, which results in the thermally activated mobility $\mu(T)$ or conductivity $\sigma(T)$. [138] However, no thermal activation is observed in the grains. Therefore, the thermally activated mobility in the single GB device can come from the carrier scattering at the GB.

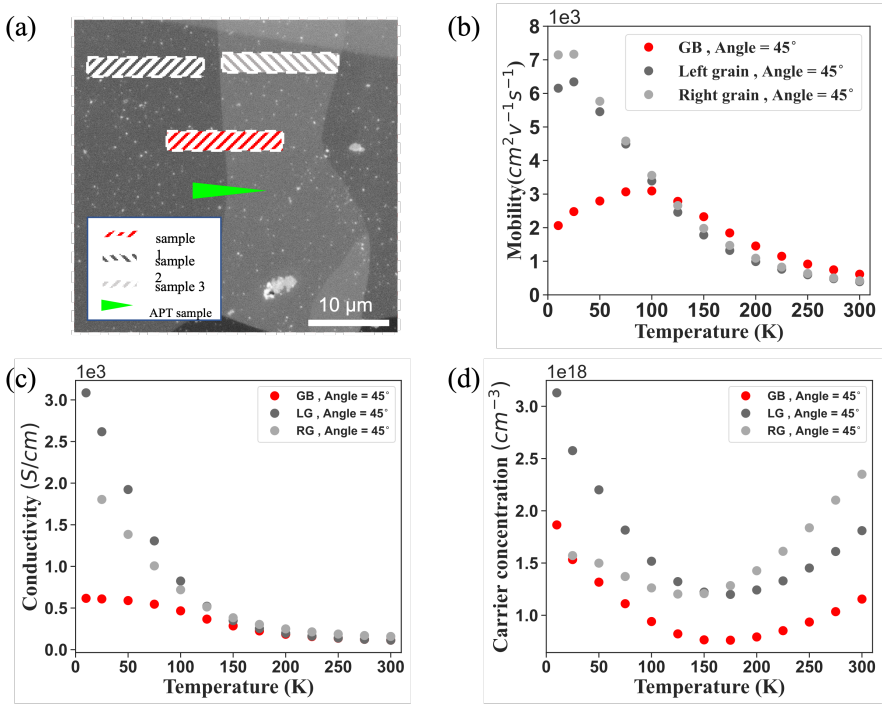

Figure 66: (a) SEM image of a 45° GB in PbTe, highlighting the locations where samples were cut from the left grain, GB, and right grain. An APT specimen, marked by a green triangle, was extracted from the same GB. (b) mobility as a function of temperature (c) Conductivity as a function of temperature. (d) Carrier concentration versus temperature for the left grain, GB, and right grain samples.

The GB scattering effect also leads to a different performance in the conductivity as a function of temperature, as shown in Figure 66(c). At temperatures below 150 K, the conductivity of the grain samples is 4-6 times larger than one of single GB sample, as displayed by the dark gray and gray dots, which are much higher than the red dots. For the carrier concentration, Figure 66(d) displays a self-doped semiconductor character: the carrier concentration of all samples drops to its lowest value at around 150 K and rises again as the temperature increases further.

5.4.2 *Grain boundary scattering analysis of individual 45° GB*

The different behavior in mobility with respect to temperature should originate from the variation of the dominant scattering mechanism. This can be deduced from the significant change in the temperature exponent (p) of electrical mobility ($\mu \propto T^p$) and Arrhenius form of trapping state model at GBs region. In PbTe, longitudinal acoustic phonon scattering dominates at high temperatures, following $\mu \propto T^{-2.5}$. The presence of grain boundaries (GBs) hinders charge carrier movement due to a potential barrier E_b, which can be described by an Arrhenius-type trapping state model: $\mu \propto \exp\left(\frac{-E_B}{k_B T}\right)$.

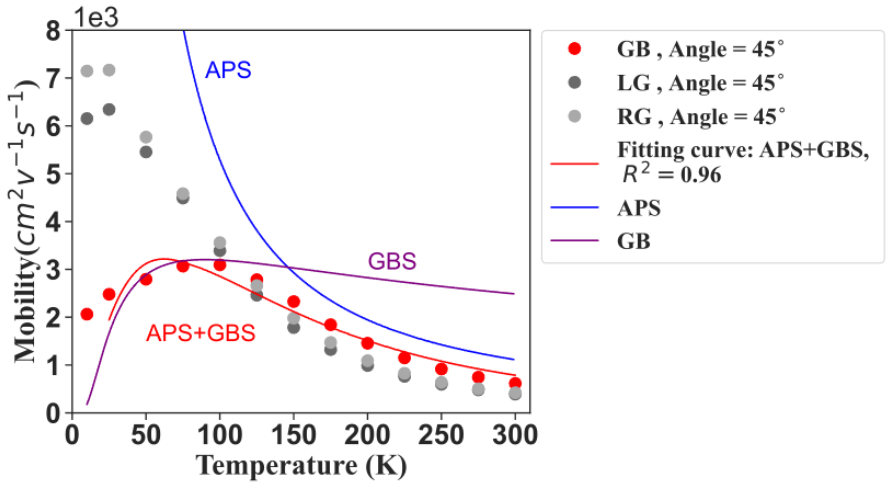

Figure 67: Fitting curves of the scattering mechanism at different temperature range in the 45° GB, its correlating left and right grain samples.

In Figure 67, the red fitting line, which presents the combined scattering mechanisms caused by acoustic phonons and this 45° GB region, shows a good fit with the red dots from this single GB sample. Consistent with the property that GB scattering occurs at low temperatures and diminishes as the temperature rises, the purple fitting curve matches well with the measured red data points in the temperature range from 50 K to 125 K. This indicates that the GB scattering mechanism is dominant in this temperature range. When the temperature exceeds 125 K, acoustic phonon scattering, shown by the blue line, takes over to reduce the mobility of the charge carriers. The two gray dotted lines from the neighboring grain samples also follow the same scattering mechanism at high temperature range. In addition, the tunneling mechanism governs the carrier transport in the temperature below 50 K. [139]

5.4.3 *APT measurement of 45° individual GB*

To understand the temperature dependent mobility behavior of 45° GB, we studied its microstructures by means of ATP. The misorientation values of the APT specimen extracted from 45° GB were resolved by correlating high-resolution TKD as shown in Figure 66(c). The 3D reconstruction of this specimen in Figure 68(a) shows the distribution of Pb, Te and Ag around the GB region and the aggregation of Ag ions at the GB region. The detector hit maps in Figure 68(b) and (c) are slices in the tip, obtained from two neighboring grain regions. The poles in the detector hit maps (b) and (c) correspond to the (002) and (111) crystallographic planes, respectively. Figure 68(d) exhibits the GB region containing ~ 1at% Ag. The higher concentration of Ag at the GB region compared to the grain region suggests that the space charge at GB could be due to Ag aggregation. As the schematic image in Figure 68(e), the GB repels the electrons in the n-type PbTe, leading to an upward band bending of the conduction band, thus creating a

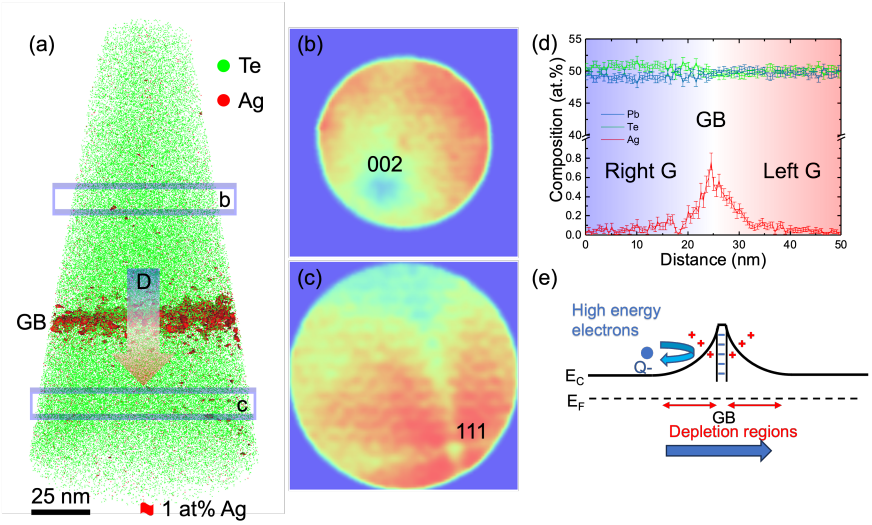

Figure 68: APT reconstruction result and composition analysis of a 45° GB region in PbTe: (a) 3D distribution of Pb (blue dots), Te (green dots) and Ag (red dots). The GB is highlighted by Ag 1at% isocomposition surface. Detector hip maps represent slices at different depths within the tip, corresponding to the blue boxes in part (a), taken from two adjacent grain regions. (d) proximity histogram of the 45° GB region showing each element's composition. (e) Schematic diagram of the energy band around the GB of n-type PbTe.

potential barrier. This barrier can prevent electrons from easily moving through the semiconductor, increasing conductivity and mobility in that region. This explanation is consistent with the analysis of the charge scattering mechanism in the temperature-dependent mobility results of the 45° GB sample, as shown in Figure 67.

5.5 MISORIENTATION ANGLE DEPENDENT ELECTRICAL TRANSPORT AT INDIVIDUAL GRAIN BOUNDARY IN PBTE

Several papers have discussed GB and interface transport in metals, two-dimensional materials, and solar cells, where it has been found out that mobility varies with mismatch angle. [122, 8] A definitive trend explaining this variation, especially in TE bulk samples, still requires further investigation. To verify this hypothesis, a systematic study of different misorientation angles has been undertaken. In this work, we explored individual GB devices, analyzing how varying misorientation angles affect their electrical properties, as listed in Table 2. The range of misorientation angle starts from 3.5° and expands to the high angle grain boundaries(HAGBs) region, reaching a maximum angle of 54°.

Table 2: Summary of measured devices with individual GBs.

Device number	**Device type**	**Angle(°)**	**Mobility ($cm^2\,V^{-1}\,s^{-1}$)**	**Critical temperature (K)**
1	HAGB	54	$3.35 \times 10^3 \pm 1\%$	50
2	HAGB	45	$3.09 \times 10^3 \pm 1\%$	100
3	HAGB	41	$3.40 \times 10^3 \pm 1\%$	25
4	LAGB	7	$5.42 \times 10^3 \pm 1\%$	25
5	LAGB	4.8	$1.29 \times 10^4 \pm 1\%$	25
6	LAGB	3.5	$1.35 \times 10^4 \pm 1\%$	25
7	grain	grain	$1.44 \times 10^4 \pm 1\%$	25

GBs are characterized by the Miller indices of the grains and rotation angle. The Miller indices can present the rotational and translational degree of freedom to define the grain boundaries.[140] Here, we focus on the tilt GBs (the rotation axis is parallel to the boundary plane), which are the most common type of GBs in polycrystalline PbTe. The misorientation angle of the GBs is defined by the rotation angle between the two neighboring grains. According to the misorientation angles, GBs can be divided into two categories: low angle GBs (LAGBs) and high angle GBs (HAGBs). When the angle is smaller than 15°, the GB is labeled as an LAGB. The LAGB is composed of a periodic set of dislocation cores. The dislocation cores are the main feature of LAGBs and the main source of scattering. The density of dislocation in LAGB rises with the misorientation angle. When the angle is larger than 15°, the grain boundary is labeled as a HAGB. The HAGB is a complex region with many overlapped dislocations and a high density of point defects. [130] Grain boundaries and their characteristic rotational parameters can be observed by EBSD.

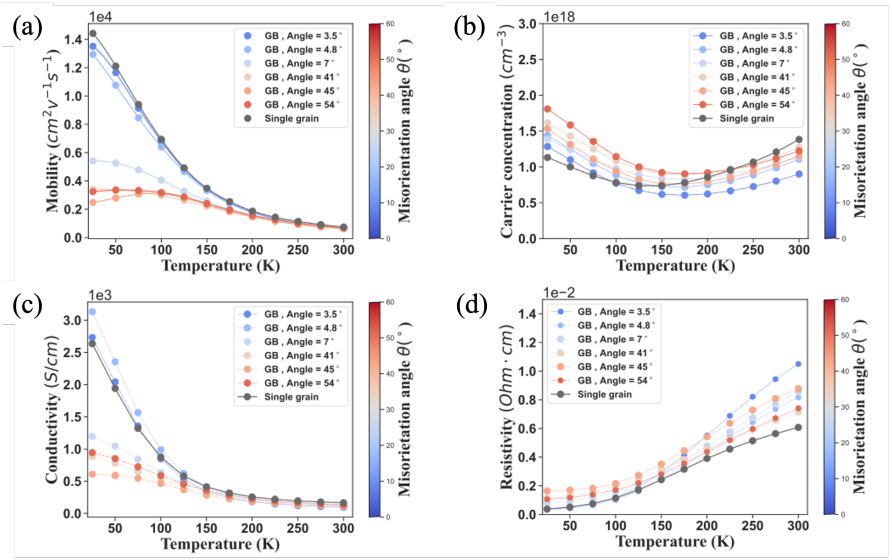

Figure 69: (a) Temperature dependence of mobilities; (b) carrier concentration; (c) conductivity, and (d) resistivity for various misorientation angles.

5.5.1 *Local electrical transport measurement*

The measurement of LAGB and HAGB samples have been conducted from room temperature down to 25 K. The results show how these individual grain boundaries' electrical properties change as a function of misorientation angle.

Figure 69(a) shows the temperature-dependent Hall carrier mobility for GBs with varying misorientation angles θ. As the misorientation angle increases, the overall mobilities of these GB samples decrease. The color bar indicates the change in misorientation angle from blue (LAGB) to red (HAGB). The red curve (HAGBs) always lies below the blue curve (LAGBs).

When considering temperature as the varying factor, all GB samples exhibit a similar trend of decreasing carrier mobility due to the dominance of acoustic and polar optical phonon scattering in charge transport at high temperatures. [141, 117] At low temperature ($T < 150$ K), the LAGB and HAGB samples exhibit distinct behaviors at low temperatures: the mobility in LAGB samples with angles of 3.5° and 4.8° shows a linear decrease from 25 K to higher temperature range. In contrast, the HAGB sample's mobility exhibits a strong GB scattering effect, with the mobility increasing up to 150 $cm^2v^{-1}s^{-1}$ and then decreasing as the temperature continues to rise. A larger misorientation angle leads to a more pronounced thermally activated behavior. The results obtained in this study are consistent with previous findings in magnesium antimonide (Mg_3Sb_2) alloys and strontium titanate ($SrTiO_3$) ceramics that reported the mobility in polycrystalline materials is suppressed by GBs, whereas in single crystalline materials, it increases linearly with temperature. [116, 66]

One single-grain sample was also measured for reference. This single-grain sample's carrier mobility monotonously decreases with

increasing temperature due to the increased thermal occupation of phonons, leading to an increase in electron-phonon scattering. [19] Furthermore, although the single-grain and LAGB samples exhibit similar linear behavior, the GB mobility value is still lower than that of the single-grain. This demonstrates that LAGBs are still effective in scattering charge carriers and reducing mobility.

In order to further confirm the reduced mobility in GB and the thermal activated behavior of $\mu(T)$ in HAGB are caused by the scattering of charged defects inside the grain or at the GBs. We need to exclude the possible scattering that comes from the ionized impurity scattering inside the grain.

Both ionized impurity scattering and GB scattering originate from the Coulomb force that exists between electrons and charged defects. The ionized impurity scattering, in general, characterizes the homogeneous scattering event within the doped grain. In contrast, the scattering event generated by the aggregation of charged defects producing a layer of space charge is attributed to GB scattering. If ionized impurity scattering dominates, the carrier mobility of the single-grain sample should also be affected and exhibit a temperature dependence of $T^{1.5}$ due to the increased mean electron velocity with increasing temperature, which weakens the change in momentum via the Coulomb interaction. [115] The linear decrease in mobility of the single grain sample in Figure 69(a) is however not consistent with the temperature power factor presented ionized impurities scattering. Thus, the influence of ionized impurity scattering can be ruled out, despite the presence of dopants within the grain interior. This is also a result of the strong dielectric screening caused by the metavalent bonding of PbTe within the grain. This conclusion can be justified as a result of the high value of the static dielectric constant ε_{st}, which is directly related to the MVB of PbTe.

As Figure 69(b) depicts, the change in carrier concentration n(T) with temperature is similar across different misorientation angles. The carrier concentration slightly decreases and then slightly increases as the temperature rises. These results demonstrate that the carrier concentration is insensitive to the misorientation angle. The full ionization of PbTe results in a high carrier concentration of $1.0 \sim 2.0 \times 10^{18} cm^{-3}$ at 25 K. [38] This non-monotonic trend is attributed to the increasing difference between the conduction band and Ag doping level with rising temperature, as well as the dynamic doping effect at high temperatures. [114, 36] For a single grain sample, its carrier concentration is similar to that of GB samples, indicating that the presence of GBs does not significantly affect carrier concentration. Moreover, the carrier concentration of the largest GB (54°) is slightly higher than that of the smallest GB (3.5°), which aligns with the fact that the measured Ag composition is higher in HAGB than the one in LAGB from APT measurements.

The strength of the GBs scattering effect on misorientation angle is further confirmed by the electrical conductivity, as shown in Figure 69(c). The electrical conductivity of the LAGB sample is higher than that of the HAGB sample at low temperatures. The conductivity

trends is similar to those of mobility, reinforcing the importance of misorientation angle on the GB scattering.

5.5.2 *Charge carrier scattering mechanism analysis*

5.5.2.1 *Extraction of GB barrier height*

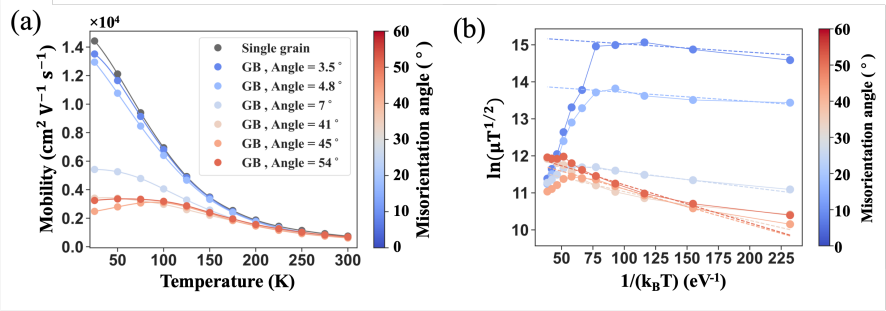

Figure 70: (a) Temperature dependence of mobilities at different misorientation angle; (b) the $\ln(\mu T^{1/2})) - (1/k_B T)$ plot for different individual GB devices.

Assuming that the scattering of GBs and phonons are uncorrelated, the measured carrier mobility will follow the following relationship:

$$\mu^{-1} = \mu_{grain}^{-1} + \mu_{GB}^{-1} \tag{62}$$

Here, "grain" refers to a single grain, where acoustic and optical phonon scattering occur, and "GB" represents the GB region. [123] The acoustic and polar optical phonon scattering dominate inside the grain, while the GB region is dominated by GB scattering. [141, 117] In this way, we eliminate the contribution of all other scattering mechanisms present in the single grain sample, isolating the mobility caused solely by the GB. Then, the trapping state model is applied to study GB scattering-dominated mobility using the following equation:

$$\mu_{GB} = Le \left(\frac{1}{2\pi m^* k_B T} \right)^{\frac{1}{2}} \exp\left(\frac{-E_b}{k_B T} \right) \tag{63}$$

The equation 63 incorporates the grain size L, electron charge e, effective mass of charge carriers m^*, Boltzmann constant k_B, temperature T, and potential barrier height E_b. [64] In the specimen design employed in this study for PPMS measurements, the grain size L for all lamellar samples is the same and equal to half the distance between two voltage electrodes (2 μm). Consequently, the potential barrier height becomes the only factor affecting GB mobility in this equation. Then, we take the logarithm of both sides of equation 63, and the equation becomes:

$$\ln(\mu_{GB} T^{\frac{1}{2}}) = \frac{-E_b}{k_B T} + constant \tag{64}$$

Based on equation 64, the $\ln(\mu_{GB} T^{\frac{1}{2}})$ versus $\frac{1}{k_B T}$ plot is created, and the negative slope of this plot represents the potential barrier height,

as illustrated in Figure 70(b). The bar plot in Figure 73(a) shows the extracted potential barriers E_b for different misorientation angles. As the misorientation angle increases from 3.5° to 54°, E_b rapidly rises from 2.5 meV to 10.1 meV. Specifically, the barrier height of the largest HAGB, whose misorientation angle is 54°, is nearly five times larger than the E_b of the smallest angle (3.5°).

The potential barrier height E_b is determined through the relationship:

$$E_b = \frac{e^2 Q_t^2}{8 N \varepsilon_{st}} \tag{65}$$

in which e is the carrier charge, N is the concentration of ionized impurity atoms (dopant concentration), Q_t is the trapping state density at the GB, and ε_{st} is the static dielectric permittivity.

5.5.2.2 *Key factors affecting GB scattering*

The next question we need to analyze is the key factors that cause the difference in the potential barriers as a function of misorientation angle between two grains. Equation 65 has pointed out that the GB scattering in TE materials is determined by three key factors: carrier concentration N, the static dielectric constant ε_{st} and trapping states density Q_t. [54]

The first factor is the concentration of ionized impurity atoms N (usually dopant atoms). The concentration of dopants is the same for all the micro-scale specimens in this work because they were lifted out from the same bulk sample. APT results also show a similar composition of Ag in the matrix for both LAGB and HAGB samples. Assuming that the N value corresponds to the measured Hall carrier concentration (Figure 69(c)), the carrier concentration with various GB angles is similar. In this work, Ag was chosen as the dopant because it has been widely used in TEs, and it can often decorate GBs, which is important for the visualization of different GB features in the APT results. The content of Ag should be low (PbTe-0.005 Ag) to avoid the formation of complex structural defects and second-phase precipitates at GBs. [36]

The next factor is the trapping state density Q_t, which is a measure of the number of charge carriers trapped at the GB. It is not easy to measure Q_t, but it can be inferred from the APT measurement results, and it will be discussed in detail with APT analysis in the next section.

The last parameter, the static dielectric constant ε_{st}, is a physical property that is defined as the ratio of an electric field within a material to the related electric displacement. It can be computed using first-principles calculations. PbTe is a typical metavalent-bonded (MVB) material, which is characterized by a high optical dielectric constant ε_∞ and large Born effective mass m^*. [92] According to the Lyddane-Sachs-Teller-Relation (Equation 72), a large static dielectric constant is obtained as a consequence in MVB compounds. The static dielectric constant of PbTe is about 380, which is much higher than that of conventional semiconductors. [68] The high dielectric constant in PbTe

results in the strong dielectric screening effect. This strong screening effect explains the high carrier mobility and the absence of the ionized impurity scattering PbTe in Ag-doped PbTe single crystal. As the GB's misorientation angle gets larger, more distortions and defects will be introduced at the GB region. This structural change will lead to a transition in chemical bonding at the GB region, which will affect the dielectric constant at the GB region. If the dielectric constant at the GB region is smaller than that of the grain region, the reduced Coulomb screening will let the moving carriers be more hindered by the space charge area in the GB region, resulting in reduced mobility or conductivity. It is consistent with the strong strength of GB scattering in HAGB samples observed in this study. Alternatively, as the dielectric constant occupies the denominator place in the equation 65, a greater dielectric constant will lead to a smaller value of E_b. [68]

5.5.3 *APT measurement*

In order to explain the intriguing differences in electrical peropeties with varying misorientation angles at GBs, both HAGB and LAGB samples were investigated using APT. This advanced technique offers a comprehensive material analysis, providing detailed information on the sample's composition, atomic structure, and bond-breaking behaviors.

As shown in the 3D atom structure reconstruction of LAGB (right side) and HAGB (left side) in Figure 71(a) and (c), the distribution of Pb, Te, and Ag atoms, with Ag atoms highlighted in red, indicates their differing distribution between low-angle and high-angle GBs. In HAGB, most Ag atoms accumulation covers the GB plane, depicted by the iso-composition surface with over 10 at% Ag, which is determined by the composition profile (Figure 71(c)). On the contrary, LAGB possesses the atomic structure with a dislocation array, as revealed by its atomic structure in Figure 71(a) and (b). In Figure 71(b), Ag atoms only decorate the dislocation cores in the GB plane. The average Ag composition within this LAGB plane can reach about 5 at%, as revealed by the 1D composition profile across the GB. Additionally, the APT analysis reveals that the Ag concentration at the GBs does not reach the values required to form Ag_2Te or Ag metal. Therefore, it is evident that no second phase of these compounds has formed, and their potential role in charge carrier scattering can be disregarded.

A striking difference in the composition of Ag ions has been observed between HAGB and LAGB, the APT measurement can also reflect the chemical bond transition at the GB regions by different bond-breaking behavior. Since PbTe is a typical metavalent-based material with extraordinary TE performance, a high value of the probability for multiple events(PME) is one of the fingerprints. Zhu et al. claim that the PME value of materials with metavalent bonding (MVB) is greater than 60%. [10] PbTe's MVB nature, shown in prior research, is confirmed by the high PME value (60%) of the matrix. [92]

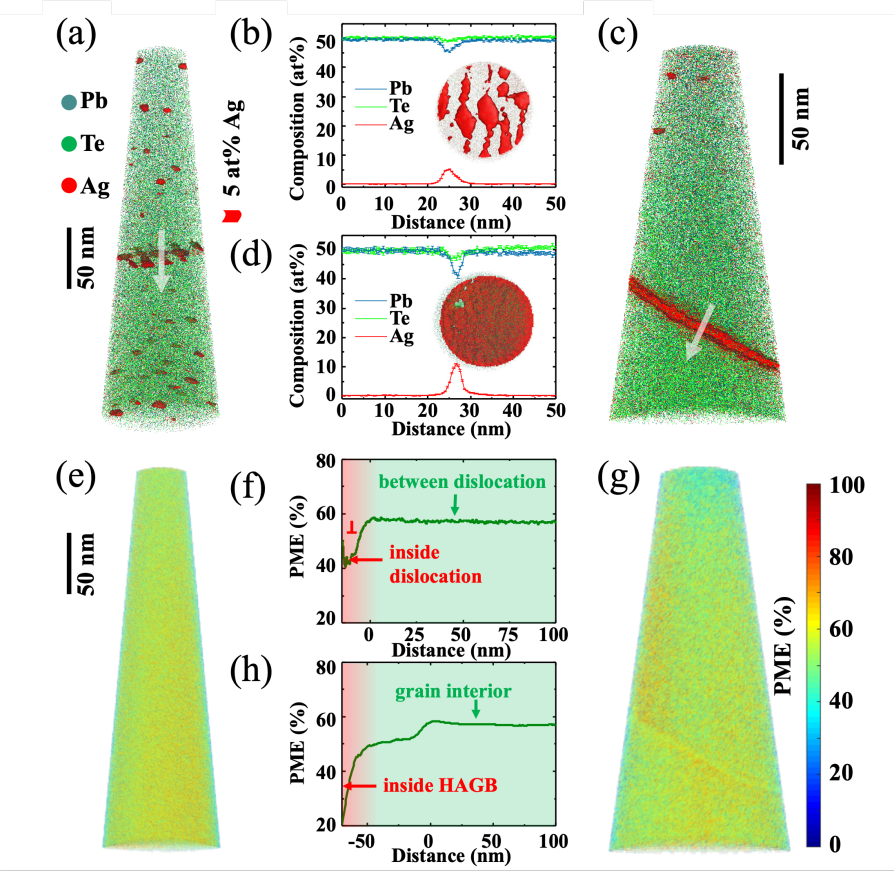

Figure 71: Atom probe tomography of two tip specimens across the LAGB and HAGB of Ag doped PbTe. (a) and (e) 3D atomic reconstruction map (left side) and corresponding probability for multiple events map across LAGB. (c) and (g) 3D atomic reconstruction map (right side) and corresponding probability for multiple events map across HAGB. Ag atoms are denoted in red dots while Pb and Te atoms are represented by blue and green dots. The close-up top view of the GB region of LAGB and HAGB are inserted in (b) and (d). In LAGB, Ag atoms only appear in dislocations cores in iso-concentration surfaces, while Ag atoms fully cover the iso-concentration surfaces in HAGB. (b) and (d) The 1D composition profile across LAGB and HAGB. The red curve in (b) represents the 8 at% Ag iso-concentration surfaces, implying the appearance of a low angle GB. The red curve in (d) represents the 10 at% Ag iso-concentration surfaces, implying the appearance of a high angle GB. (h) The probability of multiple events (PME) profile of HAGB clearly exhibits a variation in PME when crossing the GB region.

The software EPOSA is used to calculate the 3D PME map. [142] The PME value was calculated from the grain interior to the HAGB region, which is shown at the bottom of Figure 71(h). For the HAGB, the PME value varies from 55% to 20% when crossing from the grain region to the GB region. This abrupt shift in PME value predicts the transition of unique bond ruptures. In comparison to the LAGB with unique dislocation array as its atomic structure, the PME histogram in LAGB is calculated from grain to dislocation core in Figure 71(e) and (f). Owing to the overlap of signals from the surrounding matrix in 3D space, the 3D PME map fails to show these differences. As indiced in Figure 71(f) calculated using ionic iso-concentration surfaces, a minor dip in the PME value is observed from 40% inside the dislocation cores to 60% for surrounding matrix, suggesting that the metavalent bond is only collapsed at the dislocation core. The decreased PME variation at HAGB and the dislocation cores at LAGB directly proves the breaking of metavalent bonds within these regions. Moreover, based on previous studies of MVB materials using APT, this abrupt change in PME value reflects a change in the type and strength of chemical bonds, not the arrangement of nearby atoms. This is evidenced by the bond rupture observed between amorphous and crystalline phase-change materials.

5.5.4 *Explanation of the charge carrier scattering differences at LAGBs and HAGBs*

5.5.4.1 *Change of trapping states density at GB region*

Quantifying the trapping states density Q_t at the GB, is a challenge to measure directly. The APT measurement can provide a possible way to compare this indirect value between LAGBs and HAGBs.

As a type of interface, GBs introduce structural disorder and also produce a chemical composition discontinuity between the interface and the bulk. The concentration of solute atoms in the interface is higher than the solute in the bulk. This phenomenon is known as segregation. The difference in free energy between the interface and the bulk drives the redistribution of solute atoms. At equilibrium, segregation to the interfaces minimizes the total free energy of the system. This reduction in interfacial free energy can affect the behavior of the interface, such as impeding grain growth or decreasing the coarsening rate of the precipitates. [143, 144]

The degree of segregation of solute atoms at the GBs can be quantified by the Gibbsian interfacial excess. The Gibbsian interfacial excess of solute atoms is the excess number of atoms segregated at an internal interface per unit area of the interface. [143] It can be determined for both homophase and heterophase interfaces using APT. [144, 145] The Gibbsian interfacial excess of the solute Γ is defined as:

$$\Gamma = \frac{N_{excess}}{\eta A} \tag{66}$$

where the calculative number of atoms N_{excess} over the interfacial area A and η is the APT detection efficiency. [146] In this APT mea-

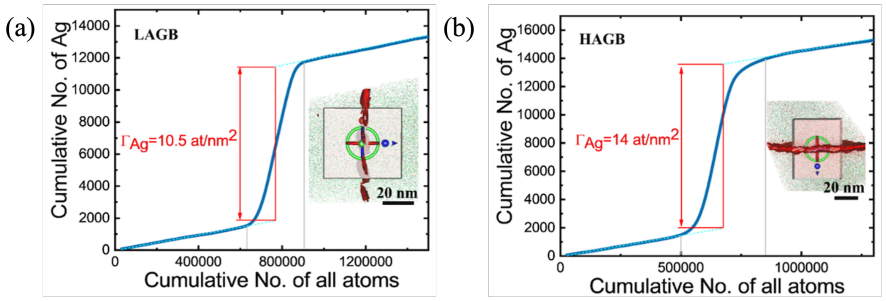

Figure 72: The calculated Gibbsian interfacial excess of Ag at the GB determined by the ladder diagram. The Gibbsian interfacial excess Γ_{Ag} at the LAGB and HAGB are 10.5 and 14.0 at/nm^2, respectively.

surement, Figures 71(b) and 71(d) demonstrate more pronounced segregation over the HAGB compared to the LAGB. To compare the segregation behavior of Ag atoms at LAGB and HAGB, the Gibbsian interfacial is calculated by the ladder diagram from the cuboid region of interest across the GBs. The APT detection efficiency is 50% for the case of LEAP 4000X Si. The interfacial area A of the selected region in the LAGB and HAGB are $40 \times 45\ nm^2$ and $40 \times 45\ nm^2$, respectively. The corresponding calculated Gibbsian interfacial excess Γ_{Ag} at the LAGB and HAGB are 10.5 and 14.0 at/nm^2.

The trapping states at GBs attract not only charge carriers, but also impurity dopants. The LM theory is used to link the segregation density of dopant atoms to the trapping states density at the GB region. According to the Langmuir-McLean theory, the adsorption of impurities at GB can be described as:

$$\frac{X_b}{X_b^0 - X_b} = \frac{X_c}{1 - X_c} \exp\left(\frac{-\Delta G}{RT}\right) \tag{67}$$

where X_b is the fraction of actual sites covered with segregated atoms, X_b^0 is the fraction of sites available for segregation, X_c is the bulk solute molar fraction, ΔG is the free energy of segregation per mole of solute, R is the gas constant, and T is the temperature. [147, 146] For Ag doped PbTed in this study, X_b denotes the density of segregated Ag sites, X_b^0 refers to the tranpping state density for charge carriers and Ag dopants. Taking the logarithm on both sides of the equation, we obtain:

$$\mathrm{In}\,(X_b) - \mathrm{In}\,(X_0 - X_b) = -\frac{\Delta G}{RT} + \mathrm{In}\left(\frac{X_c}{1 - X_c}\right) \tag{68}$$

Given that the bulk solute molar fraction (X_c) is constant, equation 68 can be simplified as:

$$\mathrm{In}\left(\frac{X_b}{X_0 - X_b}\right) = -\frac{\Delta G}{RT} + \text{ const} \tag{69}$$

For the minimum value of the GB free energy (ΔG),equation 69 can be further written as:

$$\mathrm{In}\left(\frac{1}{\frac{X_0 \uparrow\uparrow}{X_b \uparrow} - 1}\right) \uparrow = -\frac{\Delta G \downarrow}{RT} + \text{ const} \tag{70}$$

As ΔG becomes more negative (minimizing free energy), $-\frac{\Delta G}{RT}$ becomes more positive. To balance this, $\ln\left(\frac{1}{\frac{X_0}{X_b}-1}\right)$ must also become more positive. This implies that the logarithm term must increase as the denominator $(\frac{X_0}{X_b}-1)$ must decreases. For the denominator to decrease, $\frac{X_0}{X_b}$ needs to approach 1, but stay greater than 1. This means X_0 and X_b must be close but with X_0 slightly larger than X_b. The fraction of sites available for segregation X_0 should be much larger than the value of X_b. In this way, the segregation density and trapping states can be correlated. The degree of X_b is qualified by the GB Gibbsian excess of Ag segregation observed in the APT meassurements. Higher Ag segregation at HAGB compared to LAGB results in a higher X_b value at HAGBs. The trapping state density is slightly larger than the Ag segregation density at HAGB. Thus, the available trapping states at HAGB is higher than that at LAGB.

In summary, equation 67 demonstrates that for a GB with more trapping states available for segregated atoms at saturation (X_b^0), the fraction of actual sites covered with segregated atoms (X_b) is also larger, given that the bulk solute molar fraction (X_c) is constant and the requirement to keep the free energy of segregation per mole of solute (ΔG) minimum. Thus, we can qualitatively compare the density of trapping states in different GB structures by determining the GB Gibbsian excess. The Gibbsian excess of impurity Ag atoms (Figure 72) corresponds to roughly 1.3 ~ 1.5 times higher trapping states for the HAGB than that for the LAGB, assuming a similar ΔG value for both. This will lead to a difference in the GB barrier height by a factor of about 2, according to Equation 65. Yet, this factor alone cannot explain the observed E_b value that increases by a factor of about 4 ~ 5 from LAGBs to HAGBs.

5.5.4.2 *Change of static dielectric constant at GB Region*

The permittivity ε is a parameter that is used to describe how an electric field influences the electric displacement field within a medium, defined by the relationship:

$$\mathbf{D}(\mathbf{r}) = \varepsilon \mathbf{E}(\mathbf{r}) \tag{71}$$

where ε is the material's permittivity. The permittivity ε is considered a response of the electric charges in a given medium to an external electric field, and depends on the frequency ω of the electric filed. Thus, it becomes a complex function of $\varepsilon(\omega)$. [148] The parameter ε_{st}, which is an essential factor in determining the E_b height in equation 65, is the low frequency limit of the dielectric function $\varepsilon(\omega)$. [149]

The static dielectric constant ε_{st} in PbTe is quite large (about 380), which is about 30 times that for Si ($\varepsilon_{st} = 13$). [68] This is due to the fact that PbTe possess unique chemical bondings - metavalent bonding, which contributes to extraordinary physical properties, including a high optical dielectric constant ε_∞ and a large Born effective mass m^*. [80, 92] The weak bonding in metavalent solids leads to

soft phonons and pronounced polarizability of electrons. In particular, the valence electrons in MVB compounds such as PbTe are rather delocalized due to the large overlap between p-electrons. This causes a strong polarizability and a concomitant large ε_∞. The large value of ε_∞ is one of the fingerprints of MVB. According to the Lyddane-Sachs-Teller-Relation, [150] the ratio of both quantities in equation 72:

$$\frac{\varepsilon_{st}}{\varepsilon_\infty} = \frac{\omega_{LO}^2}{\omega_{TO}^2} \tag{72}$$

is related to ω_{LO} and ω_{TO}, the frequency of longitudinal and transverse optical phonons respectively. It is well-known that MVB compounds show a very low frequency of transverse optical modes, evidence for a near-by instability. This explains why these materials show extremely high values of ε_{st}.

The static dielectric constant ε_{st} is related to the screening ability of the material. This explains the high carrier mobility and the absence of the ionized impurity scattering in Ag-doped PbTe single crystal. Yet, a potential barrier is observed for samples including GBs, which is indicative of a reduced dielectric screening ability within the GB area. The bond rapture, indicated by ATP measurement, proves that the MVB collapses inside the dislocation cores at LAGBs and completely at HAGBs. As the misorientation angle of GBs increases, more MVBs transition to covalent bonds. This causes a decrease in the static dielectric constant, reducing the screening ability and resulting in stronger GB scattering. Furthermore, According to equation 65, E_b is inversely proportional to ε_{st}, suggesting that the value of ε_{st} will be controlled by the strength of GBS. The difference in GBS strength at HAGBs and LAGBs can be explained by both the reduced screening ability and the inverse relationship between ε_{st} and E_b.

5.5.5 *Mechanisms of the chemical bonding transition at the GB*

Figure 73 provides a possible microscopic picture of the atomic arrangement within the GB region, which is compatible with the scenario discussed above. For a perfect PbTe crystal, each atom has an octahedral coordination. Yet, the number of valence electrons in p-orbitals forming σ-bonds per atom is just three. Hence, for adjacent atoms, only half of an electron pair, i.e. in total one electron is available to form a bond. This is different from the picture of a covalent bond developed by Lewis, which involves the sharing of two electrons to form one electron pair between adjacent atoms. [151] This half-filled σ-bond is the hallmark of MVB. However, this atomic arrangement likely changes at the dislocation core, presumably leading to pronounced distortions away from a perfect octahedral coordination. This distortion is frequently denoted as a Peierls distortion, which causes a redistribution of electrons between short and long bonds. [87, 152] The short bonds will become stronger with a larger number of shared electrons, while the longer bonds evolve in the opposite direction. [75] A strong degree of Peierls distortion will drive the tran-

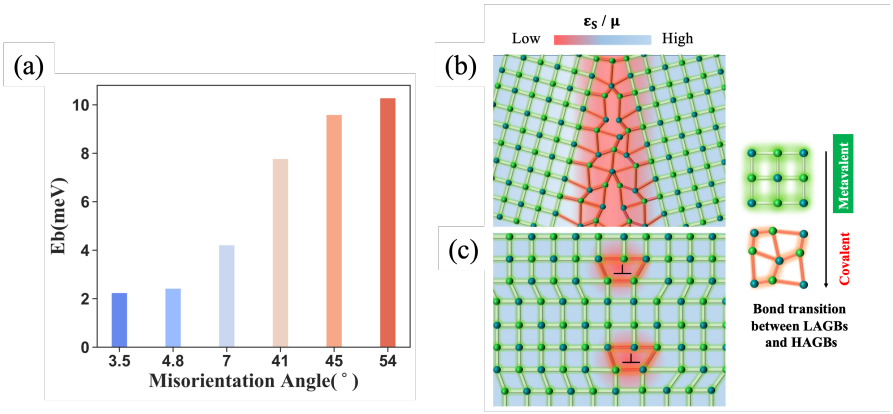

Figure 73: (a) Extracted energy barrier height at GB regions upon increasing of misorientation angles; (b) Schematic diagram of chemical bond at HAGB and (c)LAGB: Peierls distortion happens at HAGB region, HAGB are destroyed and transform to covalent bonds, while the metavalent bonds only break and transits at dislocation core position in LAGB.

sition from MVB to covalent bonding, as has been demonstrated in the material systems of GeTe-GeSe and Sb_2Te_3-Sb_2Se_3. [87]

Since atomic bonds are only modified at the dislocation core for LAGBs, the area between the dislocation cores remains almost the same configuration as the matrix, and thus, the MVB mechanism survives. Different from the LAGB, the dislocation spacing gets smaller with increasing misorientation angle, and can no longer be accommodated at the HAGB. The whole HAGB plane is distorted with a large free volume. Thereby, presumably a pronounced Peierls distortion exists in the vicinity of the HAGB, leading to the collapse of MVB (Figure 73(b)), consistent with the observed decrease of PME at the HAGB. The large degree of electron delocalization and polarization leads to the high values of ε_∞ and ε_{st}. The collapse of MVB will lead to a reduction of ε_{st} by a factor of about $2 \sim 3$, as can be seen from the sharp decrease in ε_∞ and Born effective charge upon the transition from MVB to covalent bonding. [87] This turns out to give rise to an increase in the GB barrier height from LAGBs to HAGBs. In conjunction with trapping states density at GBs, a much larger GB potential barrier height is obtained in HAGBs. This explains the observed inclining trend of E_b with increase in the misorientation angle in Figure 73(a).

5.6 CONCLUSION

In this chapter, the relationship between the strength of GB scattering and its misorientation angle in PbTe has been investigated. We combine electron backscattered diffraction (EBSD) with atom probe tomography (APT) and a physical property measurement system (PPMS). This correlative approach can decipher the impact of individual, well-characterized GBs on charge carrier scattering.

With this approach, we observe that the strength of the GB scattering decreases as the misorientation angle increases, from LAGBs to HAGBs. The GB barrier height for the scattering at HAGBs is about 4-5 times that of LAGBs. The GB potential barrier height is is determined from the distinct variations in $\mu(T)$ with different misorientation angles.

This observation is attributed to a change in the trapping state density and the nature of chemical bonds at the GB. APT measurements reveal a 1.3 times larger degree of Gibbsian excess of Ag atoms at the HAGB than that at the LAGB, indicating a larger fraction of trapping states at the HAGB. Moreover, APT also probes the drop of PME value at the whole plane of HAGB, but only within the dislocation cores of LAGB. This indicates that MVB is completely destroyed at the HAGB while only locally destroyed around dislocation cores at the LAGB. It is well-known that MVB is characterized by a high value of both static and optical dielectric constants. The collapse of MVB will reduce the dielectric constant and thus, the dielectric screening ability. As a consequence, both the larger number of trapping states and the complete breakdown of MVB at HAGBs cause strong charge carrier scattering. In contrast, the charge carriers will only be slightly scattered at the dislocation cores of LAGBs and thus, show much higher mobility. This is why GB scattering mechanism has a diminished effect on carrier transport at LAGBs.

6

ABSENCE OF ELECTRON SCATTERING AT TWIN BOUNDARY IN $Bi_2Te_{2.7}Se_{0.3}$

6.1 INTRODUCTION

GB engineering is one approach used to enhance phonon scattering. In various material systems, a high density of GBs has been introduced through the creation of nanoscale grains. Nevertheless, this approach results in structural modifications such as changes in atomic bonding, stoichiometry, and strain, leading to variations in the materials' electrical properties and band structure.[153, 154, 112]This ultimately affects the transport of charge carriers. In most cases, the carrier mobility decreases due to GB potential barrier scattering. The interaction between GBs, electrons, and phonons is complex, making it difficult to separate their effects accurately. In some materials such as Mg_3Sb_2 [44] and $SnSe$ [155], the polycrystalline sample exhibits deteriorated TE performance compared to the single crystal form, particularly at low temperatures when GB scattering dominates. This thesis has confirmed the existence of GB scattering in Ag-doped PbTe in chapter 4. Furthermore, the investigation of angle-dependent single GBs in chapter 5 revealed that high-angle GBs significantly scatter charge carriers, whereas the scattering effect of low-angle GBs is less significant.

Twin boundaries (TBs), a specific type of GB with mirror symmetry, have been shown to enhance TE performance by increasing the ratio of μ/k, as they reduce phonon scattering without significantly affecting charge carriers. [156, 157, 158] The phonon scattering by TBs has been confirmed both by theoretical calculations and experiments. [156, 157, 158] For charge carrier scattering, the twin boundary is also a coherent and low-energy interface with relatively higher stability compared with a normal GB. Thus, it was assumed that TBs have negligible effect on electron transport. However, direct experimental evidence of the absence of electron scattering at TBs is still lacking, and the mechanisms underlying this phenomenon have not been thoroughly studied.

Bi_2Te_3 alloys are highly efficient TE materials at room temperature, but their complex synthesis process poses a major limitation. Various methods such as melt spinning (MS), ball milling (BM) combined with spark plasma sintering (SPS), and hot deformation have been attempted to enhance phonon scattering by creating multiple interfaces, but this often leads to a reduction in carrier mobility, posing a challenge to achieve high ZT. These methods have also been proven to be ineffective for n-type Bi_2Te_3, particularly in the basal plane, resulting in a decline in its TE properties. [159, 32] Recently, a related study has reported that a new synthesis, which introduces LAGBs into Bi_2Te_3 alloy. This method effectively scatters phonons to reduce thermal con-

ductivity and only scattering low-energy electrons, thereby increasing the Seebeck coefficient. [160] Hence, in this chapter, we target the Bi_2Te_3 alloy as the bulk material. Remarkably, the structural characterization by SEM and EBSD has revealed the presence of twin boundaries in this sample. With the novel FIB assisted device fabrication technique, the extraction of pre-characterized TBs becomes possible.

This chapter presents a comprehensive investigation of charge carrier scattering in double parallel TBs in $Bi_2Te_{2.7}Se_{0.3}$. Firstly, we introduce the detailed fabrication process of this specific device. Polycrystalline samples with randomly distributed GBs pose challenges in pre-characterizing the target TBs and measuring transport properties of double parallel TBs. To address this, we have devised a novel method for measuring charge carrier transport across these structures. Secondly, we analyze the specialty of TB structures and study the local electrical transport of double parallel TBs. To highlight the distinct carrier scattering effect at TBs, we compare TBs with single grains and normal GB. APT measurements are used to achieve local observation of TBs. Finally, we discuss the carrier scattering at TBs.

6.2 EXPERIMENTAL DETAILS

6.2.1 *Material synthesis*

The $Bi_2Te_{2.7}Se_{0.3}$ sample was grown using a simple step-hot-pressing procedure, which resulted in a large proportion of LAGBs. Electrical characterization of the bulk sample revealed that the LAGBs effectively scattered phonons, suppressing the lattice thermal conductivity, while only minimally affecting the mobility of low-energy electrons, and enhancing the Seebeck coefficient. As a result, this n-type $Bi_2Te_{2.7}Se_{0.3}$ sample with LAGBs exhibited a high room temperature ZT of 0.94. [160]

The entire fabrication process was conducted using the FIB technology, resulting in requirements with larger crystals and clear GBs that can be observed under SEM. The grain size of the sample used in this chapter can reach up to approximately 20 µm, as demonstrated in Figure 75(a) and (b). The $Bi_2Te_{2.7}Se_{0.3}$ sample used in this study was provided by Zhejiang University.

6.2.2 *Fabrication of double parallel 60° twin boundary sample*

To investigate the impact of double parallel twin boundaries on electrical properties, the target twin GB needs to be identified using EBSD tomography with the help of a SEM. Subsequently, a Hall-bar device with twin boundaries was fabricated in the FIB. The fabrication process for the double parallel 60° GB device followed the same steps as the sample preparation discussed in the previous chapter, as depicted in Figure 65. However, the main difference was that we emphasized the characterization of the various types of GBs by EBSD. Initially,

we scanned the surface of a bulk $Bi_2Te_{2.7}Se_{0.3}$ sample to obtain the grain orientation information, as shown in Figure 75 (b). Next, we measured the misorientation angle between neighboring grains and identified the target GB with a 60° angle. To cut a small cross near the target GB as a marker, we used the unique grain shape under SEM scanning as a guide. The EBSD image of the target GB helped us find the marked GB. It is important to note that the EBSD and SEM images are mirror symmetric. Figure 74 shows the marked GB in this experiment and the "lift-out" method used to extract it. The sample fabrication and APT measurement were carried out by Shuo Jia, Yuan Yu and Riga Wu.

In this Hall-bar configuration, the double twin GB device is shown in Figure 75 (c) and (d). The device is accessible through wire bonding for electrical measurements. For an ideal Hall measurement, the length of the lamella should be three times longer than the width, and the thickness should be as thin as possible. The two horizontal contacts serve as the current ends, while the left four vertical contacts are used as the voltage end in the temperature-dependent cool-down resistance measurement. The temperature range is from 2 K to 300 K. The Hall measurement is carried out under the magnetic field from −1 T to 1 T.

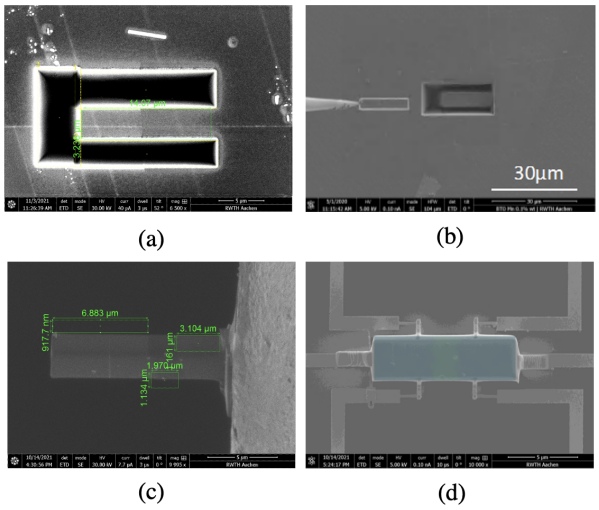

Figure 74: SEM images depicting the fabrication process of a twin GB device, including (a) a Pt marker denoting the position of TBs and three trenches cut across the TB position, (b) a lamella with TBs removed by an omni-probe, (c) the fixed lamella on a copper grid clearly indicating the presence of TBs, and (d) the transferred lamella onto gold nano-electrodes.

6.3 RESULTS AND DISCUSSION

6.3.1 *Structural analysis*

In order to further investigate the nanoscale configurations of TBs and grain interiors, SEM and EBSD scanning were performed on this

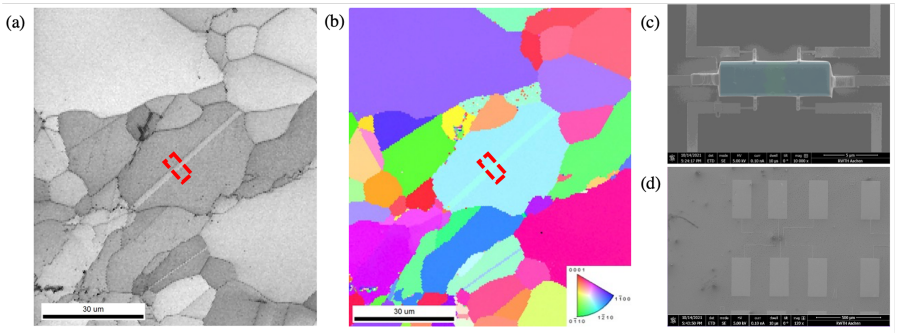

Figure 75: (a) SEM image of a polished $Bi_2Te_{2.7}Se_{0.3}$ polycrystalline bulk sample. (b) EBSD characterization of the same bulk sample. (c) Zoomed-in SEM image of a Hall bar device with a transferred double parallel TBs, shown in the middle of the whole device. (d) SEM image of the transferred device.

sample. Figure 75 (a) shows the TB location under the SEM observation. Figure 75 (b) presents the EBSD scan of the sample's region of interest, highlighting a large grain in light blue with a distinctive light green TB inside, which has a misorientation angle of 10°. The selected measurement area is outlined in a red box, crossing this stripe-shaped light green TB. Figure 75 (c) and (d) display the lamella, transferred to the electrical measurement device after sample preparation. The TB, colored in green, is located at the middle of transferred device.

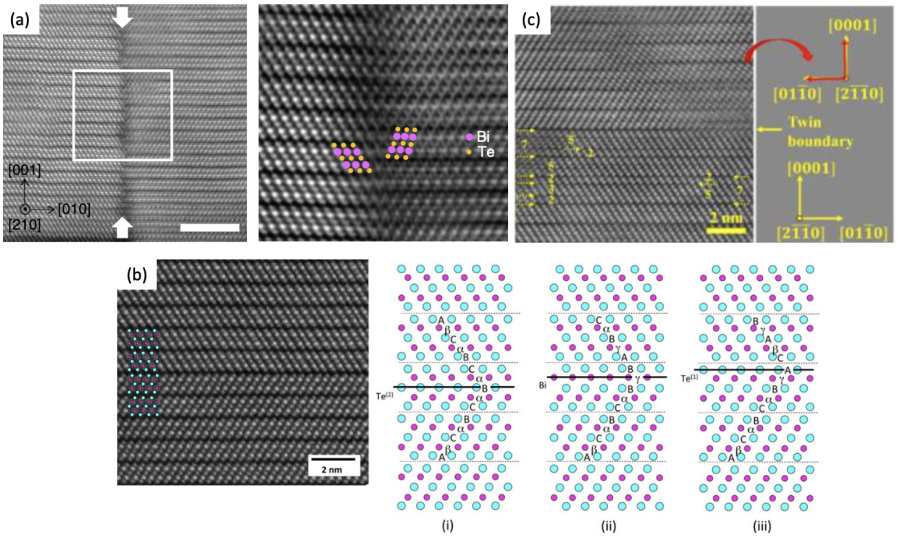

Figure 76: A comparison of the atomic structure of the TB in 2D and TE materials, showing two mirror symmetries: one perpendicular to the boundary and one along the atomic layer. (a) 2D Bi_2Te_3 [154] (b) Bi_2Te_3-based TE alloys and its three possible stacking sequences [161] (c)Bi_2Te_3 with Sb_2Te_3 alloy [112]

The atomic structure of TBs in Bi_2Te_3-based materials can be classified into two types: Type I and Type II. The atomic arrangement of TB in layered material Bi_2Te_3 in Figure 76 (a) demonstrates mirror symmetry along a direction perpendicular to the boundary, exhibiting a distinct mirror effect characteristic of Type I TBs. [154] In contrast, the TBs symmetry in Figure 76 (b) is manifested between two neighbor-

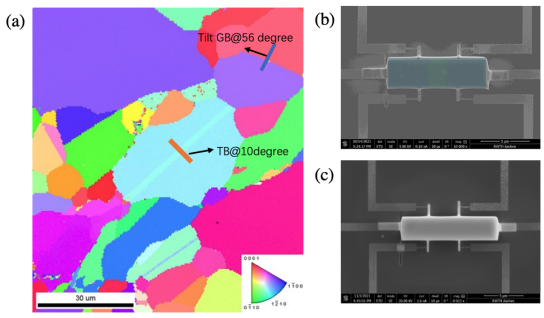

Figure 77: (a) Inverse pole figure map from EBSD measurement. The TB and tilt boundary are marked in orange and blue, respectively. (b) SEM image of the device with TB. (c) SEM image of the device with tilt boundary.

ing atomic layers, indicative of Type II TBs, signifying that the mirror symmetry at the boundary corresponds to the next layer rather than a direct reflection. [162] In TE materials, TBs are typically of Type II. The atomic configuration of the TB in Bi_2Te_3-based TE alloys has been resolved in previous HAADF-STEM investigations. The TBs region exhibit a reversal stacking sequence of the (0001) plane, which is shown in Figure 76 (b) and its three possible stacking sequences. [112] Furthermore, in $Bi_{0.5}Sb_{1.5}Te_3$, another TE material, an extra bilayer is inserted or split quintet into seven-layer structure around the TB plane, as presented in Figure 76 (c), resulting in an asymmetric structure. [161] These unique structures create superlattice-like atomic arrangements near the TB that have been found to increase carrier mobility, and decrease the lattice thermal conductivity. [163, 164] The detailed atomic structure of TB in our sample $Bi_2Te_{2.7}Se_{0.3}$ is still unknown and needs further investigation.

6.3.2 *Local electrical transport of 60° double parallel TB*

Considering the peculiar atomic structure in $Bi_2Te_{2.7}Se_{0.3}$ illustrated above, we can systematically explore the effects of double parallel TBs on the electronic properties of $Bi_2Te_{2.7}Se_{0.3}$. For electrical transport of TBs, it has been observed experimentally that mirror TBs slightly increase the measured in-plane electrical conductivity, whereas tilt boundaries slightly decrease the conductivity. [165] To compare the TBs with the tilt GB, we identified the location of double parallel TBs and tilt GBs on the surface. As indicated by the inverse polar figure map from EBSD measurement in Figure 77 (a), two lamellas are cut from the TBs region and tilt GB region respectively to fabricate two devices. The device with different GB types in Figure 77 (b) and (c) are measured in the Dynacool to explore their electrical properties.

The experiments reveal that TBs exhibit significantly different transport properties when compared to 56° tilt GBs. As illustrated in Figure 78, the electrical transport properties are represented, with the TB shown by a green line and the tilt boundary by a blue line. Additionally, a grain device without boundaries was tested for comparison

with the boundary-containing devices. Figure 78(a) indicates the locations of the TB, tilt HAGB, and single grain extracted from the bulk raw material.

The carrier concentration of the TB sample is slightly higher than that of the tilt boundary sample, with both roughly at 1×10^{19} $\frac{1}{cm^3}$, as shown in Figure 78(b). The carrier concentration of the grain sample is 1.5 times higher than that of the two GB samples, consistent with the atom probe tomography results. The presence of slight Te deficiency and Bi enrichment at the twin boundary suggests a lower interfacial energy, allowing carriers to pass through more freely, resulting in higher mobility in the TB sample.

In Figure 78 (c), the mobility trends of the three samples are initially similar, following a $T^{-1.5}$ power law, indicative of acoustic phonon scattering being dominant at higher temperatures. However, as the temperature drops below 150 K, notable differences emerge. The mobility of the TB sample increases sharply compared with the tilt boundary sample, yet remains comparable to the grain sample. At 5 K, the mobility of the TB sample, reaching approximately 2×10^3 $\frac{cm^2}{Vs}$, is almost twice higher than that of the tilt GB sample with a value of slightly above 1×10^3 $\frac{cm^2}{Vs}$. This suggests that at lower temperatures, the TB experiences substantially less GB scattering than the tilt boundary, highlighting its distinctive transport properties in these two types of boundary.

The conductivity of the TB sample is higher than that of the tilt boundary sample in the whole temperature range, as shown in Figure 78 (d). This higher conductivity is due to the TB allowing charge carriers to move more freely, which suggests that TBs do not block or interrupt the flow of these carriers. It's important to point out that the TB sample has two TBs, while the tilt boundary sample has only one GB. This difference highlights the non-blocking nature of TBs for charge carriers. This is in line with the findings in previous studies. In copper sulfide compounds, a high density of TBs has been shown to enhance electrical conductivity and improve overall electrical properties.[157] Similarly, in $Bi_{0.5}Sb_{1.5}Te_3$ and Cu-Ni alloys, TBs have been found to selectively scatter lower-energy carriers, optimizing material performance. [112, 166] This suggests that designing materials with TBs could be key to improving TE materials' performance.

6.3.3 *Micro-structure of TB via APT*

To explore the microstructure of this TB, an APT tip was made from the same TB in the bulk. The atomic distributions (Se, Bi and Te) of a reconstructed tip from 3D APT measurement is illustrated in Figure 79. The TKD assisted in the fabrication of the tip, and the corresponding TKD maps are shown in Figure 79 (a). The misorientation angle analysis shows that this tip contains a TB with a characteristic of 59.8°. It confirms that the tip is from the same TB, which has been measured by Dynacool. From the atomic distributions of Te, Bi and Se in Figure 79 (b), a high concentration of Te element is observed within the APT

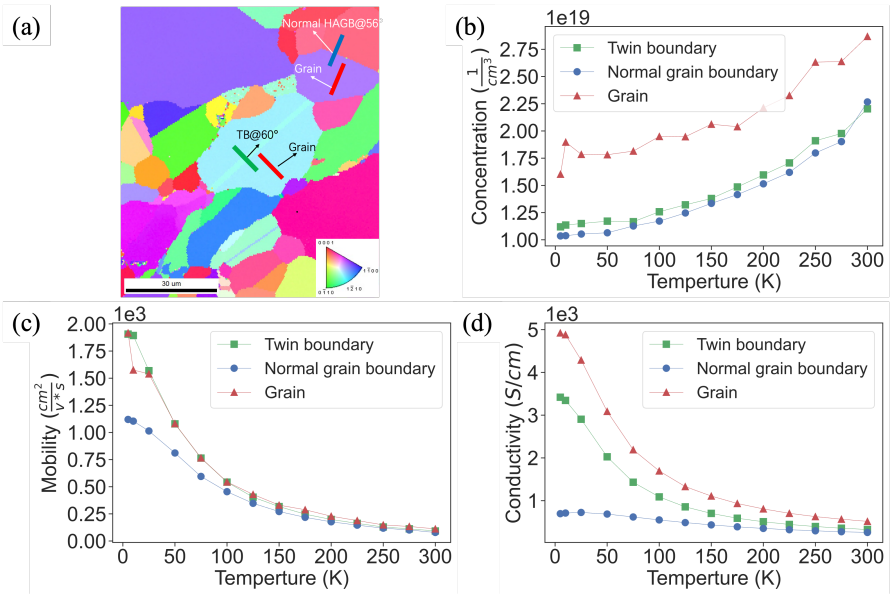

Figure 78: (a) EBSD image indicating the specific locations in the bulk material from where the twin, tilt, and single grain samples were extracted; (b) Charge carrier concentration across twin, tilt GBs and single grain samples as a function of temperature; (c) Temperature-dependent charge carrier mobility, with TBs and grain sample displaying similar higher values than one with tilt boundary; (d) Conductivity versus temperature for both GB types, with TBs exhibiting enhanced conductivity than tilt boundary.

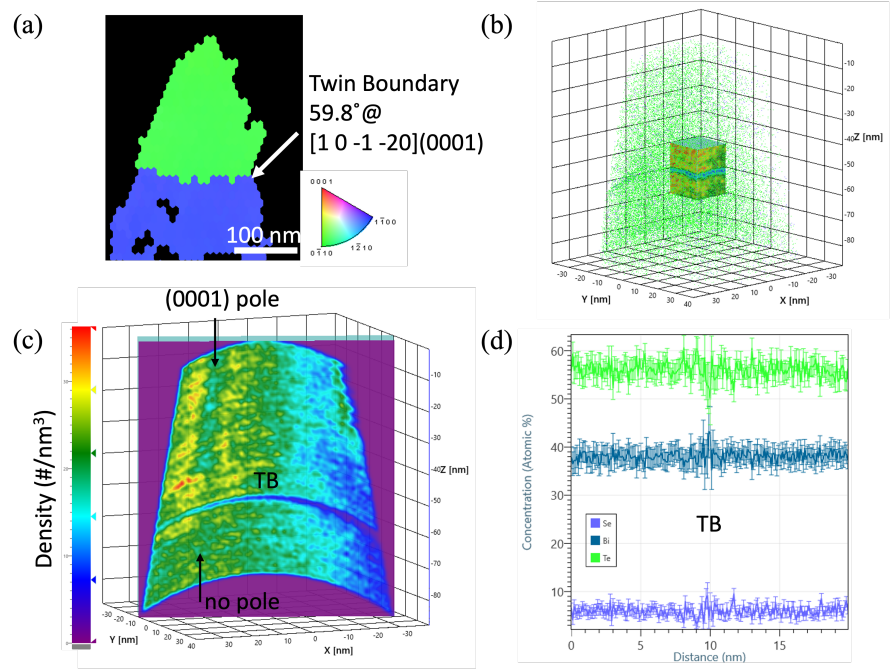

Figure 79: APT result of a TB sample: (a) TKD map of the tip with a TB (b) atomic distribution (Te, Bi and Se) within this 3D reconstructed tip (c) atomic density (atoms/nm^3) measured throughout the APT tip (d) composition profile at TB region

tip. The Gibbsian interfacial excess map thoughout the TB is obtained as in Figure 79 (c). All atoms density at per volume at TB is quite low. The composition profile of Bi, Se, Te elements at the TB region in Figure 79 (c) indicates a nearly homogeneous distribution. In the TB region, slight variations are found, with Te density decreasing from 56 to 44 atomic %, while Bi density increases from 38 to 46 atomic %, indicating a minor Te depletion or Bi enrichment. Therefore, no local solute decoration, ion segregation or secondary phase precipitate is formed along the interface, which would not significantly influence the carrier transport. It can be inferred that the TB has a low interfacial energy, which is consistent with the high mobility and conductivity observed in the electrical transport measurements.

6.3.4 *Discussion of twin grain boundary scattering*

In this study, both a temperature-dependent mobility and a conductivity decrease with increasing temperature are found in both samples, but the TB exhibits a higher conductivity and mobility than the tilt boundary. This indicates a weaker GB scattering at TBs. This electrical transport has proven that the charge carriers suffer very weak scattering, even no scattering effect at TB in $Bi_2Te_{2.7}Se_{0.3}$. The GBs not only scatter charge carriers, but also scatter phonons. The same case also happens at TBs. The Debye temperature θ_D of pristine Bi_2Te_3 is known to be 145 K. [167] At sufficiently high enough temperatures (close to θ_D), the phonon-phonon scattering dominates due to the Umklapp processes. It predicts that lattice thermal conductivity will exhibit a function of (1/T) versus temperature. [159] In this way, the increased thermal conductivity will enhance the ZT value in advance. At room temperature, the mean free path of the electrons is typically of the order of several nanometers, while for phonons, it is approximately 2.4 μm. The impact of GBs in materials with lager grains sizes is assumed to have a stronger influence on the phonons than on the electrons. Due to the low electron scattering investigated here at TBs and the hypothesized phonon scattering, we can assume that TB in $Bi_2Te_{2.7}Se_{0.3}$ improves the TE properties compared to tilt GB.

To explain the increased carrier passing though TB, we can consider the coherent feature and microstructure of TBs. Generally, interfaces at GBs are highly distorted, which would scatter a wide spectrum of carriers. The carrier scattering at high and low angle GBs in PbTe have been studied in the last two chapter. Due to the misfit of two neighboring grains in atomic structure and the bond transition at GBs, the potential barrier at the GBs region varies with different orientation angles. A larger misorientation angle between two adjacent grains corresponds to a higher potential barrier, resulting in decreased mobility. However, due to coherent feature of the TBs, most of the high-energy carriers will be unaffected by TBs, which enables the samples with TBs to maintain a good electrical conductivity. This is also consistent with the higher conductivity and mobility of TB sample than

the tilt GB sample in Figure 78. In this case, TBs act as an energy barrier to scatter the very low-energy carriers, enhancing the Seebeck coefficient. The height of the potential barrier plays a decisive role in the scattering mechanism. In order to effectively filter out the low-energy carriers, the height of potential barrier should not be too high. The non-coherent interfaces could severely distort the lattice periodic potential that leads to an unfavorably high potential barrier.

Regarding the microstructure of TBs, the mirror symmetry in one reason induce a high mobility or conductivity. The other possible reason is the superlattice-like atomic structure of Bi_2Te_3 alloy observed in the transmission electron microscopes(TEM). [112] For heterointerfaces in $Bi_2Te_{2.7}Se_{0.3}\backslash Bi_2S_3$, it is also reported that the barrier-filtering effect may occur at the heterointerfaces in $Bi_2Te_{2.7}Se_{0.3}\backslash Bi_2S_3$, which could filter the low-energy carriers to enhance the Seebeck coefficient, while the heterointerfaces do not obviously influence electrical conductivity of materials. [40] TEM measurements have to be done to further confirm the microstructure of TB in our sample. Due to the limitation of small diameter ($< 20\ nm$) of the APT tip, the APT result can only reflect a small portion of TB interface.

Also, we can consider the microstructure of TB from the perspective of interfacial excess at GBs. At the interface, the ion segregation can correlate to the interfacial excess. The APT measurement in the TB specimen reveals that no accumulation or depletion of charge carriers. The TB possesses a low interracial energy. This could be the reason that no potential barrier is formed at the TB, as discussed previously. Thus, the interfacial energy is low at TBs.

First-principles calculations on TBs show that the interaction distance at the TB in Bi_2Te_3 creates occupied states within the intrinsic band gap, generating carriers and enlarging the density-of-states near the conduction band minimum. [154] The corresponding calculation in the sample in this study would be required to explain the absence of charge carrier scattering at the TBs.

We have done other work about TBs, which might help to explain our observation. The infrared s-SNOM has attempted to characterize the TB and to explain the carrier concentration fluctuation and phonon scattering at the TBs. Our hypothesis suggests that we should observe carrier concentration fluctuations at normal GBs, but not at TBs. Previous studies of GBs in $SrTiO_2$ using SNOM have characterized electronic properties at the GBs. [168] If we do observe a difference in carrier concentration fluctuations between normal GBs and TBs, we will carry out APT to determine the local changes in stoichiometry. However, we have encountered a challenge in that the SNOM measurement. The measurement results cannot detect the location of TBs in our sample. This may be due to the lower carrier density of the Bi_2Te_3 alloy.

6.4 CONCLUSION

This chapter reports the discovery of two parallel TBs with 60° in $Bi_2Te_{2.7}Se_{0.3}$ using FIB assisted nano-device fabrication. A device was fabricated with the parallel TBs to measure its electrical transport. To investigate the impact of the TBs, a comparison was made between the TB and the normal tilt GB samples, as well as between the TB and its neighboring samples. The electrical transport measurements revealed an enhancement of mobility and conductivity caused by the existence of the two parallel TBs. The coherent feature and composition distribution at the TB, as determined by APT measurements, helps to explain why the TB did not scatter carriers in $Bi_2Te_{2.7}Se_{0.3}$. Further theoretical calculations are necessary to confirm these findings. These results have important implications for the design of Bi_2Te_3-based TE materials for low-temperature applications ($<$ 200 °C).

7

PRECIPITATES IN DOPED TE

7.1 INTRODUCTION

Tellurium (Te), an elemental TE material, demonstrates outstanding TE performance within the mid-temperature range (from 300 to 700 K). This performance is attributed to the strategic enhancement of power factors through a purely electronic effect, leveraging Te's distinctive characteristic of inherently nested valence bands. Its valence band nested structure at the H point in the Brillouin zone provides multiple conducting channels, as depicted in Figure 80(a) and (b). [169, 33, 170] Moreover, Te's trigonal structure (Figure 80(c)) is characterized by strong intrachain covalent bonding and weak interchain van der Waals bonding. [171] This quasi-1D crystal lattice of Te along the c-direction results in anisotropic behavior that can impact heat transport, as highlighted by Lin et al. [169, 172] Due to its large atomic mass and complex crystal structure, it exhibits lower lattice thermal conductivity than group IV and III-V semiconductors. Now, the ZT value of Te can reach 1.0 at 600 K, which is a significant improvement by doping. [173]

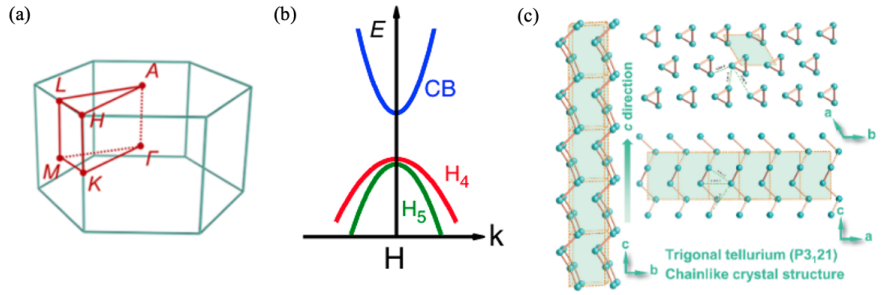

Figure 80: (a) Brillouin zone highlighting high symmetry points; [33] (b) Valence bands (H4 and H5) with inherent nesting in tellurium; [174] (c) Crystal structure of trigonal Te viewed from top and side, showcasing the unique chain arrangement along the c-axis. Yellow solid lines represent intrachain Te-Te bonding lengths, while blue dashed lines depict interchain Te-Te bonding lengths. [175]

Doping is a critical technique for fine-tuning the key electrical parameters of semiconductors, including the valley degeneracy, carrier concentration, effective mass, deformation potential, and band gap. [18] The low charge carrier concentration of pristine Te ($1 \times 10^{17} cm^{-3}$) is the main reason for its poor TE performance. Increasing the carrier concentration is crucial for improving ZT, and it has been found that doping with arsenic (As), antimony (Sb), and bismuth (Bi) effectively increases the ZT values of Te, even when co-doped with other elements. [169, 176, 33, 172] As reported, As, Sb, and Bi are effective dopants for optimizing the carrier concentration of Te. Lin et al.

[175] found that As-doping is the most effective method to increase the carrier concentration and achieve high ZT at high temperatures, while Yang et al. [177] demonstrated that even trace amounts of As can adjust carrier concentration over a broad range($7.0 \times 10^{17} - 2.7 \times 10^{19} cm^{-3}$). However, since As is toxic, eco-friendly alternatives are being investigated. Sb has been found to be a promising eco-friendly dopant that optimizes carrier concentration and introduces Sb_2Te_3 precipitates as efficient phonon scattering sites to decrease the lattice thermal conductivity of Te. [178] Bi dopants have also been found to enhance the power factor of Te while decreasing the lattice thermal conductivity. However, the efficient doping of elemental Te remains a significant challenge. The poor doping efficiency of Te is mainly attributed to the low solubility of most dopants in Te, as well as the formation of precipitates in doped Te, which makes it difficult to achieve the optimal concentration of dopants and sacrifice the charge transport properties. [175] The precipitates in doped Te can reduce the thermal conductivities and severely restrict carrier electrical conductivities. [175]

Despite the growing number of studies on Te doping, there has been no exhaustive investigation into the precipitates formed by doping and the mechanisms underlying their electrical properties. This thesis employed cutting-edge characterization techniques to investigate how effective dopants alter the microstructures and carrier transport of Te. It is meaningful to study the microstructures and TE properties of Te.

7.2 AIM AND HYPOTHESIS

The primary objective of this study is to investigate the impact of As, Bi, and Sb doping on Te's transport properties, aiming to enhance its energy conversion. To achieve this objective, we utilize EDS maps and APT to examine the composition and microstructure of As_2Te_3, Sb_2Te_3, and Bi_2Te_3 precipitates in the Te matrix. We also employ a site-specific "lift-out" approach with a FIB to evaluate the temperature-dependent electrical conductivity of the matrix and precipitate containing microscale samples. The study aims to distinguish the respective contributions of the Sb/Bi-doped matrix and precipitates to the transport properties of Te and provide insights into how these can be leveraged to enhance the material's TE performance.

7.3 METHOD

This study focuses on fabricating a well pre-characterized sample to evaluate the transport properties of Te and its precipitates, aiming to enhance its energy conversion. To achieve this goal, we employ a sample fabrication process similar to that of the single GB sample from the previous chapter. However, instead of using EBSD for pre-characterization, we use Energy Dispersive X-ray Spectrometry (EDX) to confirm the existence and composition of precipitates. The sample

fabrication follows the same steps: "lifting off" the lamella with pre-characterized precipitates or Te matrix, reshaping the lamella geometry, and transferring it onto nanoelectrodes on the substrate. The final step involves precisely placing the lamella at the center of a Hall-bar geometry gold nanoelectrode on a Si substrate.

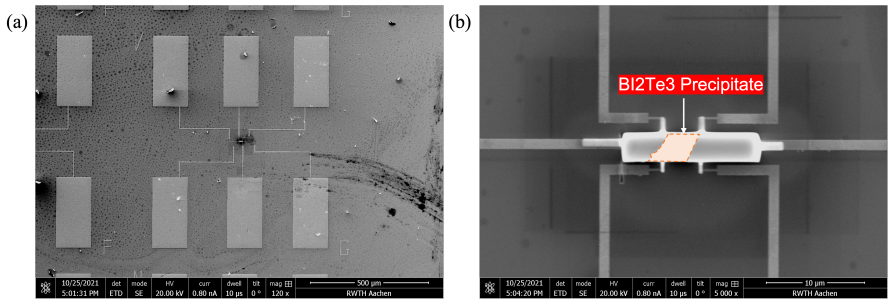

Figure 81: (a) SEM image of the final device featuring Bi_2Te_3 precipitates, and (b) a zoom in image illustrating the centered placement of the precipitates within the cut lamella.

Notably, the FIB-assisted nanodevice fabrication method employed in this study can be applied to separate the electrical properties of precipitates from the matrix. This quantitatively provides an efficient way to understand the carrier transport mechanism of the precipitate. In regular electrical transport measurements, the samples are often sputtered or grown by other deposition methods. The results only reflect the averaged contributions from the matrix and the precipitates. The novel site-specific "lift-out" assisted by FIB with custom-designed nanoelectrodes can outperform the current sample fabrication methods, which are used for electrical transport measurement. The schematic of the specific precipitate device is shown in Figure 86. The flexibility of this technique demonstrates two aspects: (i) the pre-characterization of material can easily be conducted by a dual-beam system. The dual-beam FIB system, equipped with various characterization detectors such as EBSD, EDX, and electron-beam-induced current (EBIC), offers a versatile approach to material analysis. Current research work using EBIC effectively investigates the electrical and structural properties of GBs, precipitates, and other microstructures, [179, 180] The method employed in this study facilitates a range of tests, including EBSD and EDX, offering the materials' crystalline order and composition. Moreover, this approach uniquely allows for targeted research on individual precipitates or other microstructures, enhancing the precision and depth of the material studies. (ii) The nanoelectrodes can be designed according to the size of a specific lamella. By adopting different electrode geometries and connecting them with different equipment, regular electrical transport measurements and even field-effect transistor (FET) measurements can be achieved. Equipped with the transport and thermal option (TTO) assembly, the PPMS machine can also accomplish the thermal transport measurement. The experiment in this chapter only explores the first step, which determines the temperature-dependent conductivity of the sample with a specific single precipitate. Senhao Zhang assisted

in sample fabrication and APT measurement. Riga Wu is responsible for the electrical transport measurement and data analysis.

7.4 RESULTS AND DISCUSSION

7.4.1 *Composition via EDX*

Antimony (Sb), as an effective dopant to improve the carrier concentration of Te, has been found to form Sb_2Te_3 precipitates due to Sb's low solubility in Te. [175] Similar precipitate formation led by doping occurs in other doped Te-based systems. Given these findings, the investigation in this work seeks to elucidate how dopants distribute and exist in the Te matrix. EDX measurements were performed to determine the composition of doped Te and investigate this dopant distribution.

Figure 82 demonstrates the elemental distribution in doped Te and the existence of precipitates. The precipitates are enriched with Sb, Bi, and As, while the matrices primarily comprise of Te. The EDX spectroscopic analyses were performed on the matrices and the precipitates in doped Te in order to identify their respective compositions. In the precipitate position (blue area in Figure 82(a)), the Sb-doped Te sample exhibits an increase in Sb composition from 0 at% in the matrix to 39.9 at% in the precipitate, leading to a composition ratio similar to Sb_2Te_3 precipitates. The Bi-doped Te sample reveals a Bi composition of 36.1 at% in the precipitates, as measured at the yellow area in Figure 82(b). The precipitate in the Bi-doped Te sample shows a Bi:Te ratio close to that of Bi_2Te_3. The EDX map in the As-doped Te sample shows that the precipitate contains 38.7 at% As, resulting in the formation of As_2Te_3 precipitates. In the matrix position of the three doped Te samples, all the compositions of Te matrices were observed to be 100 at%. These findings confirm the formation of precipitates due to the low solubility of dopants in Te, and no dopants are present in the matrices. Nevertheless, the limitation of resolution in EDX observation highlights the need for employing more refined analytical techniques to precisely determine the dopants' distribution in the doped Te matrix.

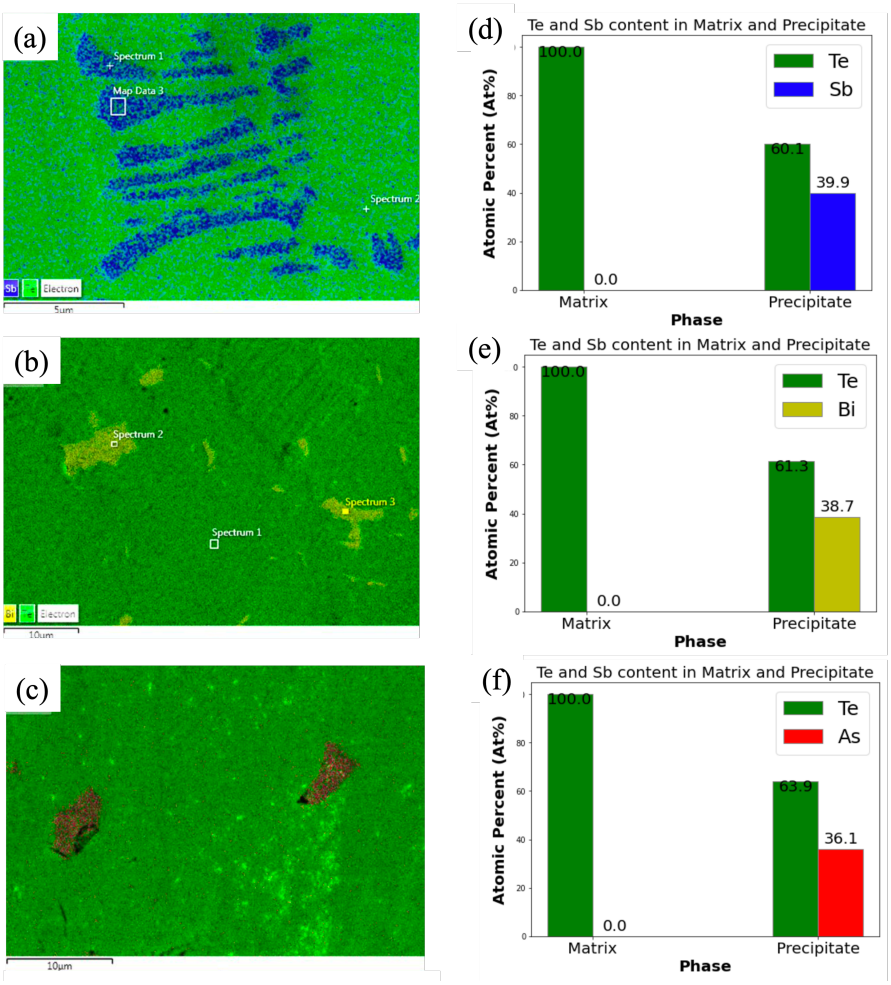

Figure 82: EDX composition map for $Te_{0.975}Sb_{0.025}$ (a), $Te_{0.99}Bi_{0.01}$ (b) and $Te_{0.98}As_{0.02}$ (c) showing the precipitates in Te with different dopants. The corresponding bar plot of the composition of the matrix and precipitates is shown in the bottom panel (d, e, f).

7.4.2 *Composition analysis of doped Te matrix via APT*

The APT was employed to conduct a more accurate composition analysis in the doped Te matrix samples. In order to obtain a high detection rate of 1%, a laser pulse rate of 200 kHz and pulse energy set between 5 and 10 pJ were used during laser-assisted APT measurement. Figure 83 (a) depicts the reconstruction of an APT specimen of the matrix of Sb-doped Te. The mass spectrum analysis reveals that the solubility of Sb in Te is extremely low, at 0.03 at.%. It is evident that less Sb is present in the Te matrix, predominantly in the form of precipitates. Figure 83 (b) illustrates the reconstructed 3D distribution of the matrix of Bi-doped Te. Similar to the results for Sb-doped Te, only a tiny fabrication of Bi (~ 0.05 at.%) is dissolved in the Te matrix. The solubility of As in Te is also low, around 0.06 at.%. Therefore, Sb, Bi, and As primarily exist as precipitates in doped Te, with only trace amounts in the matrix.

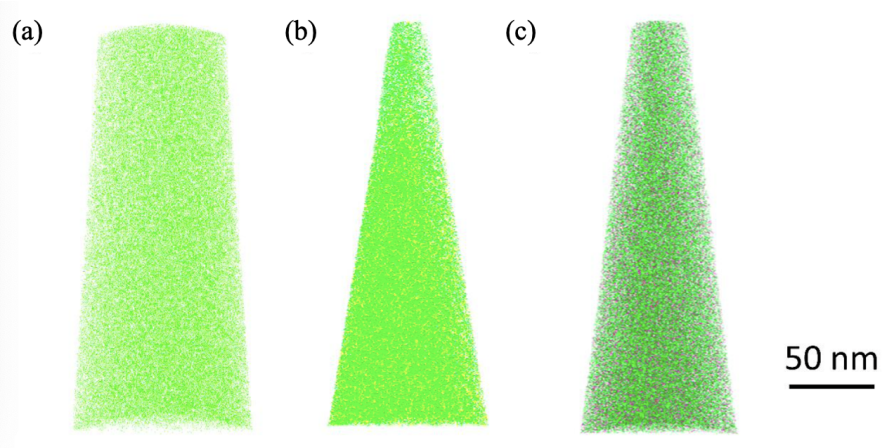

Figure 83: APT results of (a) $Te_{0.975}Sb_{0.025}$; b) $Te_{0.99}Bi_{0.01}$; and c) $Te_{0.98}As_{0.02}$.

7.4.3 *Composition analysis of doped Te precipitates and chemical bonding investigation*

The accurate examination of the precipitates was also conducted by APT. Figure 84 displays the 3D reconstruction of the volume of the sample $Te_{0.975}Sb_{0.025}$ and its corresponding PME value distribution. A blue precipitate can be observed at the top of the green needle-shaped tip. The compositions of the precipitate and the matrix correspond to Sb_2Te_3 and $TeSb_{0.0003}$, respectively. The examination on precipitates in Bi-doped Te ($Te_{0.99}Bi_{0.01}$) also certifies the existence of Bi_2Te_3 precipitate in its matrix, whose stoichiometry is $TeBi_{0.001}$.

The APT is not only used to investigate the composition and atomic structure of the precipitates, but also to reflect the chemical bond transition. Chalcogenides such as Sb_2Te_3 and Bi_2Te_3 stand out as great TE materials with unconventional chemical bonds, the metavalent bonds. [90, 42] Unconventional bond rupture, one feature of metavalent bonded materials, can be investigated by the PME value in APT

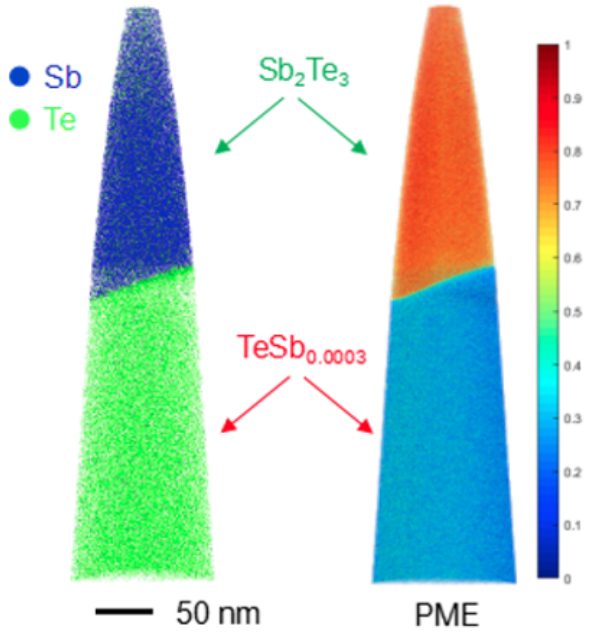

Figure 84: APT results and the probability of multiple events of $Te_{0.975}Se_{0.025}$ with precipitates Sb_2Te_3.

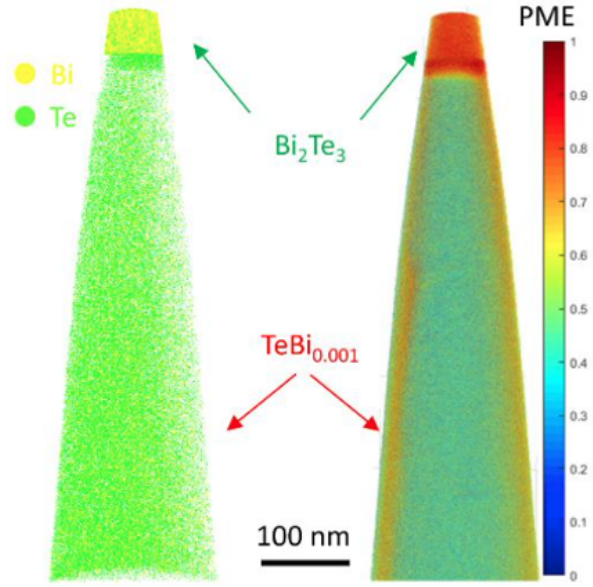

Figure 85: APT results and the probability of multiple events of $Te_{0.99}Bi_{0.01}$ with precipitates Bi_2Te_3.

measurements. When examining materials with MVB, it is frequently observed that several fragments can be detected within a single laser pulse, with a PME value exceeding 60 %. Conversely, in ionic or covalent bonded materials, the detection of more than one fragment in a single pulse is significantly less likely, with their corresponding PME value falling below 60%. The PME value becomes an essential metric to determine the chemical bond transition. [181] Following the identification of precipitates in Sb-doped Te as Sb_2Te_3, the PME value for

Sb_2Te_3 precipitate, as depicted in Figure 84, is as high as 70%. Similarly, for $Te_{0.99}Bi_{0.01}$ precipitates, the PME value is also elevated to approximately 80% in Figure 85.

The combined application of EDX and APT in this study confirms the limited solubility of Sb, Bi, and As in the Te matrix, as well as the presence of Sb_2Te_3, Bi_2Te3 and As_2Te_3 precipitates within the doped Te samples. These findings are consistent with existing literature that highlights the challenges of Te doping. Despite these challenges, doping with elements like Sb, Bi, and As significantly boosts TE performance, attributed to the optimized carrier concentration. However, the role of precipitates in the charge carrier scattering mechanism to boost the performance of Te as a TE material remains unclear.

7.4.4 *Electrical properties*

Building upon the findings presented in the previous section, where we have demonstrated the presence of precipitates in doped Te, we now turn our attention to an underexplored yet crucial aspect of precipitates' transport properties in TE material research.

Extensive research has been done until now to try to elucidate the effect of precipitates in doped Te on optimizing charge carrier concentration and enhancing TE performance. These studies on the formation of precipitates in doped Te assume that precipitates scatter phonons significantly, and reduce the lattice thermal conductivity of the material to enhance the TE performance. [175] Yet, the impact of precipitates on the charge carriers' transport of doped Te has different hypothesis and results. Some researchers prove that the formation of precipitates affects the doping to reach the optimal carrier concentration of 1×10^{19} cm^{-3}, predicted by theoretical calculation. [182] Some statements can be justified that the precipitates act as scattering centers for charge carriers to restrict the electrical conductivity significantly. This reduction in the electrical conductivity decreases the power factors, deteriorating the ZT value. [183] However, the work of Decheng et al. suggests the contrary: It was found that the precipitates improve the electrical conductivity compared with the undoped Te samples. [184, 176, 33] Therefore, more specific investigations are needed to study how precipitates affect charge carrier scattering in doped Te, highlighting a significant gap in the current understanding.

This gap presents a unique opportunity for further research, as understanding the interaction between charge carriers and precipitates could be pivotal for designing high-performance TE materials. Therefore, investigating the precipitates' role in charge carrier scattering in Te presents a key research direction, promising to yield insights that could transform our approach to optimizing TE materials.

The electrical properties of the manufactured chip are evaluated using the PPMS, which employs a Hall-bar shape device for its resistance measurements. Figure 86 offers a schematic of a single precipitate device and its electrical measurement method. The magnitude of

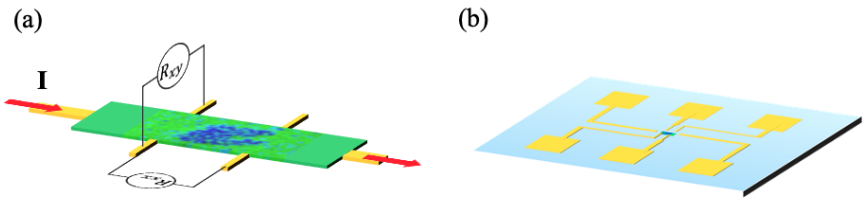

Figure 86: (a) Normal electrical conductivity measurement setup. The matrix and precipitate averages are measured; (b) single precipitate measurement obtained by FIB.

the magnetic field varies from -1 T to 1 T in Hall measurement. The temperature varies from 50 K to 300 K to obtain data on longitudinal resistance and Hall resistance. Figure 87 displays the SEM image of the fabricated sample in this experiment, successfully assembled on gold electrodes on the chip with good electrical connections. Given the sample's small size($1.5\ \mu m \times 3\ \mu m \times 12\ \mu m$), its matrix and precipitate can be evaluated individually.

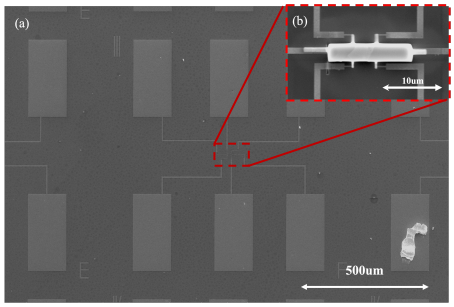

Figure 87: (a) SEM image of pre-prepared nanoelectrodes chip ; (b) SEM image of single precipitate sample acquired by focus ion beam(FIB).

Figure 88 summarizes the overall results for the electrical conductivity as a function of temperature across two types of nanostructures (precipitate and matrix) and two dopants (Bi and Sb), including the pure Te, the matrix and precipitate sample for $Te_{0.975}Sb_{0.025}$ and $Te_{0.99}Bi_{0.01}$.

Firstly, we examine the impact of two types of nanostructures, precipitate and matrix, on the electrical conductivity σ, aiming to elucidate how these structural differences influence the charge carrier electrical conductivity. Figure 88 (c) gives a pronounced variation in temperature-dependent σ led by precipitates in all Sb and Bi-doped Te samples. Despite the minimal impact of various dopants on transport properties, all the triangular lines (both red and green lines) presenting the precipitates, always remain above the dotted lines, which signifies the matrix in these two doped samples in the whole temperature range. For instance, the σ values for the precipitates in both Sb and Bi-doped Te are in the range from 500 S/m to 800 S/m, significantly exceeding the values for the matrix, which are generally centered around 100 S/m. The temperature range is from 50 K to 300 K.

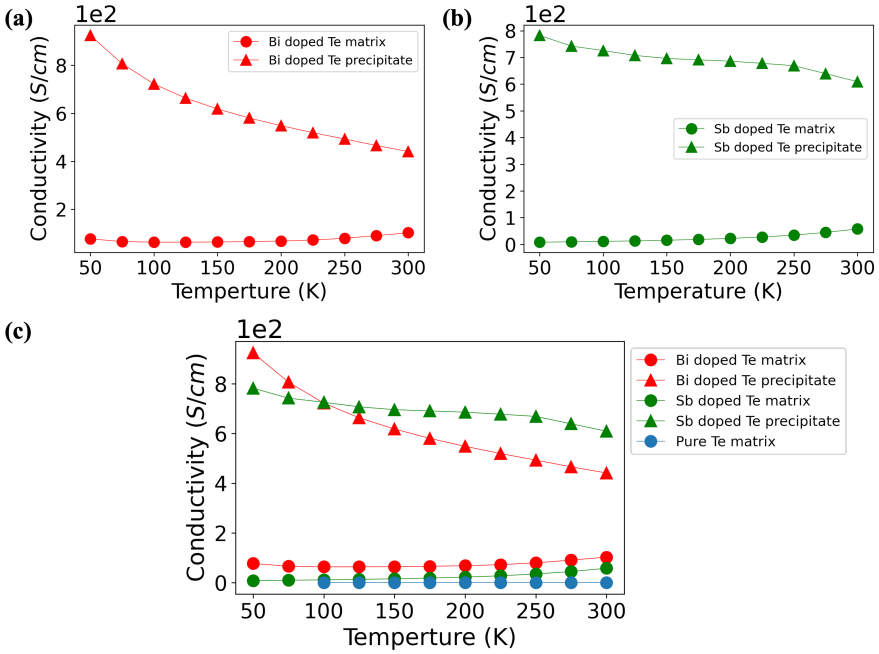

Figure 88: (a) Comparison of the conductivities as a function of temperature for matrix (red circle line) and precipitate (red triangle line) in Bi dope Te ; (b) temperature dependent conductivities for matrix (green circle line) and precipitate (green triangle line) in Sb dope Te; (c) Temperature dependent conductivity of doped Te sample.

To further confirm the precipitates' higher conductivity while controlling the effect of different dopants, we compared the precipitates and matrix samples with Bi and Sb, respectively. In Figure 88 (a), the conductivity trends of Bi-doped Te samples are depicted, with the red triangular line (precipitate) positioned higher than the red dotted line (matrix). A similar change is also seen in the Sb-doped Te samples, where the precipitate's temperature-dependent conductivity is greater than that of the matrix. These observations confirm that the precipitates have higher conductivity than the matrix. In addition, the trend of temperature-dependent σ shows a difference between precipitate and matrix. In Bi-doped Te sample, as temperature increases, the conductivity of the precipitate decreases from 900 S/m to 500 S/m (Figure 88 (a)), which is indicative of degenerate conduction for the entire measurement range. Conversely, the matrix shows a slight increase in conductivity with rising temperature, aligning with intrinsic semiconductor characteristics. This changing of temperature-dependent σ is seen clearly in Figure 89. The degenerate semiconductor behavior of precipitates and the semiconductor behavior of the matrix are also observed in the Sb doped Te samples. (Figure 88 (b))

Secondly, the impact of different dopants on electrical conductivity were investigated. For all the precipitates in Figure 88(c), the temperature dependent σ of Sb (green triangular line) is slightly higher than that of Bi doped Te (red triangular line) when $T > 100$ K. whereas an opposite temperature dependent σ are observed in the low temperature range ($50\ K < T < 100\ K$). This reflects that Sb doping improves the electrical conductivity at high temperatures. The slightly

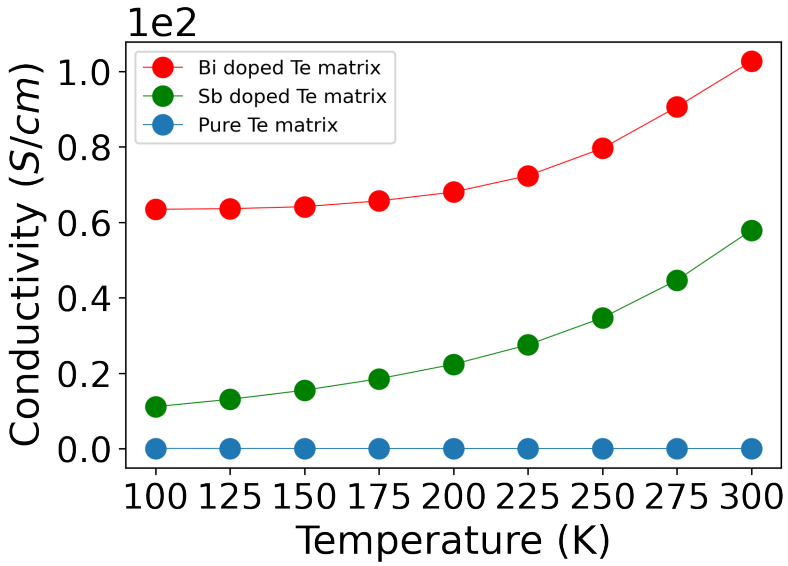

Figure 89: (a) Comparison of the conductivities as a function of temperature for doped matrix and pure Te matrix (blue dotted line). The doped matrix possess two type dopants: Bi doped Te matrix (red dotted line) and Sb doped Te matrix (green dotted line).

improved electrical conductivity of Sb-doped Te can be attributed to a higher σ in Sb_2Te_3 than in Bi_2Te_3 in the same temperature range, since the composition of the Sb_2Te_3 and Bi_2Te_3 precipitates are confirmed by the APT measurement made in this study.

For the matrix, comparisons were made between undoped and doped samples with various dopants. In Figure 89, the blue dotted line, denoted by the pure Te matrix, locates the lowest, with a conductivity below 10 S/m compared with the red and green lines for other two doped matrices. This agrees with reports that Sb and Bi doping can be used to increase the electrical conductivity of Te. [169, 176, 33, 172] Regarding different dopants, the red dotted line of $Te_{0.99}Bi_{0.01}$ matrix lie higher than the green dotted line denoted $Te_{0.975}Sb_{0.025}$ matrix. Even though both Sb and Bi are hardly dissolved in the Te matrix, more Bi content(~ 0.05 at.%) dissolves in the matrix than Sb (0.03 at.%), as shown in the APT measurement. The higher Bi content in the matrix might be the reason for the higher conductivity in the Bi doped Te matrix.

7.4.5 *Discussion*

To visualize the effect of precipitate on enhanced electrical conductivity, a bar plot in Figure 90 (a) shows the conductivities of the two dopants: Bi and Sb; and two phases: matrix and precipitate at 300 K. No matter what type of the dopants is in the Te, the precipitates' electrical conductivities are always higher than those of the matrix. The bar heights in the precipitate column are $4-6$ times taller than the ones in the matrix column. In the green color bar (Sb doped Te), the electrical conductivity of the precipitate sample is 609 S/cm, which

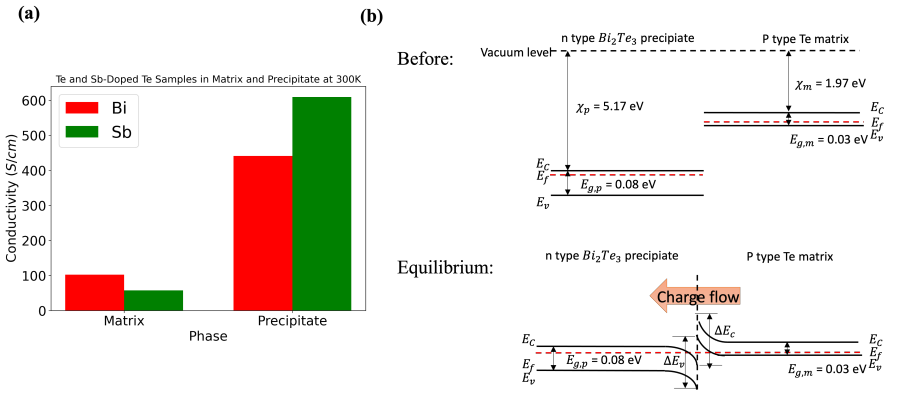

Figure 90: (a) Bar plot comparing the conductivities of two dopants across two phases. (b) Schematic diagram showing how band alignment and charge transfer enhance electrical conductivity in the precipitate.

is 6 times larger than the one of the matrix sample. In red bars (Bi-doped Te), the difference between the precipitate and matrix reduces to 4 times in height. The electrical conductivity of the precipitate sample is 441 S/cm, and that of the matrix sample is 102 S/cm. Considering different dopants, adding an Sb dopant causes a larger electrical conductivity in the precipitate form, which is also the largest value in this bar plot. Otherwise, a smaller value of electrical conductivity is obtained in the Sb-doped Te matrix. Bi-doping exhibits its advantages in the matrix phase. This is because the Sb has a lower solubility in Te than Bi. According to the APT measurement of the matrix with various dopants illustrated in the previous section, the detected Sb and Bi content in the matrix is 0.03 at.% and 0.05 at.%, respectively. The poor solubility of Sb might affect the enhancement of carrier concentration in the matrix and hence, a decrease in the electrical conductivity.

The reason for the consistently higher electrical conductivity observed in doped Te precipitates can be exemplified by the case of Bi-doped Te. Figure 90 provides a possible schematic illustration to explain the enhanced electrical conductivity of precipitates in doped Te. As to the precipitate region, our APT has already confirmed the formation Bi_2Te_3 in the precipitate. The n-type precipitate is confirmed by the negative slope in the Hall measurement. So, we can directly determine the band structure of Bi_2Te_3 from the literature. The band gap of Bi_2Te_3 is 0.08 eV, and its electron affinity is 5.17 eV. [185] Because of the n-type transport behavior, a Fermi level close to the conduction band is assumed. For the matrix, since the merely Bi doping solute in the matrix as proved by the APT measurement, we assume the band structure in the doped matrix is similar to the pure Te. The pure Te has an electron affinity of 1.97 eV and a band gap of 0.03 eV, reported by literatures. [186, 187] In view of the p-type behavior, we assure a Fermi level close to the valence band. As the Fermi level of the Te matrix is higher than that of the Bi2Te3 precipitate, the electrons tend to flow from the matrix to the precipitate region to balance the Fermi level and to yield band bending. Then, the precipitate region can be assumed as an electron acceptor. The charge carriers in

the precipitate are more than the matrix, which leads to the higher electrical conductivity of the precipitate. The whole process is similar to band alignment, and charges transfer across the interface, such as SiGe-Si and Bi_2Te_3/In_2Te_3 interface. [188, 189] The enhanced electrical conductivity is one of the main reasons for the enhanced power factor and ZT value.

7.5 CONCLUSION

This chapter illustrates a successful attempt to explore the microstructure, chemical bonding, and local electrical transport of the precipitates formed in Te by effectively doping it with Sb and Bi. According to EDX and APT characterizations, Sb, Bi, and As are not easily soluble in Te. Instead, Te precipitates are generated. This is in line with previous investigations of doped Te. By utilizing a novel sample preparation method, we have successfully accomplished temperature dependent electrical conductivity measurements of precipitates, enabling the separate study of the precipitate and matrix in doped Te. The electrical measurement demonstrates that adding Sb and Bi to the matrix as a doping method is effective in increasing their conductivities. Compared with the matrix samples, the electrical conductivities of the samples containing Bi_2Te_3 and Sb_2Te_3 precipitates are nearly two orders of magnitude larger at low temperatures and more than a factor of 10 larger at 300 K. In the doped matrices, the electrical conductivity is also slightly increased by Sb and Bi doping, although the pure Te matrix's conductivity is almost constant over the entire temperature range ($50\ K < T < 300\ K$). The increased electrical conductivity in Sb and Bi-doped Te is due to the incorporation of precipitates and not the doping of the matrix, which is explained by band alignment and charge transfer from matrix to precipitate. Therefore, Te precipitates are primarily responsible for the increase in the charge carrier transport and TE properties of doped Te. This study provides a guidance to enhance the single element TE performance.

8

CONCLUSION AND OUTLOOK

In this thesis, a series of investigations utilizing innovative FIB assisted device fabrication techniques have been conducted to study charge carrier scattering at nanostructures, including individual GBs, TBs, and precipitates in TE materials containing Ag-doped PbTe, Bi_2Te_3, and doped Te. The FIB dual-beam system is equipped with EBSD and EDX detectors capable of fabricating the lamella. It enables in situ characterization of samples in the FIB chamber, facilitating the extraction of well-characterized nanostructures into Hall-bar devices. The fabricated nanodevices are easily transferred to the PPMS system for electrical transport measurements. The APT sample can be prepared by FIB and characterized the same nanostructures' atomic arrangement and composition. Thus, this FIB-assisted device fabrication technique reveals its advantage as a correlative characterization method to determine the local microstructure, composition and transport properties of the same GB and precipitate. To this end, we can explain the impact of nanostructures' charge carrier scattering mechanism with the help of the local microstructure and composition.

In Chapter IV of the study, this is the first successful attempt to investigate individual GBs in Ag-doped PbTe using a novel FIB-assisted device fabrication technique. This study reveals a thermally activated behavior in temperature-dependent mobility and notable reductions in mobility and conductivity of the individual GBs compared to adjacent grains, confirming the charge carrier scattering at the GBs. Additionally, the precise GB resistivity is also obtained. When comparing individual GB samples with neighboring grain samples, the differences in electrical conductivity and mobility of different samples were observed. These discrepancies are attributed to the compositional heterogeneity at the GBs, as evidenced by the distinct APT results. Notably, the APT results reveal that Ag segregation at the GB can enhance electrical conductivity, while the formation of an Ag_2Te second phase markedly reduces it, acting as an additional scattering center beyond the GB scattering. Furthermore, a "one to one" correlative PPMS-APT measurement has been conducted to ensure the correlation between microstructure and transport properties at individual GBs.

In chapter V, we applied this technique to study the impact of the misorientation angle of individual GBs on charge carrier scattering. This experiment characterizes their electrical properties, composition, and atomic structure utilizing EBSD and APT in conjunction with local electrical measurement. With this approach, we have demonstrated that charge carriers are scattered more strongly at the HABGs than at the LAGBs in a TE Ag-doped PbTe compound. The GB potential barrier height is about 8-10 meV for HAGBs, while it is only 2 meV for LAGBs. APT measurements reveal a 1.3 times larger degree

of Gibbsian excess of Ag atoms at the HAGB than that at the LAGB, indicating a larger fraction of trapping states at the HAGB. Moreover, APT also probes the drop of PME value at the whole plane of HAGB, but only within the dislocation cores of LAGB. This indicates that MVB is destroyed at the HAGB, while only locally destroyed around dislocation cores at the LAGB. It is well known that MVB is characterized by a high value of both static and optical dielectric constants. The collapse of MVB will reduce the dielectric constant and thus, the dielectric screening ability. As a consequence, both the larger number of trapping states and the break-down of MVB at HAGBs cause the strong charge carrier scattering. In contrast, the charge carriers will only be slightly scattered at dislocation cores of LAGBs and thus, show much higher mobility. This work implies that LAGBs and dislocations have less effect on the charge carrier transport in metavalently bonded solids, providing insights into the materials design, including TEs and beyond.

In chapter VI, a special atomic structure of GBs - TBs, with mirror symmetry, has been examined. The two parallel TBs with 60° were found in $Bi_2Te_{2.7}Se_{0.3}$ under EBSD, and transferred onto Hall-bar device to measure its electrical transport. In order to explore the influence of two parallel TBs, a comparison between the TB and normal tilt GB samples has been conducted. The electrical transport properties show that an enhancement of mobility and conductivity are caused by the existence of two parallel TBs. The coherent feature and fewer variations in the composition distribution at TB obtained from APT measurement and further theoretical calculation are still needed in order to explain why TBs don't scatter carriers in $Bi_2Te_{2.7}Se_{0.3}$. This finding supports the study of high performance TE materials by involving TBs in the synthesis process.

The last chapter illustrates a successful attempt to explore the microstructure, chemical bonding, and local electrical transport of Te-based samples doped with Sb, Bi, and As. According to EDX and APT characterization, Sb, Bi, and As are not easily soluble in Te. Instead, telluride precipitates are generated. This is line with previous investigations in doped Te. Utilizing the novel sample preparation method, the local transport measurement of pre-characterized precipitates were accomplished to successfully separately study the precipitate and matrix in doped Te. The electrical measurement results indicates that the dramatically increased electrical conductivity is due to the incorporation of precipitates, and not the doping of the matrix, which provides a guidance to enhance the single element TE performance. To dive into the nature of chemical bonding in doped Te, the APT characterization was utilized. As determined by laser-assisted APT, high PME values for Sb_2Te_3, Bi_2Te_3 precipitates are indicative of their metavalent bonding nature. Based on the understanding of MVB-based materials in our group, compounds with MVB are recommended for the design of high performance doped Te.

This technique circumvents previous experimental limitations and offers a novel method to study individual nanostructures in bulk materials. As there is a significant number of materials utilizing MVB,

the findings on charge transport across GBs over a broad temperature range are important for various applications, including power generation (as TEs), memory (applications as phase change materials), mid-infrared lasers, and detectors. The approach devised here can be adapted to many other solids, providing a new avenue for the design of functional materials via GB engineering. We have started to apply this technique into solar cell GBs studies. The initial result has proven the portability of this technique. In the field of TE materials, the thermal conductivities and Seebeck coefficient measurements are being accomplished by specific device designs. To further explore extraordinary physical properties, this technique can be used to detect extraordinary physical properties in newly synthesized materials, such as anisotropic crystals or certain single crystals which are hard to synthesize. In this thesis, our focus was solely on fabricating Hall-bar devices for measuring the electrical properties of specific nanostructures. However, this technique has the potential to be adapted for other electrical measurements, such as field-effect transistor and tunneling measurements, with only minor modifications to the nanodevice design.

A

GDS FILES

This GDS file is a design of hall bar-like geometry electrodes for a thermoelectric grain boundary study device. The previous exposure dose was 700 $\mu C/cm^2$. In this design, the EBL writing layer is Layer 3, 5, 6, and 7, which correspond to contact pads with 150×300 µm, 1 µm wide lines, 200 nm wide lines, and 5 µm wide lines. Layers 1 and 2 don't need to be written. Layer 1 is the working field with the size of 1000×1000um. Layer 2 is the hall bar-like lamella sample for FIB.

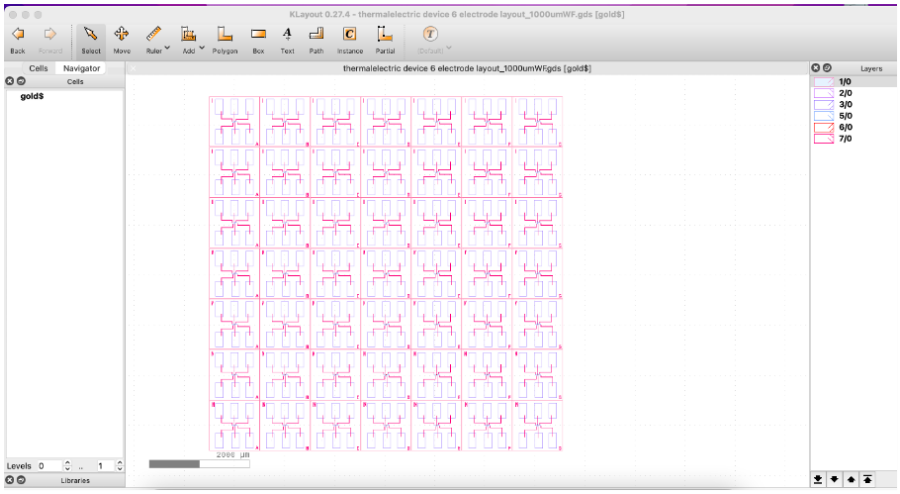

Figure 91: EBL design of electrodes array.

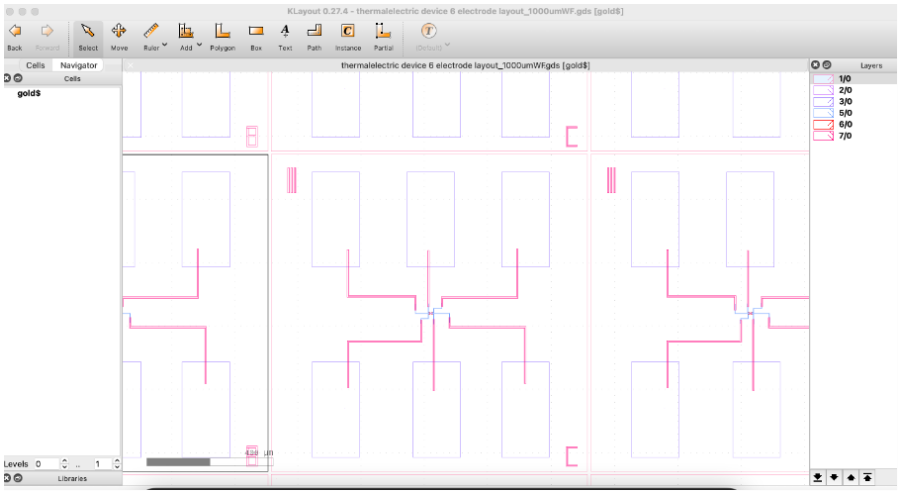

Figure 92: Zoomed-in image of hall bar-like electrodes for a thermoelectric grain boundary study device.

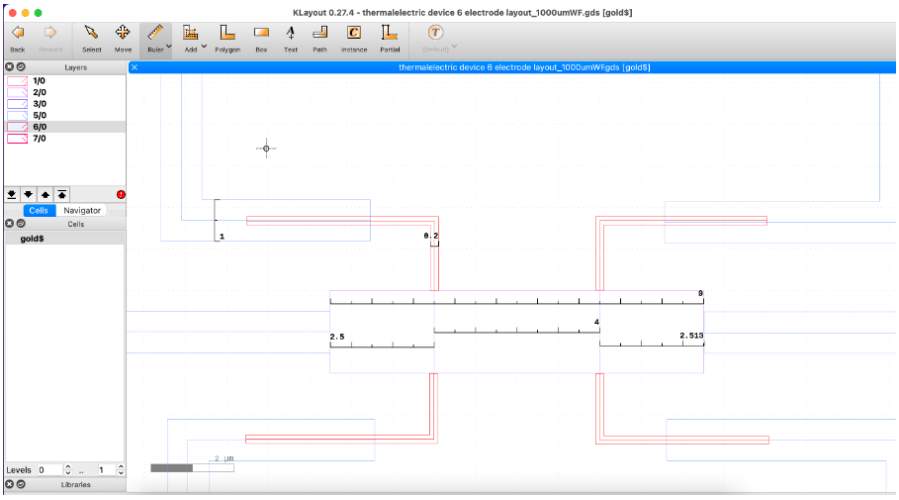

Figure 93: Zoomed-in image of the EBL design showing the smallest line connected to the contact pad.

B

DOUBLE LAYER PMMA COATING PARAMETER

Step	Process context	Equipment	Parameter
1	AZ 639.04 (50 K)		AZ 639.04 at 20 °C
2	AZ 679.02 (150K)		AZ 679.02 at 20 °C
3	Pre-baking	Hot plate	180 °C for 5 min
4	To coat the first layer PMMA AZ 639.04	Spin coater	30 s 4000 rpm
5	After baking	Hot plate	180 °C for 5 min
6	Thickness of the first layer PPMA AZ 639.04		80 nm
7	To coat the second layer PPMA AZ 679.02	Spin coater	30 s 2000 rpm
8	After baking	Hot plate	180 °C for 5 min
9	Thickness of the second layer PPMA AZ 679.02		100 nm

C

DOSE TEST

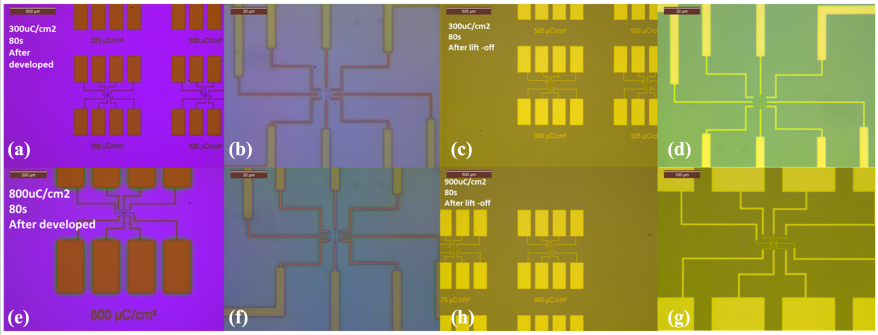

Figure 94: Dose test results in EBL with a development time of 80 s. The images in the upper row (a, b, c, d) were exposed with a dose of 300 $\mu C/cm^2$, while those in the lower row (e, f, g, h) were exposed with 900 $\mu C/cm^2$. (a, e) show the patterns under microscopy after development, and (b, f) are zoomed-in views. (c, g) display the patterns after the metal layer lift-off process, and (d, h) are the corresponding zoomed-in views.

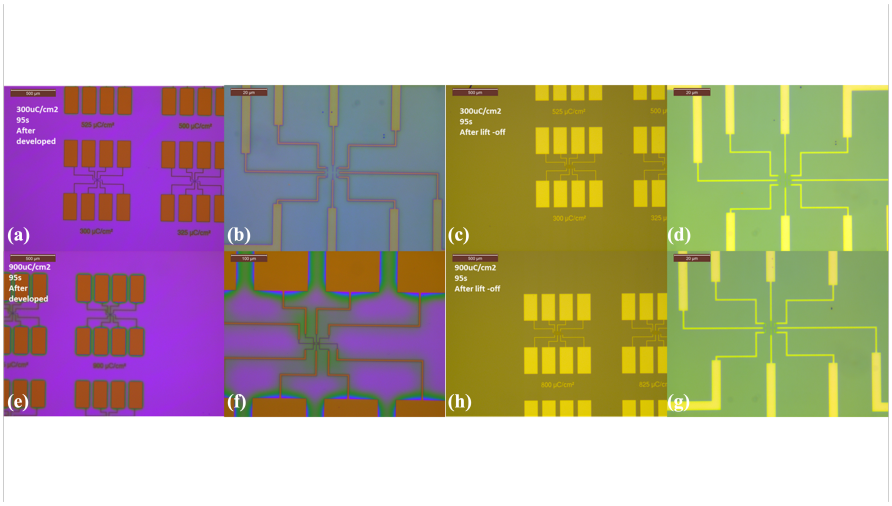

Figure 95: Dose test results in EBL with a development time of 95 s. The images in the upper row (a, b, c, d) were exposed with a dose of 300 $\mu C/cm^2$, while those in the lower row (e, f, g, h) were exposed with 900 $\mu C/cm^2$. (a, e) show the patterns under microscopy after development, and (b, f) are zoomed-in views. (c, g) display the patterns after the metal layer lift-off process, and (d, h) are the corresponding zoomed-in views.

List of publications related to the thesis:

[1] H. Zhang, M. Shen, C. Stenz, C. Teichrib, **Wu, Riga**, L. Schäfer, N. Lin, Y. Zhou, C. Zhou, O. Cojocaru-Mirédin, et al. "Improved Charge Carrier Transport Across Grain Boundaries in N-type PbSe by Dopant Segregation." In: *Small Science* (2024), p. 2300299.

[2] D. An, S. Zhang, X. Zhai, W. Yang, **Wu, Riga**, H. Zhang, W. Fan, W. Wang, S. Chen, O. Cojocaru-Mirédin, et al. "Metavalently bonded tellurides: the essence of improved thermoelectric performance in elemental Te." In: *Nature Communications* 15.1 (2024), p. 3177.

[3] **Wu, Riga**, Y. Yu, S. Jia, C. Zhou, O. Cojocaru-Mirédin, and M. Wuttig. "Strong charge carrier scattering at grain boundaries of PbTe caused by the collapse of metavalent bonding." In: *Nature Communications* 14.1 (2023), p. 719.

BIBLIOGRAPHY

[1] Y. Liu, M. Zhou, and J. He. "Towards higher thermoelectric performance of Bi2Te3 via defect engineering." In: *Scripta Materialia* 111 (2016), pp. 39–43.

[2] T.-Y. Hsieh, H. Lin, T.-J. Hsieh, and J.-C. Huang. "Thermal conductivity modeling of periodic porous silicon with aligned cylindrical pores." In: *Journal of Applied Physics* 111.12 (2012).

[3] T. Kanno, H. Tamaki, H. K. Sato, S. D. Kang, S. Ohno, K. Imasato, J. J. Kuo, G. J. Snyder, and Y. Miyazaki. "Enhancement of average thermoelectric figure of merit by increasing the grain-size of Mg3. 2Sb1. 5Bio. 49Teo. 01." In: *Applied Physics Letters* 112.3 (2018).

[4] Q. Qiu, Y. Liu, K. Xia, T. Fang, J. Yu, X. Zhao, and T. Zhu. "Grain Boundary Scattering of Charge Transport in n-Type (Hf, Zr) CoSb Half-Heusler Thermoelectric Materials." In: *Advanced Energy Materials* 9.11 (2019), p. 1803447.

[5] H. Bishara, M. Ghidelli, and G. Dehm. "Approaches to measure the resistivity of grain boundaries in metals with high sensitivity and spatial resolution: a case study employing Cu." In: *ACS applied electronic materials* 2.7 (2020), pp. 2049–2056.

[6] T.-H. Kim, X.-G. Zhang, D. M. Nicholson, B. M. Evans, N. S. Kulkarni, B. Radhakrishnan, E. A. Kenik, and A.-P. Li. "Large discrete resistance jump at grain boundary in copper nanowire." In: *Nano letters* 10.8 (2010), pp. 3096–3100.

[7] H. Bishara, S. Lee, T. Brink, M. Ghidelli, and G. Dehm. "Understanding grain boundary electrical resistivity in Cu: the effect of boundary structure." In: *ACS nano* 15.10 (2021), pp. 16607–16615.

[8] T. H. Ly, D. J. Perello, J. Zhao, Q. Deng, H. Kim, G. H. Han, S. H. Chae, H. Y. Jeong, and Y. H. Lee. "Misorientation-angle-dependent electrical transport across molybdenum disulfide grain boundaries." In: *Nature communications* 7.1 (2016), pp. 1–7.

[9] Q. Yu, L. A. Jauregui, W. Wu, R. Colby, J. Tian, Z. Su, H. Cao, Z. Liu, D. Pandey, D. Wei, et al. "Control and characterization of individual grains and grain boundaries in graphene grown by chemical vapour deposition." In: *Nature materials* 10.6 (2011), pp. 443–449.

[10] M. Zhu, O. Cojocaru-Mirédin, A. M. Mio, J. Keutgen, M. Küpers, Y. Yu, J.-Y. Cho, R. Dronskowski, and M. Wuttig. "Unique bond breaking in crystalline phase change materials and the quest for metavalent bonding." In: *Advanced Materials* 30.18 (2018), p. 1706735.

[11] D. M. Rowe. *CRC handbook of thermoelectrics*. CRC press, 2018.

[12] G. J. Snyder and E. S. Toberer. "Complex thermoelectric materials." In: *Nature materials* 7.2 (2008), pp. 105–114.

[13] T. Zhu, Z. Xu, J. He, J. Shen, S. Zhu, L. Hu, T. M. Tritt, and X. Zhao. "Hot deformation induced bulk nanostructuring of unidirectionally grown p-type (Bi, Sb) 2 Te 3 thermoelectric materials." In: *Journal of Materials Chemistry A* 1.38 (2013), pp. 11589–11594.

[14] K. Biswas, J. He, I. D. Blum, C.-I. Wu, T. P. Hogan, D. N. Seidman, V. P. Dravid, and M. G. Kanatzidis. "High-performance bulk thermoelectrics with all-scale hierarchical architectures." In: *Nature* 489.7416 (2012), pp. 414–418.

[15] X. Shi, J. Yang, J. R. Salvador, M. Chi, J. Y. Cho, H. Wang, S. Bai, J. Yang, W. Zhang, and L. Chen. "Multiple-filled skutterudites: high thermoelectric figure of merit through separately optimizing electrical and thermal transports." In: *Journal of the American Chemical Society* 133.20 (2011), pp. 7837–7846.

[16] C. Fu, S. Bai, Y. Liu, Y. Tang, L. Chen, X. Zhao, and T. Zhu. "Realizing high figure of merit in heavy-band p-type half-Heusler thermoelectric materials." In: *Nature communications* 6.1 (2015), p. 8144.

[17] B. Qin, D. Wang, T. Hong, Y. Wang, D. Liu, Z. Wang, X. Gao, Z.-H. Ge, and L.-D. Zhao. "High thermoelectric efficiency realized in SnSe crystals via structural modulation." In: *Nature Communications* 14.1 (2023), p. 1366.

[18] Z. Xu, H. Wu, T. Zhu, C. Fu, X. Liu, L. Hu, J. He, J. He, and X. Zhao. "Attaining high mid-temperature performance in (Bi, Sb) 2Te3 thermoelectric materials via synergistic optimization." In: *NPG Asia Materials* 8.9 (2016), e302–e302.

[19] T. Zhu, Y. Liu, C. Fu, J. P. Heremans, J. G. Snyder, and X. Zhao. "Compromise and synergy in high-efficiency thermoelectric materials." In: *Advanced materials* 29.14 (2017), p. 1605884.

[20] L.-D. Zhao, S. Hao, S.-H. Lo, C.-I. Wu, X. Zhou, Y. Lee, H. Li, K. Biswas, T. P. Hogan, C. Uher, et al. "High thermoelectric performance via hierarchical compositionally alloyed nanostructures." In: *Journal of the American Chemical Society* 135.19 (2013), pp. 7364–7370.

[21] C. Zhou, Y. K. Lee, J. Cha, B. Yoo, S.-P. Cho, T. Hyeon, and I. Chung. "Defect engineering for high-performance n-type PbSe thermoelectrics." In: *Journal of the American Chemical Society* 140.29 (2018), pp. 9282–9290.

[22] J. P. Heremans, V. Jovovic, E. S. Toberer, A. Saramat, K. Kurosaki, A. Charoenphakdee, S. Yamanaka, and G. J. Snyder. "Enhancement of thermoelectric efficiency in PbTe by distortion of the electronic density of states." In: *Science* 321.5888 (2008), pp. 554–557.

[23] C. Fu, T. Zhu, Y. Liu, H. Xie, and X. Zhao. "Band engineering of high performance p-type FeNbSb based half-Heusler thermoelectric materials for figure of merit zT> 1." In: *Energy & Environmental Science* 8.1 (2015), pp. 216–220.

[24] W. G. Zeier, A. Zevalkink, Z. M. Gibbs, G. Hautier, M. G. Kanatzidis, and G. J. Snyder. "Thinking Like a Chemist: Intuition in Thermoelectric Materials." In: *Angewandte Chemie International Edition* 55.24 (2016), pp. 6826–6841. ISSN: 1521-3773. DOI: 10.1002/anie.201508381.

[25] K. H. Lee, S.-i. Kim, J.-C. Lim, J. Y. Cho, H. Yang, and H.-S. Kim. "Approach to determine the density-of-states effective mass with carrier concentration-dependent Seebeck coefficient." In: *Advanced Functional Materials* 32.33 (2022), p. 2203852.

[26] H. Ibach and H. Lüth. *Solid-state physics: an introduction to principles of materials science*. Springer Science & Business Media, 2009.

[27] Y. Pei, H. Wang, and G. J. Snyder. "Band engineering of thermoelectric materials." In: *Advanced materials* 24.46 (2012), pp. 6125–6135.

[28] G. J. Snyder and E. S. Toberer. "Complex thermoelectric materials." In: *Materials for sustainable energy: a collection of peer-reviewed research and review articles from Nature Publishing Group*. World Scientific, 2011, pp. 101–110.

[29] J. Yang, L. Xi, W. Qiu, L. Wu, X. Shi, L. Chen, J. Yang, W. Zhang, C. Uher, and D. J. Singh. "On the tuning of electrical and thermal transport in thermoelectrics: an integrated theory–experiment perspective." In: *NPJ Computational Materials* 2.1 (2016), pp. 1–17.

[30] J. Yang, H.-L. Yip, and A. K.-Y. Jen. "Rational design of advanced thermoelectric materials." In: *Advanced Energy Materials* 3.5 (2013), pp. 549–565.

[31] Y. Xiao and L.-D. Zhao. "Charge and phonon transport in PbTe-based thermoelectric materials." In: *npj Quantum Materials* 3.1 (2018), p. 55.

[32] C. Zhang, X. Geng, B. Chen, J. Li, A. Meledin, L. Hu, F. Liu, J. Shi, J. Mayer, M. Wuttig, et al. "Boron-Mediated Grain Boundary Engineering Enables Simultaneous Improvement of Thermoelectric and Mechanical Properties in N-Type Bi2Te3." In: *Small* 17.42 (2021), p. 2104067.

[33] D. An, S. Chen, Z. Lu, R. Li, W. Chen, W. Fan, W. Wang, and Y. Wu. "Low thermal conductivity and optimized thermoelectric properties of p-type Te–Sb2Se3: synergistic effect of doping and defect engineering." In: *ACS applied materials & interfaces* 11.31 (2019), pp. 27788–27797.

[34] G. Tan, L.-D. Zhao, and M. G. Kanatzidis. "Rationally designing high-performance bulk thermoelectric materials." In: *Chemical reviews* 116.19 (2016), pp. 12123–12149.

[35] Y. Yu, H. Wu, and J. He. "Synergistic strategies to boost lead telluride as prospective thermoelectrics." In: *Thin Film and Flexible Thermoelectric Generators, Devices and Sensors* (2021), pp. 155–189.

[36] Y. Yu, C. Zhou, X. Zhang, L. Abdellaoui, C. Doberstein, B. Berkels, B. Ge, G. Qiao, C. Scheu, M. Wuttig, et al. "Dynamic doping and Cottrell atmosphere optimize the thermoelectric performance of n-type PbTe over a broad temperature interval." In: *Nano Energy* 101 (2022), p. 107576.

[37] H. Dow, M. Oh, B. Kim, S. Park, B. Min, H. Lee, and D. Wee. "Effect of Ag or Sb addition on the thermoelectric properties of PbTe." In: *Journal of Applied Physics* 108.11 (2010), p. 113709.

[38] Y. Pei, A. F. May, and G. J. Snyder. "Self-tuning the carrier concentration of PbTe/Ag2Te composites with excess Ag for high thermoelectric performance." In: *Advanced Energy Materials* 1.2 (2011), pp. 291–296.

[39] A. Sheskin et al. "Tailoring Thermoelectric Transport Properties of Ag-Alloyed PbTe: Effects of Microstructure Evolution." In: *ACS Applied Materials & Interfaces* 10.45 (2018), pp. 38994–39001. ISSN: 1944-8244, 1944-8252. DOI: 10.1021/acsami.8b15204. (Visited on 12/05/2022).

[40] X. Chen, F. Cai, C. Liu, R. Dong, L. Qiu, L. Jiang, G. Yuan, and Q. Zhang. "Enhanced thermoelectric performance of Bi2Te2. 7Seo. 3/Bi2S3 synthesized by anion exchange method." In: *physica status solidi (RRL)–Rapid Research Letters* 14.4 (2020), p. 1900679.

[41] Y. Yu, M. Cagnoni, O. Cojocaru-Mirédin, and M. Wuttig. "Chalcogenide thermoelectrics empowered by an unconventional bonding mechanism." In: *Advanced Functional Materials* 30.8 (2020), p. 1904862.

[42] Y. Yu, M. Cagnoni, O. Cojocaru-Mirédin, and M. Wuttig. "Chalcogenide Thermoelectrics Empowered by an Unconventional Bonding Mechanism." In: *Advanced Functional Materials* 30.8 (2020), p. 1904862. ISSN: 1616-3028. DOI: 10.1002/adfm.201904862.

[43] G. J. Snyder, A. H. Snyder, M. Wood, R. Gurunathan, B. H. Snyder, and C. Niu. "Weighted mobility." In: *Advanced Materials* 32.25 (2020), p. 2001537.

[44] J. J. Kuo, S. D. Kang, K. Imasato, H. Tamaki, S. Ohno, T. Kanno, and G. J. Snyder. "Grain boundary dominated charge transport in Mg 3 Sb 2-based compounds." In: *Energy & Environmental Science* 11.2 (2018), pp. 429–434.

[45] D. K. Ferry. *Semiconductors: Bonds and bands*. IoP Publishing, 2013.

[46] H. Wang, Y. Pei, A. D. LaLonde, and G. J. Snyder. "Weak electron–phonon coupling contributing to high thermoelectric performance in n-type PbSe." In: *Proceedings of the National Academy of Sciences* 109.25 (2012), pp. 9705–9709.

[47] S. Kasap, C. Koughia, and H. E. Ruda. "Electrical conduction in metals and semiconductors." In: *Springer handbook of electronic and photonic materials* (2017), pp. 1–1.

[48] B.-K. Hong, H. S. Yun, and I.-H. Kim. "Thermoelectric performance of famatinites double-doped with Ge and In." In: *Journal of the Korean Physical Society* (2024), pp. 1–7.

[49] S. Song, J. Mao, M. Bordelon, R. He, Y. Wang, J. Shuai, J. Sun, X. Lei, Z. Ren, S. Chen, et al. "Joint effect of magnesium and yttrium on enhancing thermoelectric properties of n-type Zintl Mg3+ δYo. o2Sb1. 5Bio. 5." In: *Materials Today Physics* 8 (2019), pp. 25–33.

[50] J. Shen, L. Hu, T. Zhu, and X. Zhao. "The texture related anisotropy of thermoelectric properties in bismuth telluride based polycrystalline alloys." In: *Applied Physics Letters* 99.12 (2011), p. 124102.

[51] L.-P. Hu, T.-J. Zhu, Y.-G. Wang, H.-H. Xie, Z.-J. Xu, and X.-B. Zhao. "Shifting up the optimum figure of merit of p-type bismuth telluride-based thermoelectric materials for power generation by suppressing intrinsic conduction." In: *NPG Asia Materials* 6.2 (2014), e88–e88.

[52] H. Wang, A. D. LaLonde, Y. Pei, and G. J. Snyder. "The criteria for beneficial disorder in thermoelectric solid solutions." In: *Advanced Functional Materials* 23.12 (2013), pp. 1586–1596.

[53] B. Qiu, Z. Tian, A. Vallabhaneni, B. Liao, J. M. Mendoza, O. D. Restrepo, X. Ruan, and G. Chen. "First-principles simulation of electron mean-free-path spectra and thermoelectric properties in silicon." In: *Europhysics Letters* 109.5 (2015), p. 57006.

[54] C. Hu, K. Xia, C. Fu, X. Zhao, and T. Zhu. "Carrier grain boundary scattering in thermoelectric materials." In: *Energy & Environmental Science* (2022).

[55] W. Steinhögl, G. Schindler, G. Steinlesberger, and M. Engelhardt. "Size-dependent resistivity of metallic wires in the mesoscopic range." In: *Physical Review B* 66.7 (2002), p. 075414.

[56] H. Mataré. "Carrier transport at grain boundaries in semiconductors." In: *Journal of applied physics* 56.10 (1984), pp. 2605–2631.

[57] M. T. Dylla, J. J. Kuo, I. Witting, and G. J. Snyder. "Grain boundary engineering nanostructured $SrTiO_3$ for thermoelectric applications." In: *Advanced Materials Interfaces* 6.15 (2019), p. 1900222.

[58] Y. Lin, M. T. Dylla, J. J. Kuo, J. P. Male, I. A. Kinloch, R. Freer, and G. J. Snyder. "Graphene/strontium titanate: approaching single crystal–like charge transport in polycrystalline oxide perovskite nanocomposites through grain boundary engineering." In: *Advanced Functional Materials* 30.12 (2020), p. 1910079.

[59] V. H. Nguyen, U. Gottlieb, A. Valla, D. Muñoz, D. Bellet, and D. Muñoz-Rojas. "Electron tunneling through grain boundaries in transparent conductive oxides and implications for electrical conductivity: the case of ZnO: Al thin films." In: *Materials Horizons* 5.4 (2018), pp. 715–726.

[60] J. Bauerle. "Study of solid electrolyte polarization by a complex admittance method." In: *Journal of Physics and Chemistry of Solids* 30.12 (1969), pp. 2657–2670.

[61] Z. Li, Z. Yang, and B. Du. "Surface charge transport characteristics of ZnO/silicone rubber composites under impulse superimposed on DC voltage." In: *IEEE Access* 7 (2018), pp. 3008–3017.

[62] K. Eda. "Conduction mechanism of non-Ohmic zinc oxide ceramics." In: *Journal of Applied Physics* 49.5 (1978), pp. 2964–2972.

[63] H. Schroeder. "Poole-Frenkel-effect as dominating current mechanism in thin oxide films—An illusion?!" In: *Journal of Applied Physics* 117.21 (2015).

[64] J. Y. Seto. "The electrical properties of polycrystalline silicon films." In: *Journal of Applied Physics* 46.12 (1975), pp. 5247–5254.

[65] H. A. Bethe. "Theory of the boundary layer of crystal rectifiers." In: *Semiconductor Devices: Pioneering Papers*. World Scientific, 1991, pp. 387–399.

[66] J. Cao, D. Ekren, Y. Peng, F. Azough, I. A. Kinloch, and R. Freer. "Modulation of charge transport at grain boundaries in SrTiO3: toward a high thermoelectric power factor at room temperature." In: *ACS applied materials & interfaces* 13.10 (2021), pp. 11879–11890.

[67] J. Shen, L. Fan, C. Hu, T. Zhu, J. Xin, T. Fu, D. Zhao, and X. Zhao. "Enhanced thermoelectric performance in the n-type NbFeSb half-Heusler compound with heavy element Ir doping." In: *Materials Today Physics* 8 (2019), pp. 62–70.

[68] T. J. Slade, J. A. Grovogui, J. J. Kuo, S. Anand, T. P. Bailey, M. Wood, C. Uher, G. J. Snyder, V. P. Dravid, and M. G. Kanatzidis. "Understanding the thermally activated charge transport in NaPb m SbQ m+ 2 (Q= S, Se, Te) thermoelectrics: weak dielectric screening leads to grain boundary dominated charge carrier scattering." In: *Energy & Environmental Science* 13.5 (2020), pp. 1509–1518.

[69] J. Singh. *Electronic and optoelectronic properties of semiconductor structures*. Cambridge University Press, 2007.

[70] Q. Ren, C. Fu, Q. Qiu, S. Dai, Z. Liu, T. Masuda, S. Asai, M. Hagihala, S. Lee, S. Torri, et al. "Establishing the carrier scattering phase diagram for ZrNiSn-based half-Heusler thermoelectric materials." In: *Nature communications* 11.1 (2020), p. 3142.

[71] R. Su, Z. Xu, J. Wu, D. Luo, Q. Hu, W. Yang, X. Yang, R. Zhang, H. Yu, T. P. Russell, et al. "Dielectric screening in perovskite photovoltaics." In: *Nature communications* 12.1 (2021), p. 2479.

[72] J. John and A. N. Bloch. "Quantum-Defect Electronegativity Scale for Nontransition Elements." In: *Physical Review Letters* 33.18 (1974), pp. 1095–1098. ISSN: 0031-9007. DOI: 10.1103/PhysRevLett.33.1095.

[73] P. B. Littlewood. "The Dielectric Constant of Cubic IV-VI Compounds." In: *Journal of Physics C: Solid State Physics* 12.21 (1979), pp. 4459–4468. ISSN: 0022-3719. DOI: 10.1088/0022-3719/12/21/013.

[74] W. B. Jensen. "The Historical Development of the van Arkel Bond-Type Diagram." In: *Bull. Hist. Chem* 13.14 (1992), pp. 47–59.

[75] J.-Y. Raty, M. Schumacher, P. Golub, V. L. Deringer, C. Gatti, and M. Wuttig. "A quantum-mechanical map for bonding and properties in solids." In: *Advanced materials* 31.3 (2019), p. 1806280.

[76] D. Lencer, M. Salinga, B. Grabowski, T. Hickel, J. Neugebauer, and M. Wuttig. "A map for phase-change materials." In: *Nature materials* 7.12 (2008), pp. 972–977.

[77] K. Shportko, S. Kremers, M. Woda, D. Lencer, J. Robertson, and M. Wuttig. "Resonant Bonding in Crystalline Phase-Change Materials." In: *Nature Materials* 7.8 (2008), pp. 653–658. ISSN: 1476-1122, 1476-4660. DOI: 10.1038/nmat2226.

[78] M. Wuttig, V. L. Deringer, X. Gonze, C. Bichara, and J.-Y. Raty. "Incipient Metals: Functional Materials with a Unique Bonding Mechanism." In: *Advanced Materials* 30.51 (2018), p. 1803777. ISSN: 1521-4095. DOI: 10.1002/adma.201803777.

[79] M. Raghuwanshi, O. Cojocaru-Mirédin, and M. Wuttig. "Investigating Bond Rupture in Resonantly Bonded Solids by Field Evaporation of Carbon Nanotubes." In: *Nano Letters* 20.1 (2020), pp. 116–121. ISSN: 1530-6984, 1530-6992. DOI: 10/gkb8b6.

[80] M. Wuttig, V. L. Deringer, X. Gonze, C. Bichara, and J.-Y. Raty. "Incipient metals: functional materials with a unique bonding mechanism." In: *Advanced materials* 30.51 (2018), p. 1803777.

[81] Y. Cheng, S. Wahl, and M. Wuttig. "Metavalent bonding in solids: characteristic representatives, their properties, and design options." In: *physica status solidi (RRL)–Rapid Research Letters* 15.3 (2021), p. 2000482.

[82] Y. Zhang, X. Ke, C. Chen, J. Yang, and P. Kent. "Thermodynamic properties of PbTe, PbSe, and PbS: First-principles study." In: *Physical Review B—Condensed Matter and Materials Physics* 80.2 (2009), p. 024304.

[83] K. Shportko, S. Kremers, M. Woda, D. Lencer, J. Robertson, and M. Wuttig. "Resonant bonding in crystalline phase-change materials." In: *Nature materials* 7.8 (2008), pp. 653–658.

[84] S. Lee, K. Esfarjani, T. Luo, J. Zhou, Z. Tian, and G. Chen. "Resonant bonding leads to low lattice thermal conductivity." In: *Nature communications* 5.1 (2014), p. 3525.

[85] P. Littlewood. "The dielectric constant of cubic IV-VI compounds." In: *Journal of Physics C: Solid State Physics* 12.21 (1979), p. 4459.

[86] B. J. Kooi and M. Wuttig. "Chalcogenides by design: Functionality through metavalent bonding and confinement." In: *Advanced materials* 32.21 (2020), p. 1908302.

[87] L. Guarneri, S. Jakobs, A. von Hoegen, S. Maier, M. Xu, M. Zhu, S. Wahl, C. Teichrib, Y. Zhou, O. Cojocaru-Mirédin, et al. "Metavalent bonding in crystalline solids: how does it collapse?" In: *Advanced Materials* 33.39 (2021), p. 2102356.

[88] D. Lencer, M. Salinga, and M. Wuttig. "Design rules for phase-change materials in data storage applications." In: *Advanced Materials* 23.18 (2011), pp. 2030–2058.

[89] J.-Y. Raty, M. Schumacher, P. Golub, V. L. Deringer, C. Gatti, and M. Wuttig. "A Quantum-Mechanical Map for Bonding and Properties in Solids." In: *Advanced Materials* 31.3 (2019), p. 1806280. ISSN: 1521-4095. DOI: 10.1002/adma.201806280.

[90] Y. Cheng, S. Wahl, and M. Wuttig. "Metavalent Bonding in Solids: Characteristic Representatives, Their Properties, and Design Options." In: *physica status solidi (RRL) – Rapid Research Letters* 15.3 (2021), p. 2000482. ISSN: 1862-6270. DOI: 10.1002/pssr.202000482.

[91] O. Cojocaru-Mirédin, Y. Yu, J. Köttgen, T. Ghosh, C.-F. Schön, S. Han, C. Zhou, M. Zhu, and M. Wuttig. "Atom probe tomography: a local probe for chemical bonds in solids." In: *Advanced Materials* (2024), p. 2403046.

[92] S. Maier, S. Steinberg, Y. Cheng, C.-F. Schön, M. Schumacher, R. Mazzarello, P. Golub, R. Nelson, O. Cojocaru-Mirédin, J.-Y. Raty, et al. "Discovering Electron-Transfer-Driven Changes in Chemical Bonding in Lead Chalcogenides (PbX, where X= Te, Se, S, O)." In: *Advanced Materials* 32.49 (2020), p. 2005533.

[93] D. J. Larson, T. Prosa, R. M. Ulfig, B. P. Geiser, and T. F. Kelly. "Local electrode atom probe tomography." In: *New York, US: Springer Science* 2 (2013).

[94] D. J. Grant and S. Sivoththaman. "Electron-beam lithography: From past to present." In: *University of Waterloo, Canada* (2003).

[95] T. Heinzel. *Mesoscopic electronics in solid state nanostructures*. John Wiley & Sons, 2008.

[96] P. J. Moll. "The role of anisotropy in iron-pnictides addressed by focused ion beam sample fabrication." PhD thesis. ETH Zurich, 2012.

[97] K. Thompson, D. Lawrence, D. Larson, J. Olson, T. Kelly, and B. Gorman. "In situ site-specific specimen preparation for atom probe tomography." In: *Ultramicroscopy* 107.2-3 (2007), pp. 131–139.

[98] V. Sarin. *Comprehensive hard materials*. Newnes, 2014.

[99] T. Muller-Reichert and P. Verkade. *Correlative light and electron microscopy*. Vol. 111. Academic Press, 2012.

[100] N. Yao. *Focused ion beam systems: basics and applications*. Cambridge University Press, 2007.

[101] A. Botman, J. Mulders, R. Weemaes, and S. Mentink. "Purification of platinum and gold structures after electron-beam-induced deposition." In: *Nanotechnology* 17.15 (2006), p. 3779.

[102] "Materials Using Atom Probe Tomography." In: *Materials Today* 32 (2020), pp. 260–274. DOI: 10.1016/j.mattod.2019.11.010.

[103] M. K. Miller and K. F. Russell. "Atom probe specimen preparation with a dual beam SEM/FIB miller." In: *Ultramicroscopy* 107.9 (2007), pp. 761–766.

[104] B. Gault, A. Chiaramonti, O. Cojocaru-Mirédin, P. Stender, R. Dubosq, C. Freysoldt, S. K. Makineni, T. Li, M. Moody, and J. M. Cairney. "Atom probe tomography." In: *Nature Reviews Methods Primers* 1.1 (2021), p. 51.

[105] M. Miller, K. Russell, and G. Thompson. "Strategies for fabricating atom probe specimens with a dual beam FIB." In: *Ultramicroscopy* 102.4 (2005), pp. 287–298.

[106] A. J. Breen, K. Y. Xie, M. P. Moody, B. Gault, H.-W. Yen, C. C. Wong, J. M. Cairney, and S. P. Ringer. "Resolving the morphology of niobium carbonitride nano-precipitates in steel using atom probe tomography." In: *Microscopy and Microanalysis* 20.4 (2014), pp. 1100–1110.

[107] Y. Yu, C. Zhou, S. Zhang, M. Zhu, M. Wuttig, C. Scheu, D. Raabe, G. J. Snyder, B. Gault, and O. Cojocaru-Mirédin. "Revealing nano-chemistry at lattice defects in thermoelectric materials using atom probe tomography." In: *Materials Today* 32 (2020), pp. 260–274.

[108] G. Wu, C. Liu, L. Sun, Q. Wang, B. Sun, B. Han, J.-J. Kai, J. Luan, C. T. Liu, K. Cao, et al. "Hierarchical nanostructured aluminum alloy with ultrahigh strength and large plasticity." In: *Nature Communications* 10.1 (2019), p. 5099.

[109] T. Luo, F. Serrano-Sánchez, H. Bishara, S. Zhang, R. B. Villoro, J. J. Kuo, C. Felser, C. Scheu, G. J. Snyder, J. P. Best, et al. "Dopant-segregation to grain boundaries controls electrical conductivity of n-type NbCo (Pt) Sn half-Heusler alloy mediating thermoelectric performance." In: *Acta Materialia* 217 (2021), p. 117147.

[110] M. Zhou, J.-F. Li, and T. Kita. "Nanostructured AgPb m SbTe m+ 2 system bulk materials with enhanced thermoelectric performance." In: *Journal of the American Chemical Society* 130.13 (2008), pp. 4527–4532.

[111] H. S. Dow, M. W. Oh, B. S. Kim, S. D. Park, B. K. Min, H. W. Lee, and D. M. Wee. "Effect of Ag or Sb Addition on the Thermoelectric Properties of PbTe." In: *Journal of Applied Physics* 108.11 (2010), p. 113709. ISSN: 0021-8979, 1089-7550. DOI: 10.1063/1.3517088. (Visited on 02/01/2023).

[112] Y. Yu, D.-S. He, S. Zhang, O. Cojocaru-Mirédin, T. Schwarz, A. Stoffers, X.-Y. Wang, S. Zheng, B. Zhu, C. Scheu, et al. "Simultaneous optimization of electrical and thermal transport properties of Bio. 5Sb1. 5Te3 thermoelectric alloy by twin boundary engineering." In: *Nano Energy* 37 (2017), pp. 203–213.

[113] K. F. Hsu, S. Loo, F. Guo, W. Chen, J. S. Dyck, C. Uher, T. Hogan, E. Polychroniadis, and M. G. Kanatzidis. "Cubic AgPb m SbTe2+ m: bulk thermoelectric materials with high figure of merit." In: *Science* 303.5659 (2004), pp. 818–821.

[114] S. Wang, G. Zheng, T. Luo, X. She, H. Li, and X. Tang. "Exploring the doping effects of Ag in p-type PbSe compounds with enhanced thermoelectric performance." In: *Journal of Physics D: Applied Physics* 44.47 (2011), p. 475304.

[115] E. Conwell and V. Weisskopf. "Theory of impurity scattering in semiconductors." In: *Physical review* 77.3 (1950), p. 388.

[116] K. Imasato, C. Fu, Y. Pan, M. Wood, J. J. Kuo, C. Felser, and G. J. Snyder. "Metallic n-Type Mg3Sb2 Single Crystals Demonstrate the Absence of Ionized Impurity Scattering and Enhanced Thermoelectric Performance." In: *Advanced Materials* 32.16 (2020), p. 1908218.

[117] H. Wang, E. Schechtel, Y. Pei, and G. J. Snyder. "High thermoelectric efficiency of n-type PbS." In: *Advanced Energy Materials* 3.4 (2013), pp. 488–495.

[118] A. Filippetti, A. Mattoni, C. Caddeo, M. Saba, and P. Delugas. "Low electron-polar optical phonon scattering as a fundamental aspect of carrier mobility in methylammonium lead halide CH 3 NH 3 PbI 3 perovskites." In: *Physical Chemistry Chemical Physics* 18.22 (2016), pp. 15352–15362.

[119] Y. Yu, S. Zhang, A. M. Mio, B. Gault, A. Sheskin, C. Scheu, D. Raabe, F. Zu, M. Wuttig, Y. Amouyal, et al. "Ag-segregation to dislocations in PbTe-based thermoelectric materials." In: *ACS applied materials & interfaces* 10.4 (2018), pp. 3609–3615.

[120] B. Ryu, M.-W. Oh, J. K. Lee, J. E. Lee, S.-J. Joo, B.-S. Kim, B.-K. Min, H.-W. Lee, and S.-D. Park. "Defects responsible for abnormal n-type conductivity in Ag-excess doped PbTe thermoelectrics." In: *Journal of Applied Physics* 118.1 (2015).

[121] L. CHALCOGENIDES. "SEMICONDUCTING LEAD CHALCOGENIDES." In: ().

[122] A. W. Tsen, L. Brown, M. P. Levendorf, F. Ghahari, P. Y. Huang, R. W. Havener, C. S. Ruiz-Vargas, D. A. Muller, P. Kim, and J. Park. "Tailoring electrical transport across grain boundaries in polycrystalline graphene." In: *Science* 336.6085 (2012), pp. 1143–1146.

[123] S. Ghosh, A. Sarkar, S. Chaudhuri, and A. Pal. "Grain boundary scattering in aluminium-doped ZnO films." In: *Thin Solid Films* 205.1 (1991), pp. 64–68.

[124] K. Kishimoto, K. Yamamoto, and T. Koyanagi. "Influences of potential barrier scattering on the thermoelectric properties of sintered n-type PbTe with a small grain size." In: *Japanese journal of applied physics* 42.2R (2003), p. 501.

[125] J. Resende, V.-S. Nguyen, C. Fleischmann, L. Bottiglieri, S. Brochen, W. Vandervorst, W. Favre, C. Jiménez, J.-L. Deschanvres, and N. D. Nguyen. "Grain-boundary segregation of magnesium in doped cuprous oxide and impact on electrical transport properties." In: *Scientific Reports* 11.1 (2021), p. 7788.

[126] E. Shi, S. Cui, N. Kempf, Q. Xing, T. Chasapis, H. Zhu, Z. Li, J.-H. Bahk, G. J. Snyder, Y. Zhang, et al. "Origin of inhomogeneity in spark plasma sintered bismuth antimony telluride thermoelectric nanocomposites." In: *Nano Research* 13 (2020), pp. 1339–1346.

[127] D. Feng and G. Jin. *Introduction To Condensed Matter Physics, Volume 1*. World Scientific Publishing Company, 2005.

[128] R. Grantab, V. B. Shenoy, and R. S. Ruoff. "Anomalous strength characteristics of tilt grain boundaries in graphene." In: *Science* 330.6006 (2010), pp. 946–948.

[129] D. Brandon. "The structure of high-angle grain boundaries." In: *Acta metallurgica* 14.11 (1966), pp. 1479–1484.

[130] V. A. Ivanov. *On kinetics and thermodynamics of high angle grain boundaries in aluminum: Experimental study on grain boundary properties in bi-and tricrystals*. Tech. rep. Technical Report, 2006.

[131] C. H. Liebscher, A. Stoffers, M. Alam, L. Lymperakis, O. Cojocaru-Mirédin, B. Gault, J. Neugebauer, G. Dehm, C. Scheu, and D. Raabe. "Strain-induced asymmetric line segregation at faceted Si grain boundaries." In: *Physical review letters* 121.1 (2018), p. 015702.

[132] T. Frolov, W. Setyawan, R. Kurtz, J. Marian, A. R. Oganov, R. E. Rudd, and Q. Zhu. "Grain boundary phases in bcc metals." In: *Nanoscale* 10.17 (2018), pp. 8253–8268.

[133] S. Najmaei, M. Amani, M. L. Chin, Z. Liu, A. G. Birdwell, T. P. O'Regan, P. M. Ajayan, M. Dubey, and J. Lou. "Electrical transport properties of polycrystalline monolayer molybdenum disulfide." In: *ACS nano* 8.8 (2014), pp. 7930–7937.

[134] K. Hsieh, V. Kochat, X. Zhang, Y. Gong, C. S. Tiwary, P. M. Ajayan, and A. Ghosh. "Effect of carrier localization on electrical transport and noise at individual grain boundaries in monolayer MoS2." In: *Nano letters* 17.9 (2017), pp. 5452–5457.

[135] R. Ma, Q. Huan, L. Wu, J. Yan, W. Guo, Y.-Y. Zhang, S. Wang, L. Bao, Y. Liu, S. Du, et al. "Direct four-probe measurement of grain-boundary resistivity and mobility in millimeter-sized graphene." In: *Nano Letters* 17.9 (2017), pp. 5291–5296.

[136] W. Wu, S. Brongersma, M. Van Hove, and K. Maex. "Influence of surface and grain-boundary scattering on the resistivity of copper in reduced dimensions." In: *Applied physics letters* 84.15 (2004), pp. 2838–2840.

[137] Q. Huang, C. M. Lilley, M. Bode, and R. Divan. "Surface and size effects on the electrical properties of Cu nanowires." In: *Journal of Applied Physics* 104.2 (2008), p. 023709.

[138] T. Luo, J. J. Kuo, K. J. Griffith, K. Imasato, O. Cojocaru-Mirédin, M. Wuttig, B. Gault, Y. Yu, and G. J. Snyder. "Nb-Mediated Grain Growth and Grain-Boundary Engineering in Mg3Sb2-Based Thermoelectric Materials." In: *Advanced Functional Materials* 31.28 (2021), p. 2100258.

[139] J. Martin, L. Wang, L. Chen, and G. Nolas. "Enhanced Seebeck coefficient through energy-barrier scattering in PbTe nanocomposites." In: *Physical review B* 79.11 (2009), p. 115311.

[140] J.-S. Park and A. Walsh. "Modeling grain boundaries in polycrystalline halide perovskite solar cells." In: *Annual Review of Condensed Matter Physics* 12.1 (2021), pp. 95–109.

[141] T. Ishibe, R. Okuhata, T. Kaneko, M. Yoshiya, S. Nakashima, A. Ishida, and Y. Nakamura. "Heat transport through propagon-phonon interaction in epitaxial amorphous-crystalline multilayers." In: *Communications Physics* 4.1 (2021), p. 153.

[142] J. Keutgen, A. J. London, and O. Cojocaru-Mirédin. "Solving peak overlaps for proximity histogram analysis of complex interfaces for atom probe tomography data." In: *Microscopy and Microanalysis* 27.1 (2021), pp. 28–35.

[143] Z. Peng, Y. Lu, C. Hatzoglou, A. Kwiatkowski da Silva, F. Vurpillot, D. Ponge, D. Raabe, and B. Gault. "An automated computational approach for complete in-plane compositional interface analysis by atom probe tomography." In: *Microscopy and Microanalysis* 25.2 (2019), pp. 389–400.

[144] S. Hofmann. "Segregation to surfaces and interfaces." In: *Scanning Electron Microscopy* 1985.3 (1985), p. 16.

[145] J. J. Kuo, Y. Yu, S. D. Kang, O. Cojocaru-Mirédin, M. Wuttig, and G. J. Snyder. "Mg Deficiency in Grain Boundaries of n-Type Mg3Sb2 Identified by Atom Probe Tomography." In: *Advanced Materials Interfaces* 6.13 (2019), p. 1900429.

[146] D. Raabe, M. Herbig, S. Sandlöbes, Y. Li, D. Tytko, M. Kuzmina, D. Ponge, and P.-P. Choi. "Grain boundary segregation engineering in metallic alloys: A pathway to the design of interfaces." In: *Current Opinion in Solid State and Materials Science* 18.4 (2014), pp. 253–261.

[147] B. W. Krakauer and D. N. Seidman. "Absolute atomic-scale measurements of the Gibbsian interfacial excess of solute at internal interfaces." In: *Physical Review B* 48.9 (1993), p. 6724.

[148] N. W. Ashcroft and N. Mermin. "Solid state." In: *Physics (New York: Holt, Rinehart and Winston) Appendix C* (1976).

[149] J. G. Kirkwood. "On the theory of dielectric polarization." In: *The Journal of Chemical Physics* 4.9 (1936), pp. 592–601.

[150] R. H. Lyddane, R. Sachs, and E. Teller. "On the polar vibrations of alkali halides." In: *Physical Review* 59.8 (1941), p. 673.

[151] G. N. Lewis. "The atom and the molecule." In: *Journal of the American Chemical Society* 38.4 (1916), pp. 762–785.

[152] J.-Y. Raty and M. Wuttig. "The interplay between Peierls distortions and metavalent bonding in IV–VI compounds: comparing GeTe with related monochalcogenides." In: *Journal of Physics D: Applied Physics* 53.23 (2020), p. 234002.

[153] S. Farokhipoor and B. Noheda. "Conduction through 71 domain walls in BiFeO 3 thin films." In: *Physical Review Letters* 107.12 (2011), p. 127601.

[154] K.-C. Kim, J. Lee, B. K. Kim, W. Y. Choi, H. J. Chang, S. O. Won, B. Kwon, S. K. Kim, D.-B. Hyun, H. J. Kim, et al. "Free-electron creation at the 60 twin boundary in Bi2Te3." In: *Nature communications* 7.1 (2016), p. 12449.

[155] L.-D. Zhao, S.-H. Lo, Y. Zhang, H. Sun, G. Tan, C. Uher, C. Wolverton, V. P. Dravid, and M. G. Kanatzidis. "Ultralow thermal conductivity and high thermoelectric figure of merit in SnSe crystals." In: *nature* 508.7496 (2014), pp. 373–377.

[156] E. Billig and M. Ridout. "Transmission of electrons and holes across a twin boundary in germanium." In: *Nature* 173 (1954), pp. 496–497.

[157] J. Mao, Y. Wang, H. S. Kim, Z. Liu, U. Saparamadu, F. Tian, K. Dahal, J. Sun, S. Chen, W. Liu, et al. "High thermoelectric power factor in Cu–Ni alloy originate from potential barrier scattering of twin boundaries." In: *Nano Energy* 17 (2015), pp. 279–289.

[158] B. Cook, M. Kramer, X. Wei, J. Harringa, and E. Levin. "Nature of the cubic to rhombohedral structural transformation in (Ag Sb Te 2) 15 (Ge Te) 85 thermoelectric material." In: *Journal of Applied Physics* 101.5 (2007), p. 053715.

[159] P. Puneet, R. Podila, M. Karakaya, S. Zhu, J. He, T. M. Tritt, M. S. Dresselhaus, and A. M. Rao. "Preferential scattering by interfacial charged defects for enhanced thermoelectric performance in few-layered n-type Bi2Te3." In: *Scientific Reports* 3.1 (2013), pp. 1–7.

[160] Q. Zhang, Y. Lin, N. Lin, Y. Yu, F. Liu, C. Fu, B. Ge, O. Cojocaru-Mirédin, T. Zhu, and X. Zhao. "Enhancing the room temperature thermoelectric performance of n-type Bismuth-telluride-based polycrystalline materials by low-angle grain boundaries." In: *Materials Today Physics* 22 (2022), p. 100573.

[161] D. L. Medlin and G. Snyder. "Atomic-scale interfacial structure in rock salt and tetradymite chalcogenide thermoelectric materials." In: *Jom* 65 (2013), pp. 390–400.

[162] M. V. Kumar, R. Kumar, K. Rajaprian, and K. Singh. "Mineralogical studies of plagioclase feldspar in Kadavur Anorthosite Complex, Tamilnadu." In: *Int. J. Adv. Geosci.* 2 (2014), pp. 31–37.

[163] H. Bhasker, V. Thakur, S. Shivaprasad, and S. Dhar. "Role of quantum confinement in giving rise to high electron mobility in GaN nanowall networks." In: *Solid State Communications* 220 (2015), pp. 72–76.

[164] R. Venkatasubramanian, E. Siivola, T. Colpitts, and B. O'quinn. "Thin-film thermoelectric devices with high room-temperature figures of merit." In: *Nature* 413.6856 (2001), pp. 597–602.

[165] A. M. Van Der Zande, P. Y. Huang, D. A. Chenet, T. C. Berkelbach, Y. You, G.-H. Lee, T. F. Heinz, D. R. Reichman, D. A. Muller, and J. C. Hone. "Grains and grain boundaries in highly crystalline monolayer molybdenum disulphide." In: *Nature materials* 12.6 (2013), pp. 554–561.

[166] A. Zhang, B. Zhang, W. Lu, D. Xie, H. Ou, X. Han, J. Dai, X. Lu, G. Han, G. Wang, et al. "Twin engineering in solution-synthesized nonstoichiometric Cu5FeS4 icosahedral nanoparticles for enhanced thermoelectric performance." In: *Advanced Functional Materials* 28.10 (2018), p. 1705117.

[167] P. Walker. "The thermal conductivity and thermoelectric power of bismuth telluride at low temperatures." In: *Proceedings of the Physical Society* 76.1 (1960), p. 113.

[168] M. Lewin, C. Baeumer, F. Gunkel, A. Schwedt, F. Gaussmann, J. Wueppen, P. Meuffels, B. Jungbluth, J. Mayer, R. Dittmann, et al. "Nanospectroscopy of infrared phonon resonance enables local quantification of electronic properties in doped SrTiO3 ceramics." In: *Advanced functional materials* 28.42 (2018), p. 1802834.

[169] S. Lin, W. Li, Z. Chen, J. Shen, B. Ge, and Y. Pei. "Tellurium as a high-performance elemental thermoelectric." In: *Nature communications* 7.1 (2016), p. 10287.

[170] C. Adenis, V. Langer, and O. Lindqvist. "Reinvestigation of the structure of tellurium." In: *Acta Crystallographica Section C: Crystal Structure Communications* 45.6 (1989), pp. 941–942.

[171] D. Yang, W. Yao, Y. Yan, W. Qiu, L. Guo, X. Lu, C. Uher, X. Han, G. Wang, T. Yang, et al. "Intrinsically low thermal conductivity from a quasi-one-dimensional crystal structure and enhanced electrical conductivity network via Pb doping in SbCrSe3." In: *NPG Asia Materials* 9.6 (2017), e387–e387.

[172] X. Qian, Y. Xiao, L. Zheng, B. Qin, Y. Zhou, Y. Pei, B. Yuan, S. Gong, and L.-D. Zhao. "Effective dopants in p-type elementary Te thermoelectrics." In: *RSC advances* 7.29 (2017), pp. 17682–17688.

[173] X. Qian, Y. Xiao, L. Zheng, B. Qin, Y. Zhou, and Y. Pei. "Effective Dopants in P-Type Elementary Te Thermoelectrics." In: *RSC advances* 7 (2017), pp. 17682–17688. DOI: 10.1039/C7RA01706E.

[174] H. Peng, N. Kioussis, and G. J. Snyder. "Elemental tellurium as a chiral p-type thermoelectric material." In: *Physical Review B* 89.19 (2014), p. 195206.

[175] S. Lin, W. Li, Z. Chen, J. Shen, B. Ge, and Y. Pei. "Tellurium as a High-Performance Elemental Thermoelectric." In: *Nature Communications* 7.1 (2016), p. 10287. ISSN: 2041-1723. DOI: 10.1038/ncomms10287.

[176] M. Yang, T. Su, H. Zhu, S. Li, M. Hu, Q. Hu, H. Ma, and X. Jia. "Thermoelectric performance of Te doped with As and alloyed with Se." In: *Journal of Materials Science* 53 (2018), pp. 11524–11533.

[177] M. Yang, T. Su, H. Zhu, S. Li, M. Hu, and Q. Hu. "Thermoelectric Performance of Te Doped with As and Alloyed with Se." In: *Journal of materials science* 53 (2018), pp. 11524–11533. DOI: 10.1007/s10853-018-2389-y.

[178] S. Lin, W. Li, X. Zhang, J. Li, Z. Chen, and Y. Pei. "Sb Induces Both Doping and Precipitation for Improving the Thermoelectric Performance of Elemental Te." In: *Chem. Front* 4 (2017), pp. 1066–1072.

[179] O. Cojocaru-Mirédin, M. Raghuwanshi, R. Wuerz, and S. Sadewasser. "Grain Boundaries in Cu (In, Ga) Se2: A Review of Composition–Electronic Property Relationships by Atom Probe Tomography and Correlative Microscopy." In: *Advanced Functional Materials* 31.41 (2021), p. 2103119.

[180] M. Raghuwanshi, J. Keutgen, A. M. Mio, H. Mirhosseini, T. D. Kühne, and O. Cojocaru-Mirédin. "The Physics of Twin Boundary Termination in Cu (In, Ga) Se2 Absorbers." In: *Solar RRL* 7.7 (2023), p. 2201033.

[181] M. Zhu, O. Cojocaru-Mirédin, A. M. Mio, J. Keutgen, M. Küpers, Y. Yu, J.-Y. Cho, R. Dronskowski, and M. Wuttig. "Unique Bond Breaking in Crystalline Phase Change Materials and the Quest for Metavalent Bonding." In: *Advanced Materials* 30.18 (2018), p. 1706735. ISSN: 1521-4095. DOI: 10.1002/adma.201706735.

[182] S. Lin, W. Li, X. Zhang, J. Li, Z. Chen, and Y. Pei. "Sb induces both doping and precipitation for improving the thermoelectric performance of elemental Te." In: *Inorganic Chemistry Frontiers* 4.6 (2017), pp. 1066–1072.

[183] L.-D. Zhao, H. Wu, S. Hao, C.-I. Wu, X. Zhou, K. Biswas, J. He, T. P. Hogan, C. Uher, C. Wolverton, et al. "All-scale hierarchical thermoelectrics: MgTe in PbTe facilitates valence band convergence and suppresses bipolar thermal transport for high performance." In: *Energy & Environmental Science* 6.11 (2013), pp. 3346–3355.

[184] K. Biswas, J. He, Q. Zhang, G. Wang, C. Uher, V. P. Dravid, and M. G. Kanatzidis. "Strained endotaxial nanostructures with high thermoelectric figure of merit." In: *Nature chemistry* 3.2 (2011), pp. 160–166.

[185] D. Haneman. "Photoelectric emission and work functions of InSb, GaAs, Bi2Te3 and germanium." In: *Journal of Physics and Chemistry of Solids* 11.3-4 (1959), pp. 205–214.

[186] E. Clementi and D.-L. Raimondi. "Atomic screening constants from SCF functions." In: *The Journal of Chemical Physics* 38.11 (1963), pp. 2686–2689.

[187] J. Oliveira, C. Enderlein, M. Fontes, and E. Baggio-Saitovitch. "The pressure-dependence of the band gap of tellurium." In: *Journal of Physics: Conference Series*. Vol. 1609. 1. IOP Publishing. 2020, p. 012013.

[188] B. Yu, M. Zebarjadi, H. Wang, K. Lukas, H. Wang, D. Wang, C. Opeil, M. Dresselhaus, G. Chen, and Z. Ren. "Enhancement of thermoelectric properties by modulation-doping in silicon germanium alloy nanocomposites." In: *Nano letters* 12.4 (2012), pp. 2077–2082.

[189] D. Liu, X. Li, P. M. d. C. Borlido, S. Botti, R. Schmechel, and M. Rettenmayr. "Anisotropic layered Bi2Te3-In2Te3 composites: control of interface density for tuning of thermoelectric properties." In: *Scientific Reports* 7.1 (2017), p. 43611.